

Optimization Hyper-parameter Laws for Large Language Models

Xingyu Xie

XYXIE@NUS.EDU.SG

Department of Mathematics, National University of Singapore, Singapore.

Kuangyu Ding

KUANGYUD@U.NUS.EDU

Department of Mathematics, National University of Singapore, Singapore.

Shuicheng Yan

SHUICHENG.YAN@GMAIL.COM

School of Computing, National University of Singapore.

Kim-Chuan Toh

MATTOHKC@NUS.EDU.SG

Department of Mathematics and Institute of Operations Research and Analytics, National University of Singapore, Singapore.

Tianwen Wei

WEI.LILLE1@GMAIL.COM

Skywork AI, Beijing.

Abstract

Large Language Models have driven significant AI advancements, yet their training is resource-intensive and highly sensitive to hyper-parameter selection. While scaling laws provide valuable guidance on model size and data requirements, they fall short in choosing dynamic hyper-parameters, such as learning-rate (LR) schedules, that evolve during training. To bridge this gap, we present Optimization Hyper-parameter Laws (Opt-Laws), a framework that predicts final training loss as a function of LR schedule, model size, and data size. Grounded in SDE-based convergence and escape analyses, Opt-Laws yield interpretable convergence and escape features that predict final training loss across model scales, enabling schedule pre-selection from small-scale experiments. Empirically, Opt-Laws achieve a 94% Top-2 hit rate for identifying near-optimal schedule candidates on held-out configurations, correctly identify the best-performing schedule family in all five evaluated out-of-family settings, and detect training divergence with $F1 = 0.92$.

Keywords: LLM Efficient Training, Optimization Analysis, Scaling Laws, Convergence Guarantee, Escaping Probability.

1 Introduction

Large Language Models (LLMs) have emerged as a leading paradigm in artificial intelligence, yet their training processes impose significant demands on computational resources and energy (Achiam et al., 2023; Dubey et al., 2024; DeepSeek-AI et al., 2024; Xie et al., 2026). Given the immense scale and associated costs, training these models is typically a one-off endeavor, where crucial hyper-parameters, such as peak learning rate (LR), warmup steps, and LR schedules, must be predetermined and remain fixed throughout the training process. However, determining the optimal values for these hyper-parameters prior to experimentation is often challenging. Inadequate hyper-parameter selection can severely compromise the training process, potentially leading to failure and the consequent waste of computational resources and financial investment.

To address the complexities of hyper-parameter selection in large-scale models, researchers have increasingly relied on **Scaling Laws** (Kaplan et al., 2020; Hoffmann et al., 2022; Achiam et al., 2023). These scaling laws, derived from extensive empirical studies on small-scale models and datasets, provide a practical framework for predicting the relationships between certain hyper-parameters, such as model size and data volume, and training outcomes. By fitting these observed relationships to the power-law formula, scaling laws offer a heuristic approach for extrapolating the expected performance of large-scale models. This enables the selection of model size and data requirements prior to full-scale training, thereby reducing the likelihood of inefficient resource utilization.

While existing research on scaling laws focuses on the relationship between model scale, dataset size and model performance, few studies have explored the scaling law on training hyper-parameters, particularly time-dependent ones like the learning rate schedule. These hyper-parameters, including peak learning rate, are crucial for optimal model performance. Consequently, practitioners often rely on heuristic methods that frequently fall short in addressing the complex challenges of diverse training scenarios.

This challenge extends beyond pre-training. Fine-tuning or continual training of advanced foundation models, such as LLaMA3 (Dubey et al., 2024) or DeepSeek-V2 (DeepSeek-AI et al., 2024), encounters similar difficulties. Although fine-tuning is less computationally expensive than pre-training, the distribution shift between the fine-tuning data and the original training data complicates the selection of optimal hyper-parameters. Furthermore, since the model size is fixed during fine-tuning, scaling laws are not easily applicable. Consequently, the identification of optimal training hyper-parameters, particularly peak LR and warmup steps, typically requires iterative cycles of fine-tuning and evaluation. These hyper-parameters play a crucial role in balancing the retention of the foundation model’s inherent capabilities with its adaptation to new data (Ibrahim et al., 2024).

To address the challenge of hyper-parameter selection in large-scale LLM training, we propose a novel approach termed Optimization Hyper-parameter Laws, **Opt-Laws**. Opt-Laws exploits data gathered from small-scale models and datasets to establish mathematical relationships between training hyper-parameters and final training loss. This enables the pre-selection of suitable hyper-parameter configurations, such as the LR schedule, warmup steps, and peak LR, before commencing large-scale model training or fine-tuning. We first apply stochastic differential equations (SDEs) to model the training dynamics of prevalent first-order optimization algorithms, such as SGD and Adam (Kingma and Ba, 2014), within a continuous-time framework, followed by a detailed analysis of convergence rates and the probability of escaping local minima. This analysis yields a statistical vector of 15 feature terms (plus one intercept) encapsulating key training hyper-parameters, which is subsequently used in a linear regression model to obtain Opt-Laws. Notably, to the best of our knowledge, this is among the first works to utilize SDEs in establishing convergence rates of gradient-based methods for general non-convex optimization and to apply time-inhomogeneous SDEs for evaluating escape probabilities in non-convex settings.

In addition to loss prediction, the law provides qualitative interpretations of observed training patterns, such as the diminishing effect of schedule choice at large data scales and the dependence of optimal peak LR on model size. We validate Opt-Laws on MoE models with up to 4 billion trainable parameters and over 450 billion training tokens, covering

pre-training, continual training, and fine-tuning. The key contributions are summarized as follows:

- We propose Opt-Laws, a framework fitted on small-scale experiments that predicts final training loss for large-scale LLM training across model sizes, data budgets, and LR schedules. This allows pre-selection of LR schedules for pre-training, continual training, and fine-tuning before committing to full-scale runs.
- We derive SDE-based convergence and escape bounds for both SGD and Adam under general time-varying learning rates in non-convex settings. Both optimizers yield similar functional forms, motivating a unified feature construction that decomposes the schedule’s effect into convergence speed and escape dynamics.
- We conduct extensive experiments on held-out prediction, divergence detection, out-of-family schedule generalization, and LR schedule ranking in continual training and fine-tuning. The generalized Opt-Laws selects a near-optimal schedule in 94% of held-out evaluations, detects divergence with F1=0.92, and correctly identifies the best schedule family in all five out-of-family groups.

Roadmap. Sec. 2 reviews related work. Sec. 3 introduces the simplified Opt-Laws at a fixed model size. Sec. 4 extends it to the generalized Opt-Laws across model scales and reports the primary held-out benchmark. Sec. 5 evaluates cross-scale extrapolation, out-of-family schedule generalization, and ranking in continual training and fine-tuning. Sec. 6 provides the SDE-based theoretical justification for the feature construction.

2 Related Work

2.1 Scaling Laws

The study of scaling laws in LLMs has been essential for understanding how model performance scales with increases in model size, data volume, and computational resources. While early research attempted to model multilayer neural network performance using power laws (Rosenfeld et al., 2020), Kaplan et al. (2020) were the first to apply this approach systematically to LLM training. This foundational work had led to several variations, including the Chinchilla law (Hoffmann et al., 2022; Besiroglu et al., 2024), Mosaic law (Sardana et al., 2024), and models from DeepSeek (Bi et al., 2024) and MiniCPM (Hu et al., 2024), all of which primarily utilize an empirical power law that defines the relationship between training loss, model size N , and data size D in LLMs:

$$\text{Loss} = \underbrace{\frac{A_1}{N^{\kappa_1}}}_{\text{Model-size dependent}} + \underbrace{\frac{A_2}{D^{\kappa_2}}}_{\text{Data-size dependent}} + \underbrace{A_3}_{\text{Irreducible}},$$

where $\kappa_1, \kappa_2 > 0$ represent the scaling exponents, $A_1, A_2 > 0$ are coefficients, and $A_3 \in \mathbb{R}$ denotes the irreducible loss component. Recent studies (Muennighoff et al., 2024; Goyal et al., 2024) have highlighted the impact of data repetition and quality on scaling behavior, suggesting the need for more frequent updates to existing scaling laws. Some researchers have also questioned the sufficiency of power law models, advocating for more complex

parameterizations to better capture the relationship between model size and data volume (Hernandez et al., 2021; Caballero et al., 2023). Other studies have extended power laws to model the relationship between training loss and individual hyper-parameters, such as batch size (DeepSeek-AI et al., 2024). Additionally, scaling laws have been applied in downstream task losses (Dubey et al., 2024) or later stages of model alignment, such as fine-tuning (Isik et al., 2024) and RLHF (Gao et al., 2023). Recent works have begun incorporating LR schedules into scaling-law-style predictors. Tissue et al. (2025) combine cumulative learning-rate and annealing-area features with a model-size interaction to predict per-step loss, while Luo et al. (2025) develop a multi-power-law approach for the same task. Opt-Laws differs in both construction and scope: the feature family is derived from SDE-based convergence and escape analyses rather than empirical curve fitting, the prediction target is the final training loss across model scales rather than the per-step loss curve, and the framework extends to continual training and fine-tuning through history-aware modifications.

2.2 Convergence Analysis via Dynamical Systems

Dynamical systems are powerful tools in the convergence analysis of optimization algorithms. Over the past decade, numerous studies such as Su et al. (2014); May (2017); Attouch et al. (2018); Muehlebach and Jordan (2019); Attouch et al. (2024) have utilized ordinary differential equations (ODEs) to analyze algorithmic convergence properties, particularly employing high-order (with order ≥ 2) ODEs to intuitively interpret the mystery behind momentum acceleration, such as Polyak’s heavy ball method (Polyak, 1987) and Nesterov’s acceleration (Nesterov, 1983) in smooth convex optimization problems. In the realm of non-smooth non-convex optimization, differential inclusions, which are more general than ODEs, have recently been applied to establish the convergence of subgradient methods (Duchi and Ruan, 2018; Davis et al., 2020; Xiao et al., 2024; Ding and Toh, 2024). In addition to ODE-based methods, recent studies (Gess and Kassing, 2023; Maulen-Soto et al., 2022, 2024) have started using SDEs to derive convergence rates for stochastic gradient methods in convex optimization problems or non-convex optimization problem under Polyak-Łojasiewicz (PL) condition. However, to the best of our knowledge, no SDE-based approach has been established for determining convergence rates in the general non-convex settings. *To the best of our knowledge, our work is among the first to apply SDEs in establishing convergence rates for general non-convex problems, with our derived bounds applicable to any general learning rate policy, without relying on specific patterns such as constant, sublinearly decaying, or linearly decaying learning rates.* On the optimization side, Li et al. (2021a) and Wang et al. (2021) are relevant to our schedule-dependent convergence discussion, while Bergsma et al. (2025) is particularly relevant to our discussion of schedules that decay to zero and to the limitations of schedules with non-zero final learning rates.

2.3 Escaping analysis via SDEs

A closely related research area involves analyzing SGD’s escape dynamics using SDEs (Nguyen et al., 2019; Xie et al., 2020; Mori et al., 2022; Ibayashi and Imaizumi, 2023; Battash et al., 2024). These work focus on estimating the exit time, which measures how quickly an SGD sequence can move from a sharp local minimum to a flatter region, potentially improving

generalization performance (Keskar et al., 2016; Foret et al., 2020). The classic Eyring-Kramers law (Kramers, 1940; Berglund, 2013), based on large deviation theory, is typically used for such exit time estimations. However, this approach is not directly applicable in our case due to the time-inhomogeneity of the SDEs, which arises from the time-dependent learning rate schedule. To address this challenge, we employ a Gaussian approximation to make the escape analysis more tractable under mild conditions.

3 Optimization Hyper-parameter Laws

This section introduces the simplified Opt-Laws at a fixed model size, capturing the relationship between LR schedule and final training loss without cross-scale variation. The generalized multi-scale extension and held-out evaluation are presented in Sec. 4.

3.1 Opt-Laws with Fixed Model Size

We propose the Opt-Laws in Eqn. (1) to predict the training loss for LLMs. Because the training epoch for both pre-training and continual training is typically set to one, the training loss closely approximates the validation loss. In this section, we fix the model size and consider the LR schedule $\eta(t) \geq 0$ for all $t \in [0, S]$, where η_{\max} denotes the peak LR, and S represents the total training steps (proportional to data size D such that $D = S \times \text{Batch size} \times \text{Token length}$). The function $\eta(t)$ is defined as $\eta(\Delta_t k) = \eta_k$, where η_k is the LR used at the k -th training step, and Δ_t is a sufficiently small time step. This mapping effectively links each step-index to its corresponding LR.

For simplicity, we set the initial and final values of η_t to zero, i.e., $\eta(0) = \eta(S) = 0$, though these values can be adjusted based on practical requirements. Under these conditions, the training loss and training hyper-parameters adhere closely to the following relationship:

$$\log(\text{Loss}) = \underbrace{c_1 \left(\int_0^a \eta(s) ds \right)^{-\alpha_1} + c_2 \left(\int_a^S \eta(s) ds \right)^{-\alpha_2}}_{\text{convergence speed}} + \underbrace{\frac{c_3}{S} + b}_{\text{bias}} + \underbrace{c_4 \left(\int_0^a (\eta'(s))^2 ds \right)^{\alpha_3} + c_5 \left(\int_a^S (\eta'(s))^2 ds \right)^{\alpha_4}}_{\text{ease of escaping local region}} \quad (1)$$

where a denotes the warm-up duration (denoted by a_1 in the later generalized multi-phase notation), $\eta'(s)$ is the time derivative of $\eta(s)$, the constants $c_1, c_2, c_3, c_4, c_5, \alpha_1, \alpha_2, \alpha_3, \alpha_4 > 0$, and $b \in \mathbb{R}$ are all dependents on the model and training data. Analogous to scaling laws, Opt-Laws is first parameterized by fitting its constants and power terms on a small-scale model with a similar network architecture and a small subset of the dataset. The parameterized Opt-Laws can then be applied to choosing hyper-parameters in large-scale training. The details on the parameters fitting are clarified in Secs. 3.2 and 4.3.

The first component in Eqn. (1) addresses the convergence speed, elucidating the impact of the LR schedule $\eta(t)$ on optimization convergence. Given the same computational budget, training dynamics with faster convergence tend to achieve lower training loss, thereby enhancing overall efficiency. Notably, the loss is inversely proportional to $\int_a^S \eta_t$, suggesting that, within certain bounds, a higher peak LR can be beneficial (Xie et al., 2024b). However,

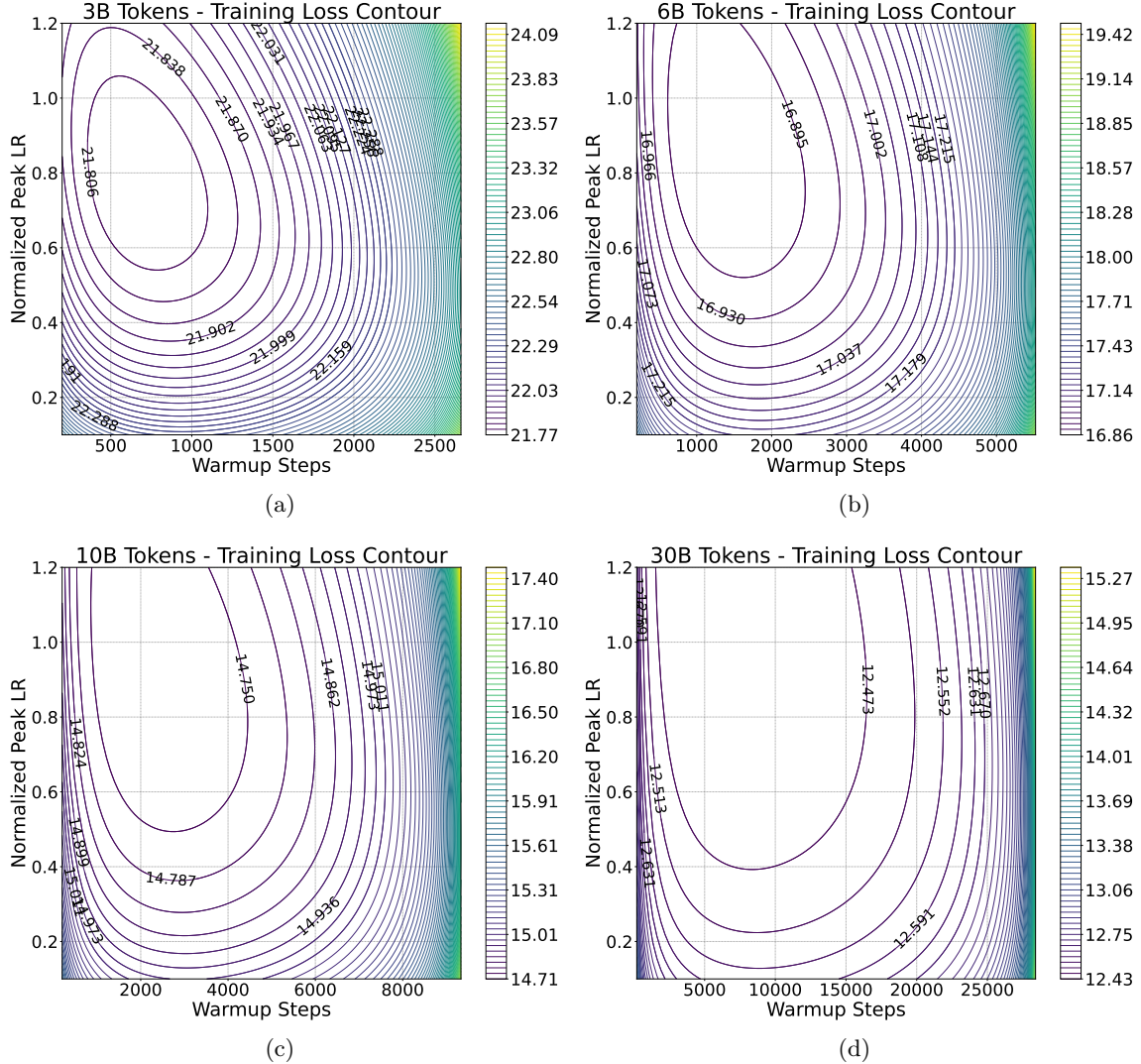


Figure 1: Opt-Laws-predicted perplexity contours as a function of warmup steps and normalized peak LR for the $8 \times 0.1\text{B}$ MoE model at four token budgets (3B, 6B, 10B, 30B). Darker regions indicate lower predicted loss. As the token budget grows, the low-loss region expands and becomes less sensitive to warmup configuration.

an excessively high peak LR can also increase the integral $\int_a^S \eta_t'^2$, indicating the need to carefully balance the benefits of a high peak LR against the potential drawbacks. Note that for convenience, we use notation such as $\int_a^S \eta_t'^2$ to denote $\int_a^S (\eta'(t))^2 dt$ in the previous sentence and other parts of this paper.

The escape terms in Eqn. (1) reflect the schedule’s influence on basin selection. A larger $\int (\eta_t')^2$ increases the trapping probability near the current basin, so overly rapid warmup or cooldown can lock the optimizer into a suboptimal region. This is consistent with LLM training practice, where excessively aggressive schedule transitions degrade performance (Hu et al., 2024).

3.2 Illustrative Fixed-Model Fit

This subsection provides a qualitative fixed-model illustration of the simplified Opt-Laws. The main predictive evaluation of the paper is deferred to the held-out and extrapolation benchmarks in Secs. 4 and 5.

We apply Opt-Laws in Eqn. (1) to fit the training loss of an $8 \times 0.1\text{B}$ MoE model (Zhao et al., 2024; Wei et al., 2024). The decision to use an MoE model over a dense model is based on two key factors: (1) many state-of-the-art LLMs (Achiam et al., 2023; DeepSeek-AI et al., 2024; Reid et al., 2024; Yang et al., 2024; Bai et al., 2023) employ MoE architectures, reflecting current trends, and (2) MoE models are computationally more efficient, allowing faster experimentation within our computational constraints. In this experiment, we fix the model and batch sizes (both with a token length and batch size of 1024) while varying the token quantities from the RedPajama-v2 dataset (Computer, 2023): 3B, 6B, 10B, and 30B tokens. We adjust the warmup steps and peak LRs to analyze their impact on final loss. The LR schedule $\eta(t)$ linearly increases to a peak LR η_{\max} during warmup, followed by a linear decay to zero in the cooldown phase. The warmup steps are denoted by a . Here and below, the normalized peak LR means the peak LR divided by the reference scale used in our fitting procedure (see Appendix A.3.1).

We use the fitted Opt-Laws to predict final training loss across the warmup-step and peak-LR grid for each token budget. The predicted perplexity contours are shown in Fig. 1, with a regression error on convergent runs below 0.5%. Several patterns are visible: as training data increases, the strong-performance region expands, indicating greater robustness to hyper-parameter variation. The influence of warmup steps weakens at larger token budgets, consistent with prior observations (Gupta et al., 2023; Ibrahim et al., 2024), though excessively short warmup remains harmful (left side of Fig. 1). These patterns are interpreted through the Opt-Laws formulation in the next subsection. Divergent runs are excluded from the regression error and analyzed in Sec. 4.1.

3.3 Qualitative Predictions of the Simplified Opt-Laws

This subsection interprets several observed LLM training phenomena through the simplified Opt-Laws. By analyzing the convergence and escape terms in Eqn. (1), we derive qualitative predictions about how warmup duration and LR schedule choice affect final loss.

3.3.1 INFLUENCE OF WARMUP STEPS ON TRAINING LOSS

Recent research has demonstrated that the number of warmup steps has little effect on the final loss during continual training. For instance, Ibrahim et al. (2024); Gupta et al. (2023) report negligible loss variation across warmup configurations for 0.5B-parameter dense models trained on 100B+ tokens. This finding is consistent with our results in Fig. 1 (d). When the token count is sufficiently large and surpasses the Chinchilla Scaling Law (25.6 tokens per parameter) (Hoffmann et al., 2022; Besiroglu et al., 2024), the range of effective warmup steps broadens significantly, making the final loss insensitive to changes in warmup duration.

This observation does not contradict other studies (Lv et al., 2023; Jin et al., 2023) that emphasize the need for careful tuning of warmup steps. Such sensitivity is primarily seen during fine-tuning, where the token-to-parameter ratio is much lower than the value suggested

by the Chinchilla Scaling Law. This aligns with our findings in Fig. 1 (a) and Fig. 1 (b), which show a narrower optimal range for warmup steps. Consequently, fluctuations in loss due to variations in the warmup steps are more likely to occur during fine-tuning.

3.3.2 INSIGHTS INTO LR SCHEDULE EFFECTS THROUGH OPT-LAWS

OpenAI researchers previously observed that the LR schedule $\eta(t)$ has a negligible impact on the final training loss (Kaplan et al., 2020). However, recent studies on pre-training and continual training of LLMs have discovered new LR schedules that achieve lower training losses compared to the widely-used cosine decay schedule (Ibrahim et al., 2024; Hägele et al., 2024). Opt-Laws offers a unified interpretation of these seemingly contradictory observations.

Opt-Laws reveal that the model loss has an asymptotic lower bound related to the model capability. When the dataset is sufficiently large, the training loss approaches this asymptotic bound, rendering it independent of the LR schedule. However, the rate at which the loss approaches this bound is influenced by the LR schedule $\eta(t)$. This explains why, during fine-tuning or continual training, it is possible to find some LR schedules that outperform cosine decay: these newly discovered schedules enable the model to reach its performance limits more rapidly. Yet, as the dataset size increases, the differences introduced by varying LR schedules diminish.

To further elucidate this asymptotic behavior, we will now consider two specific scenarios to derive the precise expressions of the Opt-Laws. The first is the classical linear warmup followed by cosine decay. In this schedule, the LR is linearly increased to η_{\max} over a steps, and then decays to zero in a cosine fashion.

$$\eta_{\cos}(t) = \begin{cases} \eta_{\max} \cdot \frac{t}{a} & t \in [0, a] & \text{(warmup)}, \\ \frac{\eta_{\max}}{2} \cdot \left(\cos\left(\pi \cdot \frac{t-a}{S-a}\right) + 1 \right) & t \in [a, S] & \text{(cooldown)}, \end{cases} \quad (2)$$

where a is the linear warmup steps, and S represents the total training steps. The second schedule has gained popularity in the recent continual training of LLMs, as evidenced in the work (Hu et al., 2024; Hägele et al., 2024). In this strategy, the LR is linearly increased to η_{\max} , held constant for a period, and then rapidly decayed to the minimum value. For simplicity, we model the decay as a linear decrease to zero.

$$\eta_{\text{const}}(t) = \begin{cases} \eta_{\max} \cdot \frac{t}{a} & t \in [0, a] & \text{(warmup)}, \\ \eta_{\max} & t \in [a, a_c] & \text{(constant)}, \\ \eta_{\max} \cdot \left(1 - \frac{t-a_c}{S-a_c} \right) & t \in [a_c, S] & \text{(cooldown)} \end{cases} . \quad (3)$$

Here, $a_c - a$ represents the duration of the constant LR phase, and $S - a_c$ is the period over which the LR linearly decays to zero. In Opt-Laws Eqn. (1), we incorporate the constant LR phase into the cooldown phase for simplification. For more complex LR schedules, the distinction between the warmup phase and other phases is elaborated in Sec. 4.3. We can derive the following proposition, which demonstrates that as the data size increases, the difference between η_{\cos} and η_{const} diminishes under Opt-Laws($\eta(\cdot)$), which we define as $\log(\text{Loss})$ in Eqn. (1).

Proposition 1 *Let $a = r_a S$ and $a_c = r_{a_c} S$. For any $r_a > 0$ and $r_{a_c} > 0$ such that $0 < r_a \leq r_{a_c} < 1$, it holds that*

$$\lim_{S \rightarrow \infty} |\text{Opt-Laws}(\eta_{\cos}(\cdot)) - \text{Opt-Laws}(\eta_{\text{const}}(\cdot))| = 0.$$

If we set $a = 0.01S$ and $a_c = 0.85S$ (as recommended by [Hu et al. \(2024\)](#)), when S is relatively small, η_{const} yields a lower predicted loss because $\int_a^S \eta_{\text{const}}(s)ds$ is larger, consistent with [Hu et al. \(2024\)](#); [Hägele et al. \(2024\)](#). However, when $a = a_c$ (no constant phase), the ordering reverses, matching our experimental results in [Sec. 5](#).

As S becomes sufficiently large, the Opt-Laws for both LR schedules asymptotically converge to a fixed value. This value depends solely on the model capacity and data property, and is independent of the specific LR schedule. This explains the finding of [Kaplan et al. \(2020\)](#), where small models (3M parameters) trained on large datasets showed negligible schedule sensitivity, as the loss was already near its asymptotic limit.

These observations motivate the generalized construction in [Sec. 4](#), which introduces cross-scale variation, divergence modeling, and interaction terms, with empirical evaluation in [Sec. 5](#).

4 Generalized Opt-Law across Scales

This section extends the simplified Opt-Laws to the multi-scale setting by incorporating model size, divergence boundaries, and interaction terms. We standardize the optimizer and LR schedule (linear warmup followed by linear cooldown) and perform grid experiments across a range of model sizes, LR, warmup steps, and data sizes. Specific details on the MoE configurations are provided in [Sec. A](#). The results are summarized in [Fig. 2](#), where each grid point represents the smoothed final training loss; divergent runs are assigned a loss of 7. As [Fig. 2](#) shows, incorporating model size reveals non-monotonic local structure and divergence boundaries that the simplified unimodal form in [Sec. 3](#) cannot capture. To address these challenges, we first define a divergence prediction criterion ([Sec. 4.1](#)), then construct the generalized feature family ([Sec. 4.2](#)), and evaluate the resulting law via a held-out benchmark on the training grid ([Sec. 4.3](#)).

4.1 Predicting Training Divergence

We first discuss the selection of hyper-parameters to prevent training divergence. [Fig. 2](#) provides two key insights: (1) Excessively high peak LR can cause divergence, but increasing the warmup duration can prevent this, to make training stable. (2) The hyper-parameter combinations that lead to divergence vary, depending on the model and data size.

For general non-convex optimization problems $\min_{\mathbf{x}} f(\mathbf{x})$, optimization theory typically dictates that the peak LR η_{max} should not exceed $2/L$, where L is the Lipschitz constant of the function gradient $\nabla f(\cdot)$, regardless of the LR schedule ([Arjevani et al., 2022](#); [Xie et al., 2024b](#); [Rotaru et al., 2024](#)). However, estimating the Lipschitz constant for neural networks remains an open challenge ([Kim et al., 2021](#); [Khromov and Singh, 2024](#)). Moreover, recent studies indicate that surpassing certain theoretical thresholds for peak LR does not necessarily lead to divergence; rather, when appropriately managed, peak LR above $2/L$ can even enhance convergence ([Grimmer et al., 2024](#)).

From these observations, we hypothesize that training divergence is not merely a consequence of an excessively large η_{max} . Instead, it is influenced by the duration that the LR remains above a critical threshold η_L and the length of the warmup phase. Ideally, η_L would correspond to $2/L$, where L is the Lipschitz constant of the function gradient. For neural

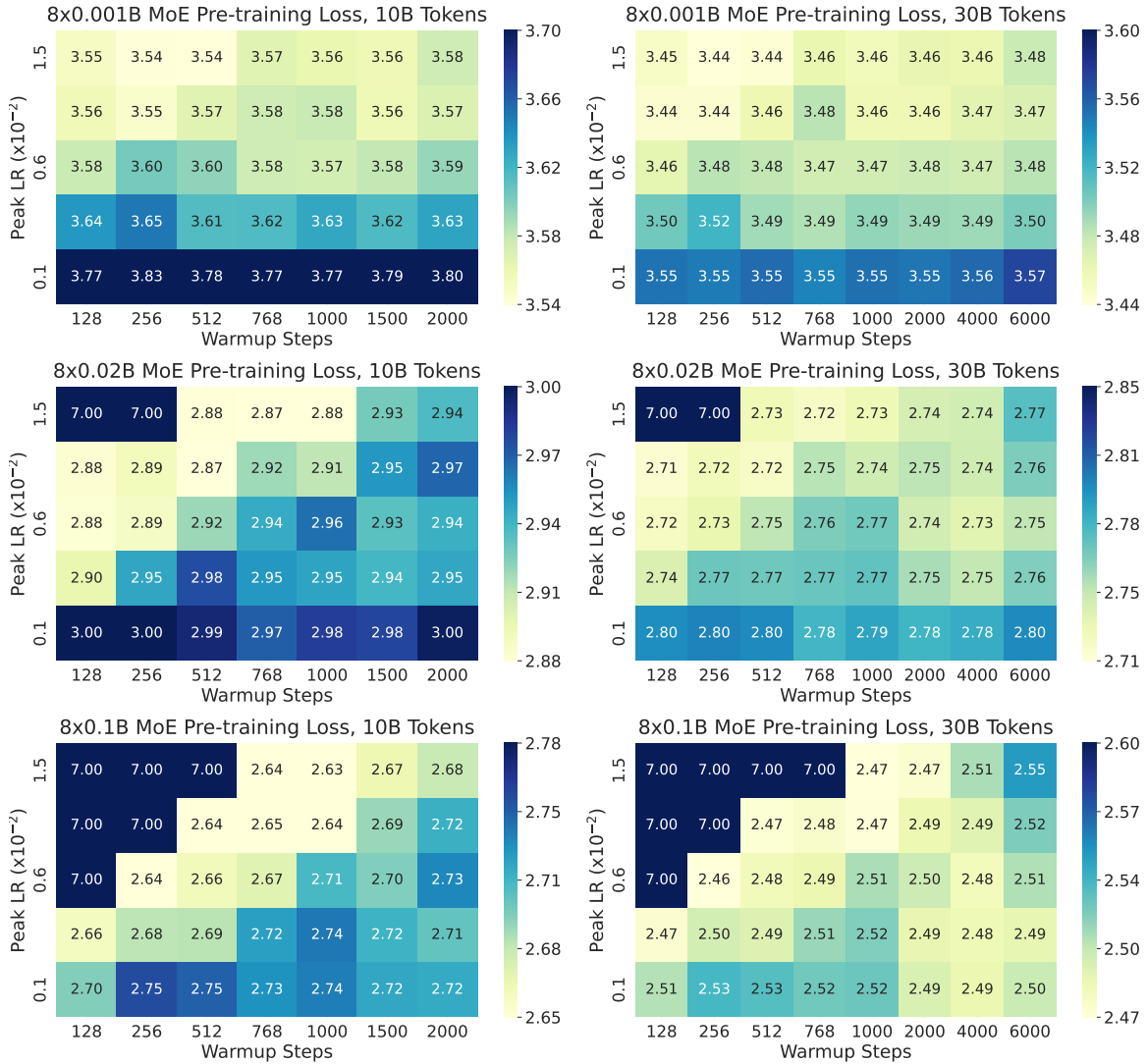


Figure 2: Smoothed final training loss across various combinations of training parameters, including model sizes from $8 \times 0.001\text{B}$ to $8 \times 0.3\text{B}$ MoEs, peak LRs from $1\text{e-}3$ to $1.5\text{e-}2$, warmup steps from 128 to 6000, and data sizes of 10B and 30B tokens. Each grid point represents the loss for a specific parameter set. Divergent training runs were assigned a loss of 7, reflecting the typical plateau observed in practice.

networks, L tends to increase with model size (Khromov and Singh, 2024), suggesting that η_L should decrease as the model size grows. However, with larger datasets η_L can increase. A larger data volume gives the training dynamics more iterations to recover from an excessively high peak LR, as illustrated in Fig. 2. Based on this intuition, we let $\eta_L = \mathcal{O}(S^{\hat{\alpha}_1}/N^{\hat{\alpha}_2})$, where $\hat{\alpha}_1, \hat{\alpha}_2 > 0$ are data-driven constants, S is the number of iterations (proportional to data size), and N is the model size (i.e., the number of learnable parameters). Building on these insights, we define a divergence criterion by comparing the below-threshold warmup area against the above-threshold area in the LR schedule (Fig. 3). When above-threshold

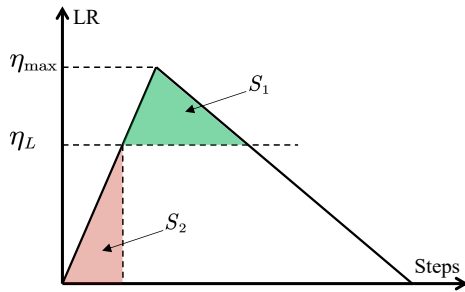


Figure 3: Divergence prediction criterion. The shaded regions denote the below-threshold warmup area ($\text{LR} < \eta_L$) and the above-threshold area ($\text{LR} \geq \eta_L$). The ratio of these two areas motivates the divergence discriminant R in Eqn. (4).

exposure dominates, training is expected to diverge. We parameterize this comparison as:

$$R(\eta_{\max}, a_1, N, S) := \frac{S(\eta_{\max} - \eta_L)^2}{\hat{c}_3 a_1 \eta_L^2}, \quad \eta_L := \min\left(\eta_{\max}, \frac{\hat{c}_1 S^{\hat{\alpha}_1}}{\hat{c}_2 N^{\hat{\alpha}_2}}\right), \quad (4)$$

where S is the iteration number, N is the model size, a_1 is the number of warmup steps (corresponding to the warm-up duration a in the simplified Opt-Laws above), and $\hat{c}_1 > 0$, $\hat{c}_2 > 0$, $\hat{c}_3 > 0$, $\hat{\alpha}_1 > 0$, and $\hat{\alpha}_2 > 0$ are data-driven parameters. Similar to the Opt-Laws approach, these parameters are estimated by fitting the real data presented in Fig. 2, with the fitted values provided in Appendix Sec. A. The area comparison motivates the functional form of R , while the coefficient \hat{c}_3 calibrates the decision boundary to $R = 1$. Empirically, warmup stabilizes training more effectively than above-threshold exposure destabilizes it, so the fitted boundary lies far from the equal-area point. We find that if $R(\eta_{\max}, a_1, N, S) > 1$, indicating that the time spent above η_L is too long relative to the effective warmup duration, training is likely to fail. Conversely, if $R(\eta_{\max}, a_1, N, S) < 1$, the chosen hyper-parameters are unlikely to cause divergence. In Eqn. (4), η_L is inversely related to model size and directly proportional to data size, implying that larger models require lower peak LR, while larger datasets may permit a higher peak LR. This is consistent with established practices in training modern LLMs, such as LLaMAs (Dubey et al., 2024).

As shown in Fig. 5, the $R(\eta_{\max}, a_1, N, S)$ metric effectively predicts training outcomes across various data sizes, model sizes, and hyper-parameter combinations. In the figure, for scenarios where $R > 1$, we assign a fixed sentinel value of 7 to mark expected divergence.

4.2 Generalized Opt-Laws

Building on the patterns in Fig. 2, we construct the feature family in three stages. First, we define schedule-dependent basis terms motivated by the convergence and escape analyses, which summarize how the schedule affects optimization progress and schedule-induced exploration. Second, we introduce scale-dependent terms for model size and training horizon, in order to capture cross-scale variation that is absent from the simplified law. Third, we include a restricted set of interaction terms between these components, so that the effect of a schedule can vary with model and data scale.

The goal of this construction is not to enumerate all possible monomials, but to retain a compact and interpretable theory-motivated basis that is expressive enough for the observed loss grids while avoiding unnecessary over-parameterization. Specifically, given a LR schedule

$\eta(t)$, SDE-based convergence analysis (Sec. 6, Theorems 1 and 2) shows that the averaged squared gradient norm for both SGD and Adam is bounded in terms of the integrated learning rate $\int_0^t \eta(s) ds$. This integral therefore serves as a natural surrogate for optimization progress. The resulting convergence-related basis terms take the form

$$\text{Convergence Bound} \propto \left[\frac{N}{\int_0^{a_{c_1}} \eta(t) dt}, \frac{N}{\int_{a_{c_2}}^S \eta(t) dt} \right], \quad (5)$$

where the convergence bound represents the average gradient norm, usually serving as an indicator of how near the current loss is to a local minimum in continuous optimization, S represents the number of iterations, N is the model size, and $a_{c_1} \leq a_{c_2}$ are specific points within the interval $[0, S]$ that define the divisions in the LR schedule. The ‘‘proportional to’’ \propto indicates that the convergence bound is influenced by these basis functions in Eqn. (5). Specifically, when the values of these functions are smaller for a given $\eta(t)$, the optimization algorithm tends to converge more quickly to a stationary point.

Typically, a_{c_1} marks the end of the warmup phase, and a_{c_2} indicates the start of the cooldown phase. Ibrahim et al. (2024) observed that LR variations during intermediate phases have limited effect on the final loss when warmup and cooldown are properly configured. We therefore retain only the warmup and cooldown segments in the convergence features. The specific instantiation and a supporting ablation are given in Sec. 4.3 and Appendix Sec. A.4.

Complementarily, SDE-based escape analysis (Sec. 6, Theorems 3 and 4) shows that the probability of remaining trapped near a local minimum grows with the integrated squared learning-rate derivative, motivating the following escape-related basis terms:

$$\text{Trapping Probability} \propto \left[\frac{1}{SN}, \int_0^{a_{e_1}} \eta'(t)^2 dt, \int_{a_{e_2}}^S \eta'(t)^2 dt \right], \quad (6)$$

where N is the model size, and $a_{e_1} \leq a_{e_2}$ are values between 0 and S . Similar to the previous Eqn. (5), smaller values of these basis functions in Eqn. (6) indicate a higher probability of escaping a local region under the chosen $\eta(t)$.

To extend the Opt-Laws, we consider pairwise combinations of the basis functions from Eqn. (5) and Eqn. (6). We introduce three sets of terms: the convergence term $C(\eta_t, \mathbf{a}_c, S, N, \boldsymbol{\alpha})$:

$$C(\eta_t, \mathbf{a}_c, S, N, \boldsymbol{\alpha}) := \left[\frac{1}{\int_0^{a_{c_1}} \eta_t}, \frac{1}{\int_{a_{c_2}}^S \eta_t}, \left(\frac{N}{\int_{a_{c_2}}^S \eta_t} \right)^{\alpha_1}, \left(\frac{1}{\int_0^{a_{c_1}} \eta_t \int_{a_{c_2}}^S \eta_t} \right)^{\alpha_2} \right],$$

where $\boldsymbol{\alpha}$ is a predefined vector representing the powers of certain basis functions; the escaping local region term $E(\eta_t, a_e, S, N, \boldsymbol{\alpha})$:

$$E(\eta_t, a_e, S, N, \boldsymbol{\alpha}) := \left[\int_{a_{e_2}}^S \eta_t'^2, \left(\int_0^{a_{e_1}} \eta_t'^2 \right)^{\alpha_3}, \left(\int_{a_{e_2}}^S \eta_t'^2 \right)^{\alpha_4}, \left(\frac{1}{SN} \right)^{\alpha_5} \right],$$

And the mixed term $M(\eta_t, \mathbf{a}_c, \mathbf{a}_e, S, N, \boldsymbol{\alpha})$:

$$M(\eta_t, \mathbf{a}_c, \mathbf{a}_e, S, N, \boldsymbol{\alpha}) := \left[\left(\frac{\int_{a_{e_2}}^S \eta_t'^2}{\int_0^{a_{c_1}} \eta_t} \right)^{\alpha_6}, \left(\frac{\int_{a_{e_2}}^S \eta_t'^2}{\int_{a_{c_2}}^S \eta_t} \right)^{\alpha_7}, \left(\frac{N \int_{a_{e_2}}^S \eta_t'^2}{\int_0^{a_{c_1}} \eta_t} \right)^{\alpha_8}, \left(\frac{N \int_{a_{e_2}}^S \eta_t'^2}{\int_{a_{c_2}}^S \eta_t} \right)^{\alpha_9} \right].$$

We then combine these terms to define the optimization-feature vector for Opt-Laws:

$$F(\eta_t, \mathbf{a}_c, \mathbf{a}_e, S, N, \boldsymbol{\alpha}) := [C(\eta_t), E(\eta_t), M(\eta_t), N^{-\alpha_{10}}, S^{-\alpha_{11}}, \eta_{\max}^{\alpha_{12}}, 1], \quad (7)$$

where, for the sake of notation, we omit certain arguments of $C(\cdot)$, $E(\cdot)$, and $M(\cdot)$. For readability, the main text groups the terms into convergence, escape, mixed, and scale components; the corresponding fitted coefficients and closed-form expressions for two representative schedule families are given in Appendix Table 8.

Discussion The terms in $F(\cdot)$ are derived from the SDE convergence bound $O(N/\int \eta)$ (Theorems 1-2) and the escape bound involving $\int \eta_t'^2$ and $1/SN$ (Theorems 3-4). Splitting the schedule into warmup and cooldown segments yields the per-segment convergence terms $1/\int \eta_w$ and $1/\int \eta_c$, and the model-size-scaled term $(N/\int \eta_c)^\alpha$ that retains N from the bound. The warmup-cooldown product $(1/(\int \eta_w \cdot \int \eta_c))^\alpha$ captures their joint contribution. The escape block follows the same splitting logic. The mixed terms multiply the convergence basis $1/\int \eta$ with the escape basis $\int \eta_t'^2$, producing $\int \eta_t'^2/\int \eta$ and $N \cdot \int \eta_t'^2/\int \eta$ with warmup and cooldown variants. Combinations not present in the bounds (e.g., $\int \eta \times S$) are not included. This yields 15 terms plus one intercept.

The three terms $(1/\int \eta_w, 1/\int \eta_c, \int \eta_t'^2)$ preserve the closed-form expressions from the SDE analysis and carry no fitted exponent. Scale terms carry fitted exponents following standard power-law parameterization. Interaction terms require fitted exponents because the convergence and escape bounds are derived independently and do not predict their coupling. The escape exponents α_3, α_4 are fitted rather than fixed at the theoretical value, as the underlying bounds rely on approximations that may not fully capture real training dynamics.

The feature construction reveals a natural convergence-escape trade-off. The convergence terms $C(\cdot)$ suggest that maintaining a higher LR allows for a larger $\int \eta_t$, which accelerates the convergence. However, an excessively high LR can lead to increased $(\eta_t')^2$ during warmup and cooldown, causing the escape terms $E(\cdot)$ to rise and potentially trapping the model in poor local minima. Unlike in Sec. 3.1, where model size was not factored in, introducing model size reveals a trade-off: larger models slow convergence (as $N/\int \eta_t$ increases) but reduce the escape terms (as $1/SN$ decreases), highlighting the need for balance. Additionally, the mixed terms provide insights into the interaction between model size and peak LR. For example, the term $N \int (\eta_t')^2/\int \eta_t$ indicates that when data size increases modestly while model size N grows significantly, reducing the peak LR becomes necessary to keep this term small. This aligns with empirical observations that the optimal peak LR tends to decrease as model size increases (Dubey et al., 2024).

The feature vector $F(\cdot)$ is designed to capture the dominant factors relating training hyper-parameters to final loss, enabling us to derive generalized Opt-Laws through linear regression.

$$\log(\text{Loss}) = \mathbf{c}^\top F(\eta_t, \mathbf{a}_c, \mathbf{a}_e, S, N, \boldsymbol{\alpha}), \quad (\text{Opt-Laws})$$

where $(\eta_t, \mathbf{a}_c, \mathbf{a}_e, S, N)$ is the combination of training parameters, $\boldsymbol{\alpha}$ represents the powers of the basis functions, and \mathbf{c} is the solution to the following linear regression problem:

$$\mathbf{c} = \underset{\mathbf{c}}{\operatorname{argmin}} \left\{ \sum_i \left(\mathbf{c}^\top F(\eta_t^i, \mathbf{a}_c^i, \mathbf{a}_e^i, S^i, N^i, \boldsymbol{\alpha}) - \log(\text{Loss}_i) \right)^2 \right\}, \quad (8)$$

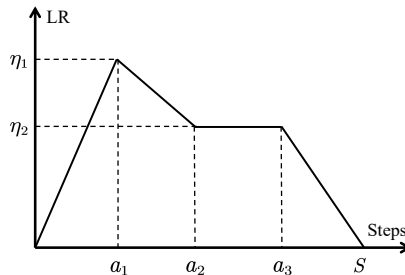


Figure 4: A four-phase LR schedule template illustrating the selection of \mathbf{a}_c and \mathbf{a}_e in **Opt-Laws**.

where $(\eta_t^i, \mathbf{a}_c^i, \mathbf{a}_e^i, S^i, N^i)$ represents the different hyper-parameter combinations shown in Fig. 2, and Loss_i denotes the final training loss associated with each combination (excluding divergent losses during regression). We adopt a staged procedure: the exponent vector α is selected from a discrete candidate set using only the training data, and the linear coefficients \mathbf{c} are then fitted on the training split. The held-out set is reserved for final evaluation only (details in Appendix Sec. A.3). The proposed **Opt-Laws** can, under certain conditions, recover classical scaling laws. For instance, when the LR schedule is fixed and model size N is the only variable, normalizing N to a range much smaller than 1 allows **Opt-Laws** to approximate the broken neural scaling laws (BNSL) (Caballero et al., 2023). Specifically, BNSL is expressed as $\log(\text{Loss}) = \bar{b} + \sum_i \bar{c}_i \log(1 + N^{\bar{\alpha}_i}) \approx \bar{b} + \sum_i \bar{c}_i N^{\bar{\alpha}_i}$, where $\bar{\alpha}_i$ and \bar{b} are data-driven parameters and the approximation represents **Opt-Laws**. BNSL has been shown to outperform the classical Kaplan scaling laws across both upstream and downstream tasks. Furthermore, by applying a logarithmic transformation to N during normalization and selecting $\alpha_1 = \alpha_8 = \alpha_9 = \alpha_{10} = 1$, **Opt-Laws** can closely approximate the classical Kaplan and Chinchilla scaling laws (Kaplan et al., 2020; Hoffmann et al., 2022).

4.3 Evaluation on the Training Grid

This subsection evaluates the generalized **Opt-Laws** on the training grid via held-out benchmarking. Fig. 4 depicts the piecewise-linear schedule template used throughout, parameterized by transition points a_1, a_2, a_3 . Standard families arise as special cases: linear warmup plus linear cooldown ($a_1 = a_2 = a_3$), constant-rate-plus-cooldown (Hägele et al., 2024) ($a_1 = a_2 < a_3$), and multi-phase polygon schedules (Ibrahim et al., 2024) ($a_1 < a_2 < a_3$).

To evaluate **Opt-Laws** on this template, we map the abstract partition points \mathbf{a}_c and \mathbf{a}_e to the transition points a_1, a_2, a_3 that define the phase boundaries of the schedule. For the convergence terms, we set $a_{c_1} = a_1$ and $a_{c_2} = a_2$. If a constant phase precedes the cooldown at the same LR, it is included in $\int_{a_{c_2}}^S \eta dt$, as it involves no LR change and shares the same LR as the cooldown onset. The decay phase $[a_1, a_2]$ is excluded because LR variations during intermediate phases have limited effect on the final loss (Ibrahim et al., 2024). This information is instead captured by the escape feature $\int_0^{a_2} \eta_t'^2$, and the ablation in Appendix Sec. A.4 confirms that additionally including the decay $[a_1, a_2]$ in the convergence integral does not improve prediction. For the escape terms, we set $a_{e_1} = a_{e_2} = a_2$, so that the first escape integral covers warmup and decay jointly, while the second covers cooldown (the intervening plateau has $\eta' = 0$).

Table 1: Held-out benchmark (5-fold configuration-level cross-validation). All five baselines and the proposed method are evaluated under the same outer-fold protocol. Higher R^2 , Spearman, and Top-2 are better; lower Rel.Err. and Regret are better. Metric definitions (Top- k Hit Rate, Regret) are given in Appendix Sec. A.2.1. #p counts fitted coefficients, including the intercept.

Method	#p	R^2	Rel.Err.(%)	Spearman	Top-2 (%)	Regret
Constant (block mean)	–	0.991	1.08	–0.29	3	0.103
Chinchilla ($A/N^\alpha + B/D^\beta + E$)	5	0.988	1.28	–0.16	3	0.103
Linear regression	4	0.556	9.51	0.38	54	0.021
Tissue	7	0.973	1.81	0.61	74	0.012
Simplified + Chin. scale	11	0.992	1.01	0.68	77	0.008
Generalized Opt-Law	16	0.998	0.50	0.84	94	0.003

Evaluation protocol. The loss grids in Fig. 2 contain multiple (model size, token budget) blocks, each comprising several hyper-parameter configurations (peak LR, warmup steps). We perform 5-fold cross-validation by partitioning the configurations within each block into five folds, so that every fold contains held-out samples from all blocks. The exponent vector α and linear coefficients \mathbf{c} are fitted on the training folds only. Divergent runs are identified separately by the criterion in Eqn. (4) and excluded from the loss regression, but retained for fitting and evaluating the divergence criterion itself.

Fig. 5 compares the actual and predicted loss grids for one representative fold, where dashed-border cells denote held-out configurations. Within each block, the predicted surface correctly identifies the low-loss region and reproduces the sensitivity to peak LR and warmup steps. The predicted loss for held-out cells closely matches the actual loss, confirming that the law generalizes to unseen configurations. By construction, the predicted surface is smooth and does not reproduce local irregularities in the empirical grid, but this property is desirable for schedule selection as it filters out per-run noise and yields a stable ranking. Divergent configurations, flagged by the R criterion with a sentinel value of 7, align well with the observed divergence boundaries. Quantitative metrics aggregated across all five folds are reported in Table 1.

We compare against five baselines, ranging from a parameter-free constant predictor to a schedule-aware cross-scale model. The *Constant* baseline predicts the per-block mean loss (high R^2 but no within-block ranking). The *Chinchilla* baseline (Hoffmann et al., 2022) uses the standard power-law form without schedule-dependent features. *Linear regression* uses normalized (η_{\max}, a_1, N, S) as inputs. The *Tissue* baseline uses the cross-scale formula of Tissue et al. (2025), which combines cumulative learning-rate and annealing-area features with a model-size interaction term. Because the between-block variation in loss (driven by model size and token budget) dominates R^2 , a high R^2 does not guarantee accurate within-block ranking of hyper-parameter configurations. The selection-oriented metrics (Spearman, Top-2, Regret) directly measure this ranking quality and are therefore more informative for practical schedule selection.

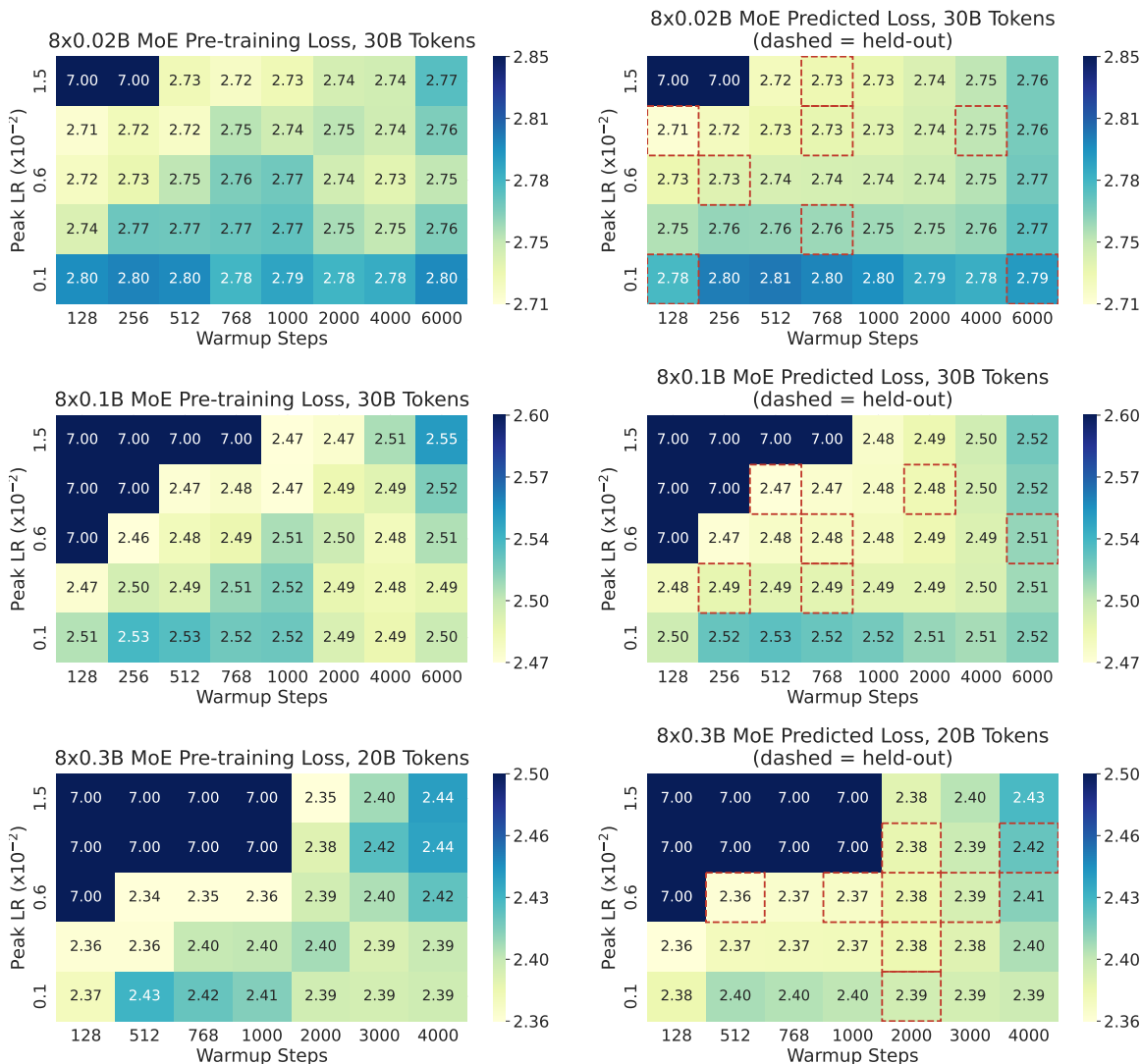


Figure 5: Actual training loss (left) versus predictions from generalized Opt-Laws (right) across model sizes and token budgets. Dashed-border cells are held out in the displayed fold. Divergent runs (sentinel value 7) are flagged by the R criterion. The predicted surface correctly ranks configurations within each block, with held-out cells closely matching their actual values.

On all five performance metrics, the generalized Opt-Laws improves upon all baselines. The Constant and Chinchilla baselines model only scale factors (N , S) without schedule-dependent features. Despite achieving $R^2 > 0.988$, their Spearman correlation is near zero, as they lack the capacity to rank configurations within the same (model size, token budget) block. Linear regression incorporates schedule variables (η_{\max} , a_1) but uses a linear combination that cannot capture the nonlinear trade-off between convergence and escape. The Tissue baseline introduces cumulative learning-rate and annealing-area features, yielding moderate ranking ability (Top-2 74%), but does not include escape or convergence-escape interaction terms. The generalized Opt-Laws, whose features are derived from the SDE

convergence and escape bounds, achieves Top-2 94% and Regret 0.003, meaning that the selected configuration is the best or second-best in nearly all blocks and the expected sub-optimality in loss is below 0.3%. Progressive ablation (Appendix Sec. A.4) corroborates this result, showing that each feature block contributes independent predictive signal.

As a separate classification task, divergence prediction is evaluated on all 260 training-grid configurations. The R criterion achieves precision=0.96, recall=0.88, F1=0.92, and balanced accuracy=0.94, substantially outperforming a peak-LR threshold (F1=0.38) and logistic regression (F1=0.54). The full comparison is reported in Appendix Table 12.

5 Evaluation beyond the Training Grid

This section evaluates the generalized Opt-Laws beyond the training grid used for fitting. In all experiments, we used an $8 \times 0.6\text{B}$ MoE model (Zhao et al., 2024; Wei et al., 2024) with approximately 4B trainable parameters. Additionally, $8 \times 0.1\text{B}$ and $8 \times 0.3\text{B}$ MoE models, containing 0.5B and 2B learnable parameters, respectively, were employed in the pre-training experiments. All experiments were conducted with consistent token lengths and a batch size of 2048, using pre-training data sourced from the RedPajama-v2 dataset (Computer, 2023). For continual training, over 100B tokens from Chinese Common Crawl data were incorporated, while fine-tuning involved sampling an additional 60B+ tokens from the Stack-Repo Java code dataset (Shrivastava et al., 2023). Model configurations and fitted coefficients are provided in Appendix Sec. A.3.

Roadmap. The empirical results are organized in three parts. We first study actual-loss behavior under alternative schedule families (Sec. 5.1). We then evaluate cross-scale extrapolation in large-scale pre-training (Sec. 5.2). Finally, we present downstream ranking studies in continual training (Sec. 5.3) and fine-tuning (Sec. 5.4). Each subsection below explicitly separates the description of observed loss behavior from the quantitative evaluation of prediction and selection quality.

5.1 Effects of Learning Rate Schedules

This subsection compares three LR schedule families (linear decay, cosine decay, and constant-plus-linear decay) across data scales of 3B, 10B, and 100B tokens. The corresponding cross-family prediction accuracy is evaluated quantitatively at the end of Sec. 5.2. Each schedule began with a linear warmup phase, gradually increasing from zero to a peak LR, η_{\max} . The specific mathematical formulations are provided in Eqn. (2) and Eqn. (3).

As shown in Fig. 6, the three schedule families produce notably different final losses at the 3B token scale, where the constant-plus-linear schedule achieves the lowest loss. As the training data increases to 10B and 100B tokens, the gap across families narrows, consistent with the analysis in Sec. 3.3.2: a larger token budget increases $\int \eta dt$ for all families, making the convergence terms dominant and reducing the relative contribution of the escape terms that differentiate the schedules.

However, this narrowing is slower for larger models. Comparing the $8 \times 0.1\text{B}$ results (Fig. 6(b,c)) with the $8 \times 0.6\text{B}$ results (Fig. 6(e,f)) at matched token budgets, the larger model retains a wider loss spread across schedule families. For instance, at 10B tokens the cosine and linear schedules nearly converge for the $8 \times 0.1\text{B}$ model, but still differ visibly for

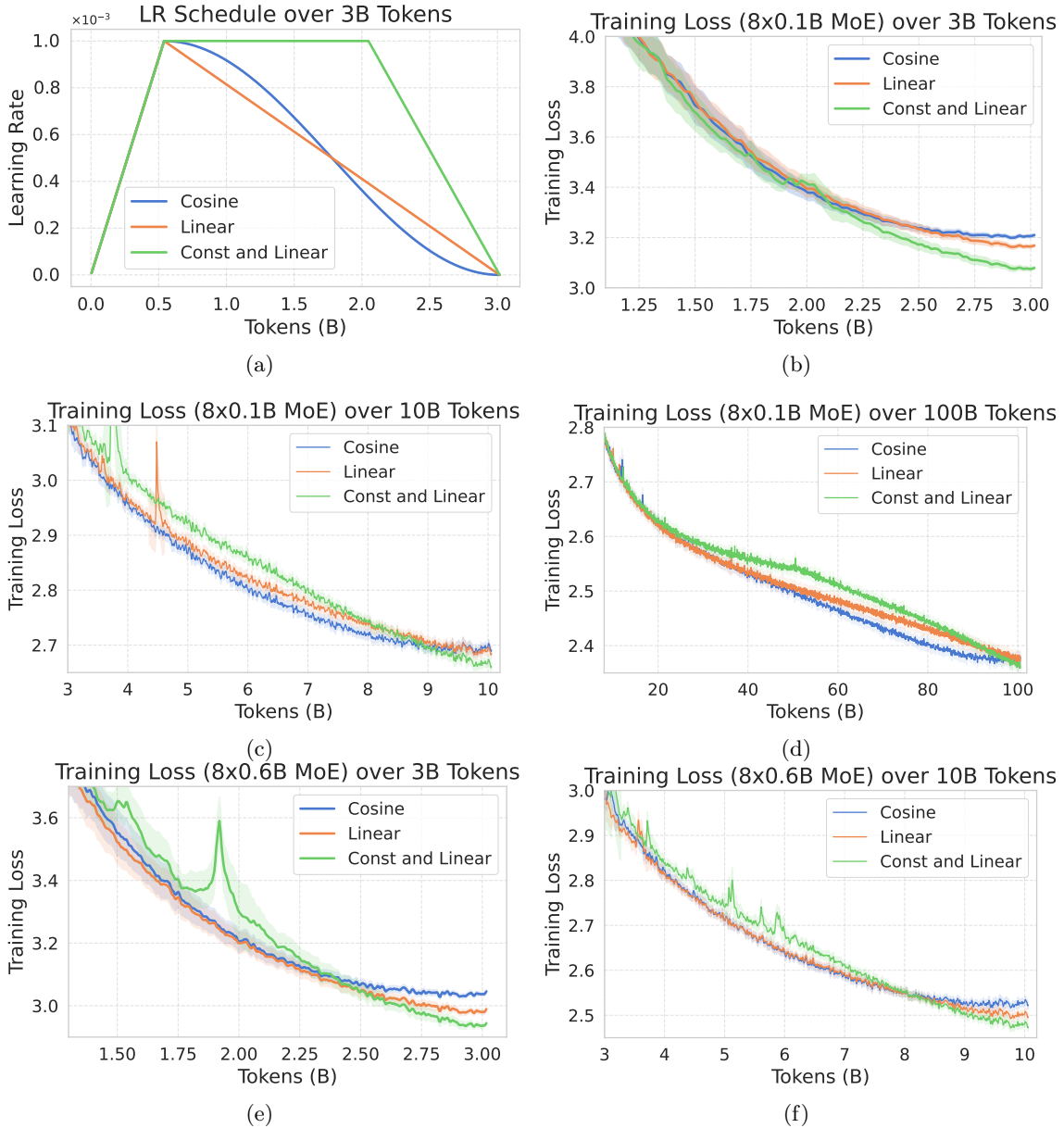


Figure 6: Training loss comparison for $8 \times 0.1\text{B}$ and $8 \times 0.6\text{B}$ MoEs under three LR schedules (linear decay, cosine decay, and constant followed by linear decay) across pre-training scales of 3B, 10B, and 100B tokens. The loss gap across schedule families is larger at smaller token budgets and closes more slowly for the larger model.

the $8 \times 0.6\text{B}$ model. This is expected from the Opt-Laws perspective: the convergence terms scale with $N / \int \eta$, so a larger N amplifies the schedule sensitivity at the same token budget.

Among the families, linear decay consistently achieves a slightly lower final loss than cosine decay at equal token budgets (Fig. 6(b,c)). The two schedules share the same convergence integral $\int \eta dt$ but differ in the escape term $\int \eta_t^2$: the linear schedule has a

Table 2: Actual versus predicted pre-training loss for the $8\times 0.6\text{B}$ and $8\times 0.3\text{B}$ MoE models at 100B–300B tokens. Three groups are tested: single-phase schedules at 300B tokens, multi-phase schedules at 100B tokens, and loss-equivalent schedules identified by inverse design. All prediction errors are below 0.5%.

Configuration		LR Schedule Parameters					Loss		
Model	Tokens	η_1	η_2	a_1	a_2	a_3	Actual	Predicted	Err. (%)
<i>300B tokens — single-phase schedules</i>									
$8\times 0.6\text{B}$	300B	10^{-3}	10^{-3}	500	500	500	1.985	1.984	0.04
$8\times 0.6\text{B}$	300B	6×10^{-3}	6×10^{-3}	2000	2000	2000	1.996	1.995	0.05
$8\times 0.3\text{B}$	300B	6×10^{-3}	6×10^{-3}	500	500	500	2.073	2.073	0.00
<i>100B tokens — multi-phase schedules</i>									
$8\times 0.6\text{B}$	100B	6×10^{-4}	6×10^{-4}	1200	1200	10000	2.076	2.075	0.04
$8\times 0.6\text{B}$	100B	1.2×10^{-3}	6×10^{-4}	1200	7000	13000	2.098	2.095	0.13
$8\times 0.6\text{B}$	100B	1.2×10^{-3}	6×10^{-4}	1200	5000	11500	2.097	2.095	0.08
$8\times 0.6\text{B}$	100B	10^{-3}	5×10^{-4}	5000	10000	15000	2.057	2.064	0.35
<i>100B tokens — loss-equivalent schedules</i>									
$8\times 0.6\text{B}$	100B	10^{-3}	10^{-3}	2000	2000	2000	2.077	2.078	0.05
$8\times 0.6\text{B}$	100B	10^{-3}	5×10^{-4}	2450	7000	12000	2.079	2.080	0.05
$8\times 0.6\text{B}$	100B	5×10^{-5}	5×10^{-4}	1000	1000	9500	2.077	2.078	0.05

smaller derivative integral, corresponding to a lower trapping probability under the escape analysis (Sec. 3.3.2). The observed loss difference is consistent with this prediction.

These results confirm that the convergence-escape decomposition in Opt-Laws captures the key factors governing schedule selection: data volume controls the convergence terms, model scale modulates their sensitivity, and the escape terms account for residual differences among families with matched convergence budgets.

5.2 Pre-training Extrapolation

In this subsection, we evaluate generalized Opt-Laws as an extrapolation predictor for large-scale pre-training. The law is fitted on the small-scale piecewise-linear grid (Sec. 4.3) and applied without re-fitting to larger models, larger token budgets, and more complex schedule shapes.

We consider an $8\times 0.6\text{B}$ and an $8\times 0.3\text{B}$ MoE model, pre-trained on up to 300B tokens. Table 2 reports the actual and predicted final losses across three groups of configurations with varied LRs η_1 , η_2 and schedule parameters a_1 , a_2 , a_3 (Fig. 4). The fitted exponents and coefficients are listed in Appendix Sec. A.3.

The first group in Table 2 evaluates predictions at 300B tokens under simple warmup-plus-cooldown schedules. Across different model sizes and peak LRs, prediction errors remain below 0.2%. The second group tests multi-phase piecewise-linear schedules at 100B tokens. Despite the increased schedule complexity, all errors stay below 0.5%. These results

Table 3: Baseline comparison for pre-training extrapolation. All methods are fitted on the small-scale training grid (Table 7) and evaluated on the configurations in Table 2 without re-fitting. Mean relative error (%) is reported per group.

Method	Per-Group Rel. Err. (%)			
	300B-SP (3)	100B-MP (4)	100B-LE (3)	All (10)
Linear regression	63.8	44.8	44.7	50.8
Tissue cross-scale	11.3	9.7	10.2	10.3
Simplified + Chin. scale	8.9	6.9	7.2	7.6
Generalized Opt-Law	0.1	0.2	0.2	0.2

SP: single-phase ; MP: multi-phase ; LE: loss-equivalent.

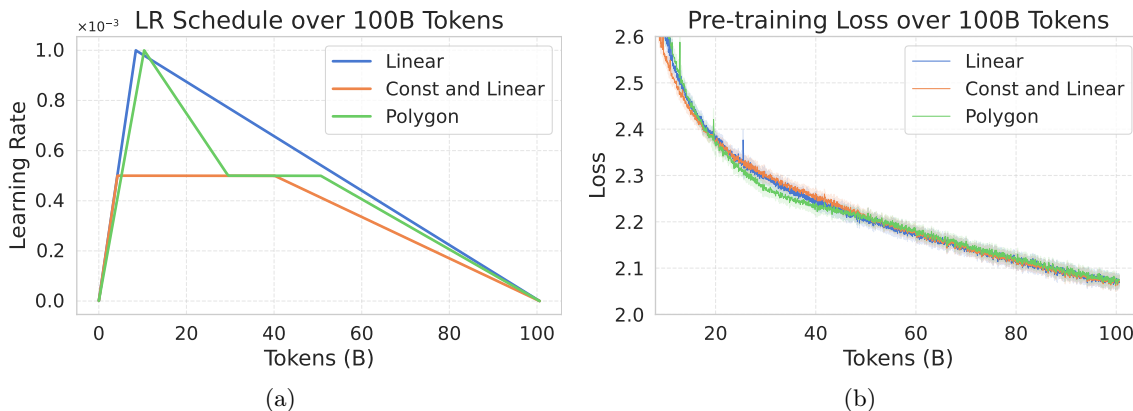


Figure 7: (a) Three LR schedules for the $8 \times 0.6B$ model on 100B tokens, selected by inverse design to yield the same predicted loss. (b) The corresponding training loss curves. The final losses converge to nearly the same value, confirming that Opt-Laws correctly identifies loss-equivalent configurations.

are obtained without re-fitting, confirming that the small-scale calibration transfers to configurations well beyond the training grid.

As a further test, we used generalized Opt-Laws to infer specific combinations of η_1 , η_2 , a_1 , a_2 , and a_3 (last three rows of Table 2) that would yield the same predicted loss. We then pre-trained the $8 \times 0.6B$ MoE on 100B tokens using these schedules. Fig. 7 shows that the training losses converge to nearly the same final value across all three schedules, confirming that the law correctly identifies loss-equivalent configurations even when the schedules differ substantially in shape.

Table 3 compares the generalized Opt-Laws against three schedule-aware baselines on the same Table 2 configurations. All methods are fitted on the small-scale training grid, which contains only linear warmup-plus-cooldown schedules, and are evaluated without re-fitting. Linear regression uses (η_{\max}, a_1, N, S) as inputs and produces mean errors above 44%, as the linear form cannot capture the nonlinear relationship between schedule features and

loss at new scales. The Tissue cross-scale baseline incorporates cumulative learning rate and annealing features, reducing errors to approximately 10%, but its functional form does not separate convergence and escape contributions, limiting extrapolation precision. The simplified Opt-Law with Chinchilla-style scale terms achieves 7–9% errors. By contrast, the generalized Opt-Laws maintains errors below 0.5% on all three groups. The gap widens at 300B tokens (0.1% vs. 8.9–63.8%), where the extrapolation distance from the training grid is largest, suggesting that the SDE-derived convergence-escape decomposition provides a more robust basis for cross-scale transfer than the features used by the baselines.

Schedule-family generalization. All results above involve piecewise-linear schedules. The training grid contains only linear warmup-plus-cooldown schedules, and the Table 2 configurations extend this to multi-phase piecewise-linear variants. To test generalization to entirely different schedule shapes, we evaluate the generalized Opt-Laws on cosine and constant-plus-linear schedules. The generalized Opt-Laws correctly identifies the optimal schedule family in all five evaluated groups, with prediction errors below 2%. The detailed per-group results are reported in Appendix Table 13. This cross-family transfer reflects the design of the feature construction: the convergence and escape features capture the mechanisms through which the schedule affects training, rather than the parametric form of the schedule itself. Specifically, $\int \eta$ measures how much total learning the optimizer accumulates, and $\int \eta_t'^2$ measures how aggressively the learning rate changes during warmup and cooldown. Different families that deliver similar values of these quantities produce similar predicted losses. We do not claim universal validity for arbitrary schedules, but these results provide evidence that the SDE-derived features are not restricted to the family used for fitting.

5.3 Continual-Training Ranking

This subsection evaluates whether the generalized Opt-Laws can rank candidate LR schedules for continual training, where a pre-trained model is further trained on new data with a re-warmed learning rate.

We use an 8×0.6 B MoE model pre-trained on 300B English tokens from the RedPajama-v2 dataset (Table 2, row one). We evaluate two scenarios: strong distribution shift (100B Chinese tokens) and weak distribution shift (100B English tokens).

Since the model starts from a pre-trained checkpoint rather than from scratch, the generalized Opt-Laws must account for the optimization history. For the convergence term, the cumulative optimization budget should reflect both stages: if pre-training already accumulated a large $\int \eta^{pre}$, the model is closer to a local minimum and the marginal effect of the continual-training schedule differs from that of training from scratch. We therefore define the history-aware convergence integral as

$$\int_0^{a_{c_1}^{ct}} \eta_t dt = \int_0^{S^{pre}} \eta_t^{pre} dt + \int_0^{a_{c_1}^{ct}} \eta_t^{ct} dt.$$

For the escape term, the pre-training schedule is already finished and contributes no derivatives during continual training, so only the current-stage schedule shape enters. In the pre-training feature construction, the effect of η_{\max} on the escape term is implicitly absorbed by the fitted coefficients together with the scale feature $\eta_{\max}^{\alpha_{12}}$. In continual training,

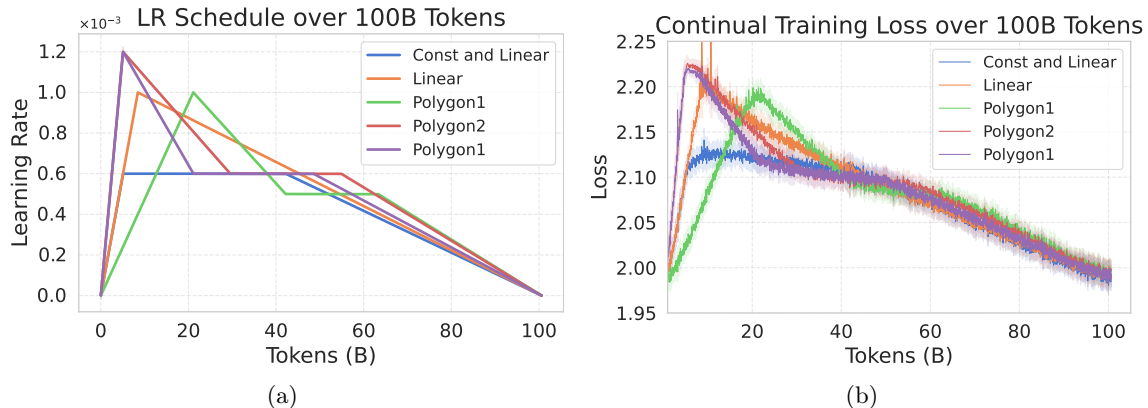


Figure 8: (a) Five LR schedules for continual training of the $8\times 0.6B$ model on 100B English tokens (weak distribution shift). (b) The corresponding loss curves. Final losses are closely clustered despite substantial schedule variation.

Table 4: Ranking evaluation for continual training of the $8\times 0.6B$ model on 100B tokens under strong shift (Chinese) and weak shift (English). Rank (Act./Pred.): actual versus predicted rank. Pred. Score is used for ranking only; lower score indicates lower predicted loss.

Schedule	LR Parameters					Obs.	Pred.	Rank	
	η_1	η_2	a_1	a_2	a_3	Loss	Score	Act.	Pred.
<i>Strong distribution shift ($8\times 0.6B$, 100B Chinese tokens)</i>									
① Polygon1	10^{-3}	5×10^{-4}	5000	10000	15000	1.826	2.058	3	3
② Polygon2	1.2×10^{-3}	6×10^{-4}	1200	7000	13000	1.821	2.014	2	2
③ Linear	10^{-3}	10^{-3}	2000	2000	2000	1.818	1.975	1	1
<i>Weak distribution shift ($8\times 0.6B$, 100B English tokens; near-tie)</i>									
④ Const+Linear	6×10^{-4}	6×10^{-4}	1200	1200	10000	1.991	1.995	1	2
⑤ Linear	10^{-3}	—	2000	2000	2000	1.992	1.975	2	1
⑥ Polygon1v2	1.2×10^{-3}	6×10^{-4}	1200	5000	11500	1.993	2.010	3	3
⑦ Polygon2	1.2×10^{-3}	6×10^{-4}	1200	7000	13000	1.995	2.017	4	4
⑧ Polygon1	10^{-3}	5×10^{-4}	5000	10000	15000	1.996	2.059	5	5

however, the coefficients are not re-fitted, and the re-warmed peak LR may lie outside the pre-training range. To ensure the escape feature remains comparable under different LR scales, we use the normalized form $\int_{a_{e2}}^S \eta_t^2 / \eta_{\max}^4$ directly, following the ratio that appears in the escape bound (Theorems 3 and 4).

In the strong-shift scenario, we used 100B tokens of Chinese common crawl data, mixed with 5% of the original English data as replay (Parmar et al., 2024; Guo et al., 2024; Ke et al., 2023). The observed losses are well separated (spread $>0.4\%$), and the modified Opt-Laws recovers the exact 1–2–3 ranking (Table 4, top). The linear schedule achieves the lowest

Table 5: Fine-tuning ranking evaluation for the 8×0.6B model at 3B, 30B, and 60B tokens. Rank (Act./Pred.) denotes actual versus predicted rank out of 3 candidates per token budget. Lower Pred. Score indicates a schedule predicted to achieve lower loss. All runs use warmup-and-decay schedules except ③ in the 60B group (two-phase). The predicted ranking matches the actual ranking in all nine configurations.

Schedule	LR Parameters			Observed	Predicted	Rank	
	η_{\max}	a_1	a_3	Loss	Score	Act.	Pred.
<i>3B tokens — small-scale fine-tuning</i>							
① Linear-S	5×10^{-4}	128	128	0.920	2.302	3	3
② Linear-L	10^{-3}	512	512	0.909	2.158	2	2
③ Linear-H	1.5×10^{-3}	128	128	0.904	2.102	1	1
<i>30B tokens — medium-scale fine-tuning</i>							
① Linear-S	5×10^{-4}	128	128	0.857	2.116	3	3
② Linear-L	10^{-3}	512	512	0.849	2.028	2	2
③ Linear-H	1.5×10^{-3}	128	128	0.847	2.004	1	1
<i>60B tokens — large-scale fine-tuning (mixed schedules)</i>							
① Linear-S	5×10^{-4}	128	128	0.822	2.052	2	2
② Linear-H	2×10^{-3}	512	512	0.817	1.972	1	1
③ Two-phase	3×10^{-4}	128	7000	0.826	2.178	3	3

loss, followed by Polygon2 and Polygon1. Notably, this ranking differs from the pre-training ranking under the same schedules, confirming that the history-aware modification captures the changed optimization dynamics rather than simply reproducing the pre-training ordering.

In the weak-shift scenario, we sampled 100B English tokens and tested five LR schedules (Fig. 8). The final losses differ by only 0.005 (0.25% relative), consistent with prior observations that schedule choice has limited impact under small distribution shift (Ibrahim et al., 2024). The predicted scores correctly recover positions 3–5, while the top two schedules are separated by only 0.001 in observed loss (Table 4, bottom). This near-tie setting illustrates the resolution limit of the fitted law.

In both scenarios, the history-aware Opt-Laws produces correct rankings wherever the observed loss differences are resolvable, providing reliable schedule selection for continual training.

5.4 Fine-Tuning Ranking

This subsection extends the ranking evaluation to fine-tuning, the final stage of a multi-stage training pipeline. In practice, production LLMs are typically not fine-tuned directly from a base pre-training checkpoint (Dubey et al., 2024). Continual training on domain-specific corpora usually precedes task-level fine-tuning, so we test the history-aware Opt-Laws on the full three-stage pipeline (pre-training → continual pre-training → fine-tuning), evaluating whether the law remains effective after multiple training stages and data shifts.

In our experiments, we fine-tuned an $8 \times 0.6\text{B}$ MoE model on the Stack-Repo Java code dataset. Prior to fine-tuning, the model had been pre-trained on 300B English tokens and subsequently underwent continual training on 100B Chinese tokens. We conducted fine-tuning with three token budgets (3B, 30B, and 60B) across three LR schedules per budget, as detailed in Table 5.

Following the same history-aware approach as in Sec. 5.3, the convergence integral accumulates the optimization budget from all preceding stages: $\int_0^{a_{c1}^{ft}} \eta_t dt = \int_0^{S^{pre}} \eta_t^{pre} dt + \int_0^{S^{ct}} \eta_t^{ct} dt + \int_0^{a_{c1}^{ft}} \eta_t^{ft} dt$. The escape term uses the current-stage schedule only, with the same η_{\max}^4 normalization as in Sec. 5.3.

At 3B and 30B tokens, the predicted scores correctly rank all three candidates (Table 5). The predicted score gap between the best and worst schedule narrows from 0.20 at 3B to 0.11 at 30B, mirroring the observed loss gap (0.016 at 3B versus 0.010 at 30B). This parallel narrowing indicates that the law not only preserves the ranking but also tracks the diminishing sensitivity of loss to schedule choice as the fine-tuning budget grows. At 60B tokens, one candidate (③) uses a two-phase schedule rather than simple warmup-and-decay. The law still correctly identifies the best and worst candidates, indicating that the history-aware construction generalizes across schedule types even after three training stages. Across all nine fine-tuning configurations, the predicted and actual rankings agree perfectly.

These results demonstrate that the history-aware Opt-Laws retains ranking utility across a realistic multi-stage pipeline spanning pre-training, continual training, and fine-tuning.

6 SDE Analysis behind Opt-Laws

This section presents the SDE-based analysis that motivates the feature construction in Secs. 3–4. We analyze the training dynamics of non-convex smooth optimization problems for both SGD and Adam (Kingma and Ba, 2014), modeling them as SDEs to capture the effects of time-varying learning rates.

Our analysis examines the influence of key hyper-parameters, including the LR schedule $\eta(t)$, data size D , and model size N , on two critical aspects: convergence speed and the ability to escape suboptimal local minima. Notably, we observe that both SGD and Adam yield similar forms in their bounds related to these hyper-parameters. This similarity allows us to generalize Opt-Laws, encapsulating the relationship between these factors and the final training loss, thereby offering deeper insights into the optimization process.

While existing research frequently uses SDEs to model optimization processes and analyze convergence (Li et al., 2017; Soto et al., 2022; Dambrine et al., 2024), or to study escape time from local minima (e.g., the Eyring–Kramers law (Berglund and Gentz, 2013; Bovier and Den Hollander, 2015)), these studies are predominantly restricted to convex problems, quadratic objectives, or fixed learning rates. In contrast, our work extends to general non-convex smooth problems with time-varying LRs, thus leading to a nonlinear, time-inhomogeneous SDE. This added complexity precludes the direct application of existing results. Our contributions address these new theoretical challenges, providing novel insights into the optimization of LLMs under more general conditions.

6.1 Optimization Methods and SDEs

We study the following non-convex optimization problem:

$$\min_{\mathbf{x}} f(\mathbf{x}) := \mathbb{E}_{\zeta \sim \mathcal{D}}[F(\mathbf{x}, \zeta)], \quad (9)$$

where the objective function $F(\cdot, \cdot)$ is differentiable and possibly non-convex, data ζ is drawn from an unknown data distribution \mathcal{D} , \mathbf{x} is the learnable parameters. The formulation Eqn. (9) encapsulates a large body of machine learning problems, e.g., LLM training problems, and least square regression. For SGD, the update scheme is as follows:

$$\mathbf{x}_{k+1} = \mathbf{x}_k - \eta_0 \eta_k \tilde{\mathbf{g}}_k, \quad (\text{SGD})$$

where gradient estimate $\tilde{\mathbf{g}}_k$ is defined as $\tilde{\mathbf{g}}_k := \nabla f(\mathbf{x}_k) + \mathbf{z}_k$, with a LR of $\eta_0 \eta_k$, where η_0 is a small rescaling parameter and η_k is the normalized LR. This choice of LR facilitates the derivation of the corresponding SDE. Following previous work (Zhu et al., 2019; Malladi et al., 2022; Xie et al., 2020; Zhou et al., 2024b), we assume $\mathbf{z}_k \sim \mathcal{N}(0, \Sigma(\mathbf{x}_k))$, where

$$\Sigma(\mathbf{x}_k) := \frac{1}{B} \left(\frac{1}{D} \sum_{i=1}^D (\nabla F(\mathbf{x}_k, \zeta_i) - \nabla f(\mathbf{x}_k)) (\nabla F(\mathbf{x}_k, \zeta_i) - \nabla f(\mathbf{x}_k))^\top \right). \quad (10)$$

We should mention that the exact characterization of the noise \mathbf{z}_k in stochastic optimization remains unresolved (Simsekli et al., 2019; Zhang et al., 2021). For analytical convenience, here we adopt a Gaussian noise assumption, acknowledging that determining the precise stochastic process of the noise during LLM training is beyond the scope of this work.

Under mild conditions, SGD can be approximated by an Itô-SDE, where the noise is modeled by Brownian motion, as derived via the Euler-Maruyama method in Sec. B.1.2:

$$d\mathbf{X}_t = -\eta(t) \nabla f(\mathbf{X}_t) dt + \sqrt{\eta_0 \eta(t)} \sigma(\mathbf{X}_t) d\mathbf{W}_t. \quad (\text{SGD-SDE})$$

where \mathbf{W}_t is a Wiener process, $\sigma : \mathbb{R}^N \rightarrow \mathbb{R}^{N \times N}$ is defined as $\sigma(\mathbf{x}) := \sqrt{\Sigma(\mathbf{x})}$, $\eta(t)$ is the normalized LR schedule, and η_0 is a small rescaling parameter. Specifically, $\eta_0 \cdot \eta(t)$ corresponds to the original LR schedule.

Similarly, the dynamics of the Adam can be approximated using a lifted Itô-SDE. The algorithmic steps for Adam are presented as follows:

$$\begin{cases} \mathbf{x}_{k+1} = \mathbf{x}_k - \eta_0 \eta_k \mathbf{m}_k \odot (\mathbf{v}_k + \epsilon)^{-\frac{1}{2}}, \\ \mathbf{m}_{k+1} = (1 - \beta_{1,k}) \mathbf{m}_k + \beta_{1,k} \tilde{\mathbf{g}}_{k+1}, \\ \mathbf{v}_{k+1} = (1 - \beta_{2,k}) \mathbf{v}_k + \beta_{2,k} \tilde{\mathbf{g}}_{k+1}^2, \end{cases} \quad (\text{Adam})$$

where \odot denotes the element-wise product, with $\beta_{1,k}, \beta_{2,k} \in (0, 1)$ and initial conditions $\mathbf{m}_0 = \mathbf{v}_0 = \mathbf{0}$. The parameter ϵ prevents degeneracy. In practice, both $\beta_{1,k}$ and $\beta_{2,k}$ are typically close to 1. To facilitate SDE-based analysis, we use the parameters $\beta_{1,k} = 1 - \hat{c}_1 \eta_k$ and $\beta_{2,k} = 1 - \hat{c}_2 \eta_k$, following a single-time scale scheme (Ding et al., 2023; Shen and Chen, 2022; Xiao et al., 2023), where \hat{c}_1 and \hat{c}_2 are small constants. The resulting Itô-SDE for Adam's dynamics is:

$$\begin{cases} d\mathbf{X}_t = -\eta(t) \mathbf{m}_t \odot (\mathbf{v}_t + \epsilon)^{-\frac{1}{2}} dt, \\ d\mathbf{m}_t = -c_1 \eta(t) (\mathbf{m}_t - \nabla f(\mathbf{X}_t)) dt + c_1' \eta(t) \sigma(\mathbf{X}_t) d\mathbf{W}_t, \\ d\mathbf{v}_t = -c_2 \eta(t) (\mathbf{v}_t - \text{diag}(\Sigma(\mathbf{X}_t))) dt, \end{cases} \quad (\text{Adam-SDE})$$

where c_1, c'_1 , and c_2 are constants. The notation $\text{diag}(\mathbf{M})$ refers to the vector formed by the diagonal elements of matrix \mathbf{M} , while $\text{Diag}(\mathbf{v})$ denotes the diagonal matrix with the entries of \mathbf{v} on its diagonal. Given the initial condition $\mathbf{v}_0 = \mathbf{0}$, the solution for \mathbf{v}_t is:

$$\mathbf{v}_t = \exp\left(-c_2 \int_0^t \eta(s) ds\right) \left[\int_0^t \exp\left(c_2 \int_0^s \eta(\tau) d\tau\right) c_2 \eta(s) \mathbf{d}_s ds \right],$$

where $\mathbf{d}_t := \text{diag}(\boldsymbol{\Sigma}(\mathbf{X}_t))$. This formulation ensures that \mathbf{v}_t remains nonnegative throughout the process.

6.2 Inspiration from Convergence Guarantee

In this subsection, we analyze the convergence properties of (SGD-SDE) and (Adam-SDE) in the context of non-convex smooth problems, deriving the mathematical formula for the convergence component of Opt-Laws. To present these results rigorously, we first provide several mild assumptions. In the following discussion, the notation $\|\cdot\|$ denotes the Euclidean norm when applied to vectors and the Frobenius norm when applied to matrices. While $\|\cdot\|_{\text{op}}$ denotes the operator norm for matrix.

Assumption 1 (L-smoothness) *The function $f(\cdot)$ is L -smooth with respect to the parameters, namely,*

$$\|\nabla f(\mathbf{x}) - \nabla f(\mathbf{y})\| \leq L\|\mathbf{x} - \mathbf{y}\|, \quad \forall \mathbf{x}, \mathbf{y} \in \mathbb{R}^N.$$

Assumption 2 (Unbiased Estimator) *Given any $\mathbf{x} \in \mathbb{R}^N$, we assume that the entries of $\nabla F(\mathbf{x}, \zeta_i) - \nabla f(\mathbf{x})$ are i.i.d. Gaussians $\mathcal{N}(0, \boldsymbol{\Sigma}_g)$ for all $i \in [D]$, where $\boldsymbol{\Sigma}_g$ is given.*

Assumption 1 asserts that the objective function of our optimization problem is L -smooth. This is a standard and mild assumption in the stochastic optimization literature, which facilitates the determination of specific convergence rates for optimization algorithms, a task that is otherwise challenging (Arjevani et al., 2022; Guo et al., 2021; Li and Lin, 2022; Xie et al., 2022, 2024b,a; Zhou et al., 2024a). Assumption 2 stipulates that the noise introduced by different data points during the estimation of the gradient is unbiased and independent, given the weights of LLMs. This assumption is also common, especially when the Langevin diffusion is employed to analyze the behavior of SGD (Jastrzēbski et al., 2017; He et al., 2019; Xie et al., 2020). Notably, we do not assume that the gradient estimation noise originates from an oracle distribution $\mathcal{N}(0, \boldsymbol{\Sigma})$. As indicated in Eqn. (10), the covariance matrix encountered during actual training is not $\mathbb{E}_{\zeta \sim \mathcal{D}}[(\nabla F(\mathbf{x}, \zeta_i) - \nabla f(\mathbf{x}))(\nabla F(\mathbf{x}, \zeta_j) - \nabla f(\mathbf{x}))^\top]$.

Under these assumptions, we derive a concentration inequality for the trace of the covariance matrix $\boldsymbol{\Sigma}(\mathbf{x}_k)$ defined in Eqn. (10), which is helpful for the following analysis. In this work, the batch size B is fixed. For simplicity, we assume $B = 1$ throughout the analysis. However, the results are readily adaptable to any fixed positive batch size B .

Proposition 2 (Trace Boundedness) *Suppose Assumption 2 holds. Given any point $\mathbf{x} \in \mathbb{R}^N$ and a positive $t > 0$, the covariance matrix in Eqn. (10) satisfies*

$$\mathbb{P}\left(|\text{Tr}(\boldsymbol{\Sigma}(\mathbf{x})) - \text{Tr}(\boldsymbol{\Sigma}_g)| \geq t\right) \leq 2 \exp\left(-\frac{Dt^2}{4 \text{Tr}(\boldsymbol{\Sigma}_g^2) + 2t\sigma_g^2}\right),$$

where D is the number of samples and $\sigma_g := \lambda_{\max}\left(\boldsymbol{\Sigma}_g^{\frac{1}{2}}\right)$ is the largest eigenvalue of $\boldsymbol{\Sigma}_g^{\frac{1}{2}}$.

We can also estimate the maximal eigenvalue of the random matrix $\Sigma(\mathbf{x})$ by random matrix theory.

Proposition 3 (Covariance Boundedness) *Suppose Assumption 2 holds, then the covariance matrix in Eqn. (10) satisfies*

$$\sup_{\mathbf{x} \in \mathbb{R}^N} \mathbb{E} [\lambda_{\max}(\Sigma(\mathbf{x}))] \leq \left(1 + \sqrt{\frac{D}{N}}\right) \sigma_g^2 + \frac{C\sigma_g^2}{N^{2/3}}.$$

where $C > 0$ is a constant independent of N , the expectation is taken with respect to the Gaussian distribution $\mathcal{N}(0, \Sigma_g)$ specified in Assumption 2, and $\sigma_g := \lambda_{\max}\left(\Sigma_g^{\frac{1}{2}}\right)$.

Proposition 3 provides a non-asymptotic extension of the classical Marchenko-Pastur theorem (Bai and Silverstein, 2010; Ledoux and Rider, 2010) from random matrix theory, offering a more precise variance estimate based on the convergence of the largest eigenvalue of covariance matrices to $(1 + \sqrt{D/N})\sigma_g^2$. For most LLMs adhering to scaling laws, the ratio $D/N \gg 1$. Consequently, we can expect $\lambda_{\max}(\Sigma(\mathbf{x})) = \mathcal{O}\left(\sigma_g^2 \sqrt{D/N}\right)$ in expectation.

6.2.1 SGD CONVERGENCE ANALYSIS

With the smoothness and boundedness properties established, we can now derive the expected convergence rate of SGD-SDE for non-convex problems in terms of time-varying LR.

Theorem 1 (SGD Convergence Bound) *Suppose Assumptions 1 and 2 hold. For the dynamics described in (SGD-SDE), the following bound holds:*

$$\mathbb{E} \left[\overline{\|\nabla f(\mathbf{X}_t)\|^2} \right] \leq \frac{f(\mathbf{X}_0) - f_{\min}}{\int_0^t \eta(s) ds} + \frac{\eta_0 L \sigma_0^2 N \int_0^t \eta(s)^2 ds}{2 \int_0^t \eta(s) ds}, \quad (11)$$

where $\overline{\|\nabla f(\mathbf{X}_t)\|^2} := \frac{\int_0^t \eta(s) \|\nabla f(\mathbf{X}_s)\|^2 ds}{\int_0^t \eta(s) ds}$ and $f_{\min} := \min_{\mathbf{x} \in \mathbb{R}^N} f(\mathbf{x})$, and

$$\sigma_0 := \sigma_g \sqrt{\left(1 + \sqrt{\frac{D}{N}}\right) + \frac{C}{N^{2/3}}}.$$

It can be observed that the average squared norm of the gradient can be effectively upper bounded by a function of the training hyper-parameters. Given a maximal time horizon $T > 0$, the bound in Eqn. (11) achieves the optimal bound of $\mathcal{O}(1/\sqrt{T})$ when we select constant LR $\eta(t) = \mathcal{O}(1/\sqrt{T})$. This upper bound consists of two terms, both of which share the denominator of $\int_0^t \eta(s) ds$. Despite the complexity inherent in the numerator, the numerator of the first term is clearly of the order $\mathcal{O}(N)$, given that $f(\mathbf{X}_0) - f_{\min} \leq \frac{L}{2} \|\mathbf{X}_0 - \mathbf{X}^*\|^2$, where $\mathbf{X}^* \in \arg\min_{\mathbf{x}} f(\mathbf{x})$. The magnitude of the numerator in the second term is also $\mathcal{O}(N)$. Thus, the overall order of the average squared norm of the gradient is $\mathcal{O}(N / \int_0^t \eta(s) ds)$.

Practical interpretation. In non-convex optimization, finding a global minimum is generally intractable, and the standard convergence criterion is to reach an approximate stationary point. In the stochastic setting, the gradient norm at any single iterate is subject to mini-batch noise and serves as a poor convergence indicator. The averaged squared gradient norm (Ghadimi and Lan, 2013) smooths out this noise and measures how much time the trajectory spends in near-stationary regions, providing a robust trajectory-level convergence metric.

A small averaged gradient norm implies that the optimizer has largely converged to stationary points. Stochastic gradient methods almost surely avoid strict saddle points (Lee et al., 2019), so the stationary points reached in practice are local minima. For overparameterized neural networks, recent work shows that the loss landscape is benign: Chen et al. (2026) observe a basin-like structure in LLMs where performance remains stable within each basin and the basin expands with model scale, consistent with the broadening of the low-loss region observed in Figs. 1 and 2. These observations connect the averaged gradient norm to the final loss: convergence to a local minimum in a benign landscape yields a good loss.

Our convergence bound (Theorem 1) shows that the averaged gradient norm is controlled by $1/\int \eta$, which therefore serves as a natural surrogate for convergence speed in the feature construction. Under the Polyak–Łojasiewicz (PL) condition (Karimi et al., 2016), the qualitative chain above can be made quantitative: $\|\nabla f\|^2 \geq 2\mu(f - f_{\min})$ directly converts the gradient norm bound into a loss gap bound. Liu et al. (2022) show that overparameterized networks generically satisfy PL*, a variant of PL, providing theoretical grounding for this connection. Our feature construction relies on the qualitative relationship and does not require PL to hold.

6.2.2 ADAM CONVERGENCE ANALYSIS

We proceed to analyze the convergence of (Adam-SDE). Before delving into this analysis, we need to introduce an additional mild assumption, which is commonly employed in the study of stochastic first-order methods (Bertsekas and Tsitsiklis, 2000; Reddi et al., 2018).

Assumption 3 (Smoothness and Boundedness) *The function $f(\cdot)$ is smooth with respect to the parameters and the normalized LR schedule is bounded,*

1. $|f(\mathbf{x}) - f(\mathbf{y})| \leq \ell \|\mathbf{x} - \mathbf{y}\| \quad \forall \mathbf{x}, \mathbf{y} \in \mathbb{R}^N,$
2. $\int_0^\infty \eta(s) ds = \infty, \quad \int_0^\infty \eta^2(s) ds < \infty.$

Assumption 3.1 asserts global Lipschitz continuity, implying that the gradient of f is uniformly bounded. This is a common assumption in extensive literature on adaptive gradient methods (Reddi et al., 2018; Xiao et al., 2024; Xie et al., 2024b). Assumption 3.2 requires that the LR be non-summable but square summable, which is a fundamental assumption for ensuring the convergence of stochastic first-order methods (Bertsekas and Tsitsiklis, 2000; Davis et al., 2020). Based on this assumption, we first establish the boundedness of the (Adam-SDE) dynamics as follows. The boundedness helps to guarantee the convergence of (Adam-SDE). From Proposition 3, we can observe that the maximal eigenvalue of $\Sigma(\mathbf{x})$ can be bounded by $\mathcal{O}\left(\sigma_g^2 \sqrt{D/N}\right)$ in expectation. Based on this observation, we make the following stronger assumption than Assumption 2 to establish the convergence of Adam.

Assumption 4 *There exists $\bar{\sigma}$, such that $\lambda_{\max}(\Sigma(\mathbf{x})) \leq \bar{\sigma}$ for all $\mathbf{x} \in \mathbb{R}^N$.*

Proposition 4 (Dynamics Boundedness) *Suppose Assumptions 3 and 4 hold, then there exist positive constants M and V which are independent of N , such that*

$$\sup_{t \geq 0} \left\{ \mathbb{E} \left[\|\mathbf{m}_t\|^2 \right] \right\} \leq M^2 N, \quad \sup_{t \geq 0} \{\|\mathbf{v}_t\|_\infty\} \leq V.$$

This proposition demonstrates uniform bounds for \mathbf{m}_t and \mathbf{v}_t . The distinction is that the bound for \mathbf{v}_t is deterministic, whereas the bound for \mathbf{m}_t is in the sense of expectation. This is due to the SDE associated with \mathbf{m}_t involving a Brownian motion. Since both M and V are independent of N , the scales of \mathbf{m}_t and \mathbf{v}_t are matched in the sense that both $\mathbb{E}[\|\mathbf{m}_t\|^2]$ and $\mathbb{E}[\|\mathbf{v}_t\|^2]$ are of the order $\mathcal{O}(N)$.

Theorem 2 (Adam Convergence Bound) *Suppose Assumptions 1, 3 and 4 hold. For the dynamics of (Adam-SDE), the following bound holds:*

$$\mathbb{E} \left[\overline{\|\mathbf{m}_t\|^2} \right] \leq \frac{\sqrt{V+\epsilon} \left(f(\mathbf{X}_0) + \frac{1}{2c_1} \left\langle \frac{\mathbf{m}_0}{\sqrt{\mathbf{v}_0+\epsilon}}, \mathbf{m}_0 \right\rangle - f_{\min} \right) + \frac{(c'_1)^2 \bar{\sigma} \sqrt{V+\epsilon} \int_0^t \eta(s)^2 ds}{2c_1}}{\left(1 - \frac{c_2}{4c_1} \right) \int_0^t \eta(s) ds} + \frac{\frac{(c'_1)^2 \bar{\sigma} \sqrt{V+\epsilon} \int_0^t \eta(s)^2 ds}{2c_1}}{\left(1 - \frac{c_2}{4c_1} \right) \sqrt{\epsilon} \int_0^t \eta(s) ds}, \quad (12)$$

where $\overline{\|\mathbf{m}_t\|^2} := \frac{\int_0^t \eta(s) \|\mathbf{m}_s\|^2 ds}{\int_0^t \eta(s) ds}$, and $f_{\min} := \min_{\mathbf{x} \in \mathbb{R}^N} f(\mathbf{x})$. Moreover, we also have

$$\begin{aligned} \mathbb{E} \left[\overline{\|\nabla f(\mathbf{X}_t)\|^2} \right] &\leq \frac{2\sqrt{V+\epsilon} \left(f(\mathbf{X}_0) - \frac{1}{c_1} \left\langle \nabla f(\mathbf{X}_0), \frac{\mathbf{m}_0}{\sqrt{\mathbf{v}_0+\epsilon}} \right\rangle - f_{\min} + \frac{\ell M \sqrt{N}}{c_1 \sqrt{\epsilon}} \right)}{\int_0^t \eta(s) ds} \\ &\quad + \left(\frac{2L\sqrt{V+\epsilon}}{c_1 \epsilon} + \left(1 + \frac{\bar{\sigma}^2}{\epsilon^2} \right) \frac{c_2^2 (V+\epsilon)}{2c_1^2 \epsilon} \right) \mathbb{E} \left[\overline{\|\mathbf{m}_t\|^2} \right]. \end{aligned} \quad (13)$$

Theorem 2 outlines the convergence rates of the momentum \mathbf{m}_t and gradient $\nabla f(\mathbf{X}_t)$ in (Adam-SDE). When focusing solely on the LR schedule $\eta(t)$, and ignoring N and other Lipschitz constants, the bound for $\mathbb{E} \left[\overline{\|\mathbf{m}_t\|^2} \right]$ simplifies to $\mathcal{O} \left(\frac{1}{\int_0^t \eta(s) ds} + \frac{\int_0^t \eta(s)^2 ds}{\int_0^t \eta(s) ds} \right)$. By Eqn. (13), the bound for $\mathbb{E} \left[\overline{\|\nabla f(\mathbf{X}_t)\|^2} \right]$ is identical, indicating that $\mathbb{E} \left[\overline{\|\nabla f(\mathbf{X}_t)\|^2} \right]$ and $\mathbb{E} \left[\overline{\|\mathbf{m}_t\|^2} \right]$ share the same convergence rate in terms of $\eta(t)$.

Discussion Theorems 1 and 2 collectively demonstrate a common relationship between the optimization hyper-parameters and the gradient norm from an SDE perspective. Both theorems suggest that the average squared norm of the gradient can be upper bounded by $\mathcal{O}(N^\gamma / \int_0^t \eta(s) ds)$, where $\gamma \geq 1$ is a constant. The magnitude of $f(\mathbf{x}_t) - f(\mathbf{x}^*)$ is positively correlated with the gradient norm in smooth cases, where \mathbf{x}^* is a local minimum in the current region. Consequently, the relationship between the training loss and the hyper-parameters $\eta(t)$ can also be expressed as $c(N / \int_0^t \eta(s) ds)^\alpha$.

As in **Opt-Laws**, we introduce the constants c and α to generalize the relationship between convergence rate and training loss. These parameters are essential because $\mathcal{O}(N^\gamma / \int_0^t \eta(s) ds)$ reflects the worst-case convergence rate, while the actual rate depends on the specific architectures of LLMs, data, and training techniques. Therefore, a data-driven approach is used to determine c and α , ensuring these parameters are more practically applicable, as worst-case bounds are often too conservative for LLM training strategies.

6.3 Inspiration from Escaping Capacity

Effective optimization hyper-parameters can expedite escaping sharp local minima during training, which is why large LRs are favored when training LLMs, followed by cooldown techniques. These strategies help LLMs efficiently move away from sharp local minima, improving the final training loss. Building on this idea, this subsection quantitatively investigates the escape capacity of (SGD-SDE) and (Adam-SDE). We calculate the probability of these dynamics escaping a local region, providing a rigorous analysis of their effectiveness.

6.3.1 LINEARIZATION APPROXIMATION OF SDES

In the context of SDEs, the density of the solutions adheres to the Fokker-Planck-Kolmogorov (FPK) equation. For instance, in the case of (SGD-SDE), the specific FPK form is

$$\frac{\partial p(\mathbf{x}, t)}{\partial t} = \sum_{i=1}^N \frac{\partial}{\partial x_i} [\eta(t) \nabla_i f(\mathbf{x}) p(\mathbf{x}, t)] + \frac{\eta_0}{2} \sum_{i,j} \frac{\partial^2}{\partial x_i \partial x_j} [\Sigma(\mathbf{x})_{ij} \eta^2(t) p(\mathbf{x}, t)], \quad (14)$$

where $p(\mathbf{x}, t)$ denotes the density of \mathbf{X}_t at time t , $\Sigma(\mathbf{x})_{ij}$ is the (i, j) -th entry of the covariance matrix $\Sigma(\mathbf{x})$ in Eqn. (10), $\nabla_i f(\mathbf{x})$ is the i -th component of the gradient $\nabla f(\mathbf{x})$, and the initial distribution is specified by the Dirac delta function $\delta(\mathbf{x} - \mathbf{X}_0)$. The non-linearity and time-dependent nature of the FPK equation pose significant challenges for deriving analytical solutions. Consequently, it is difficult to directly estimate the exit times using the density function $p(\mathbf{x}, t)$. A common approach is to approximate the operators in Eqn. (14), to make the estimation of exit times more tractable.

Given the density $p(\mathbf{x}, t)$ at time t , we aim to determine the density $p(\mathbf{x}, t + \Delta_t)$ at time $t + \Delta_t$. Note that the transition density over the interval $[t, t + \Delta_t]$ still satisfies Eqn. (14) with the initial condition $p(\mathbf{x}, t)$. We then perform a local linear approximation of Eqn. (14), for all $s \in [t, t + \Delta_t]$:

$$\begin{aligned} \frac{\partial p(\mathbf{x}, s)}{\partial s} &\approx \sum_{i=1}^N \frac{\partial}{\partial x_i} \{ \eta(s) p(\mathbf{x}, s) \nabla_i f(\bar{\mathbf{x}}_t) + \eta(s) p(\mathbf{x}, s) [\nabla^2 f(\bar{\mathbf{x}}_t) (\mathbf{x} - \bar{\mathbf{x}}_t)]_i \} \\ &+ \frac{\eta_0}{2} \sum_{i,j} \frac{\partial^2}{\partial x_i \partial x_j} [\eta^2(s) p(\mathbf{x}, s) \Sigma(\bar{\mathbf{x}}_t)_{ij}], \end{aligned} \quad (15)$$

where the drift term $\nabla f(\mathbf{x})$ is approximated by its first order expansion around the mean value $\bar{\mathbf{x}}_t := \mathbb{E}[\mathbf{X}_t]$ at time t , while the diffusion term $\Sigma(\mathbf{x})$ is approximated by its value at $\bar{\mathbf{x}}_t$ without expansion. Higher-order terms are neglected. This local linearization implies that the FPK equation now describes a local Ornstein-Uhlenbeck process. Consequently, the solution $p(\mathbf{x}, s)$ becomes a Gaussian distribution $\forall s \in [t, t + \Delta_t]$. By iteratively applying such local approximations and letting $\Delta_t \rightarrow 0$, the dynamics of \mathbf{X}_t evolve into a Gaussian process derived from piecewise linear approximations. The mean $\bar{\mathbf{x}}_t := \mathbb{E}[\mathbf{X}_t]$ and variance $\mathbf{P}_t := \text{Cov}(\mathbf{X}_t)$ of this process are governed by the ODEs as follows:

$$\begin{cases} \frac{d\bar{\mathbf{x}}_t}{dt} = -\eta(t) \nabla f(\bar{\mathbf{x}}_t), \\ \frac{d\mathbf{P}_t}{dt} = -\eta(t) \mathbf{P}_t \nabla^2 f(\bar{\mathbf{x}}_t) - \eta(t) \nabla^2 f(\bar{\mathbf{x}}_t) \mathbf{P}_t + \eta_0 \eta^2(t) \Sigma(\bar{\mathbf{x}}_t). \end{cases} \quad (\text{SDE-GA})$$

Since $\{\mathbf{X}_t\}$ is a Gaussian process, the solutions to the ODEs (**SDE-GA**) for the mean and variance fully determine the form of the density. This allows us to analytically determine $p(\mathbf{x}, t)$, which is pivotal for estimating the escape probability from a local region. These approximations, also known in the literature as Gaussian approximations (GAs) (Solin et al., 2021; Archambeau et al., 2007), are widely utilized in filtering theory (Särkkä and Sarmavuori, 2013; Särkkä et al., 2015). For a comprehensive overview, please refer to Särkkä and Solin (2019), Sec. 9.1.

6.3.2 ESCAPE PROBABILITY FROM LOCAL MINIMA

The GA results for both (**SGD-SDE**) and (**Adam-SDE**) are provided as follows:

Proposition 5 (SGD-SDE Approximation) *Considering any local minimum \mathbf{x}^* of $f(\cdot)$, and setting the initial conditions of (**SGD-SDE**) as $\mathbf{X}_0 = \mathbf{x}^*$ and $\mathbf{P}_0 = \mathbf{0}$, the mean $\bar{\mathbf{x}}_t := \mathbb{E}[\mathbf{X}_t]$ and variance $\mathbf{P}_t := \text{Cov}(\mathbf{X}_t)$ of the (**SDE-GA**) for (**SGD-SDE**) satisfies the following ODE:*

$$\begin{cases} \frac{d\bar{\mathbf{x}}_t}{dt} = \mathbf{0}, \\ \frac{d\mathbf{P}_t}{dt} = -\eta(t)\mathbf{P}_t\mathbf{H} - \eta(t)\mathbf{H}\mathbf{P}_t + \eta_0\eta^2(t)\boldsymbol{\Sigma}, \end{cases} \quad (16)$$

where $\mathbf{H} := \nabla^2 f(\mathbf{x}^*)$, and the definition of $\boldsymbol{\Sigma} := \boldsymbol{\Sigma}(\mathbf{x}^*)$ is provided in Eqn. (10). Furthermore, the solution to Eqn. (16) has the following closed form:

$$\mathbf{P}_t = \mathbf{A}(t) \left(\int_0^t \exp\left(\mathbf{H} \int_0^s \eta(\tau) d\tau\right) \boldsymbol{\Sigma} \exp\left(\mathbf{H} \int_0^s \eta(\tau) d\tau\right) \eta_0 \eta^2(s) ds \right) \mathbf{A}(t), \quad (17)$$

where

$$\mathbf{A}(t) = \exp\left(-\mathbf{H} \int_0^t \eta(s) ds\right).$$

We can reformulate the (**Adam-SDE**) in the similar form of (**SGD-SDE**). Let $\mathbf{Z}_t := [\mathbf{X}_t; \mathbf{m}_t; \mathbf{v}_t]$ and $\widehat{\mathbf{W}}_t$ be the $3N$ -dimensional Brownian motion. Then, (**Adam-SDE**) can be rewritten as

$$d\mathbf{Z}_t = -\eta(t) \underbrace{\begin{bmatrix} \mathbf{m}_t \odot (\mathbf{v}_t + \epsilon)^{-\frac{1}{2}} \\ c_1(\mathbf{m}_t - \nabla f(\mathbf{X}_t)) \\ c_2(\mathbf{v}_t - \text{diag}(\boldsymbol{\Sigma}(\mathbf{X}_t))) \end{bmatrix}}_{=: \mathbf{F}(\mathbf{Z}_t)} dt + c'_1 \eta(t) \begin{bmatrix} \mathbf{0} & & \\ & \sigma(\mathbf{X}_t) & \\ & & \mathbf{0} \end{bmatrix} d\widehat{\mathbf{W}}_t. \quad (18)$$

Subsequently, the Jacobian of $\mathbf{F}(\mathbf{Z})$ with respect to \mathbf{Z} is given by:

$$\partial_{\mathbf{Z}} \mathbf{F}(\mathbf{Z}) = \begin{bmatrix} \mathbf{0} & \text{Diag}(\mathbf{v} + \epsilon)^{-\frac{1}{2}} & -\frac{1}{2} \text{Diag}(\mathbf{m} \odot (\mathbf{v} + \epsilon)^{-\frac{3}{2}}) \\ -c_1 \nabla^2 f(\mathbf{X}) & c_1 \mathbf{I} & \mathbf{0} \\ -c_2 \partial_{\mathbf{X}} \text{diag}(\boldsymbol{\Sigma}(\mathbf{X})) & \mathbf{0} & c_2 \mathbf{I} \end{bmatrix}. \quad (19)$$

Based on the reformulation, we also have a similar GA approximation for (**Adam-SDE**).

Proposition 6 (Adam-SDE Approximation) Denote $\bar{\mathbf{z}}_t := \mathbb{E}[\mathbf{Z}_t]$ and $\hat{\mathbf{P}}_t := \text{Cov}(\mathbf{Z}_t)$. Consider any local minimum \mathbf{x}^* of $f(\cdot)$ and set the initial conditions of (Adam-SDE) as $\mathbf{X}_0 = \mathbf{x}^*$, $\mathbf{m}_0 = \mathbf{0}$, $\mathbf{v}_0 = \text{diag}(\boldsymbol{\Sigma}(\mathbf{x}^*))$ and $\mathbf{P}_0 = \mathbf{0}$. The Gaussian approximation for (Adam-SDE) satisfies

$$\begin{cases} \frac{d\bar{\mathbf{z}}_t}{dt} = \mathbf{0}, \\ \frac{d\hat{\mathbf{P}}_t}{dt} = -\eta(t)\hat{\mathbf{P}}_t\hat{\mathbf{H}}^\top - \eta(t)\hat{\mathbf{H}}\hat{\mathbf{P}}_t + (c'_1)^2\eta(t)^2\hat{\boldsymbol{\Sigma}}, \end{cases} \quad (20)$$

where

$$\hat{\mathbf{H}} := \begin{bmatrix} \mathbf{0} & \text{Diag}(\boldsymbol{\Sigma}(\mathbf{x}^*) + \epsilon\mathbf{I})^{-\frac{1}{2}} & \mathbf{0} \\ -c_1\nabla^2 f(\mathbf{x}^*) & c_1\mathbf{I} & \mathbf{0} \\ -c_2\partial_{\mathbf{X}}\text{diag}(\boldsymbol{\Sigma}(\mathbf{x}^*)) & \mathbf{0} & c_2\mathbf{I} \end{bmatrix}, \quad \text{and} \quad \hat{\boldsymbol{\Sigma}} := \begin{bmatrix} \mathbf{0} & & \\ & \boldsymbol{\Sigma}(\mathbf{x}^*) & \\ & & \mathbf{0} \end{bmatrix}.$$

Furthermore, the solution to Eqn. (20) has the following closed form:

$$\hat{\mathbf{P}}_t = \hat{\mathbf{A}}(t) \left(\int_0^t \exp\left(\hat{\mathbf{H}} \int_0^s \eta(\tau) d\tau\right) \hat{\boldsymbol{\Sigma}} \exp\left(\hat{\mathbf{H}}^\top \int_0^s \eta(\tau) d\tau\right) (c'_1)^2 \eta(s)^2 ds \right) \hat{\mathbf{A}}^\top(t), \quad (21)$$

where

$$\hat{\mathbf{A}}(t) = \exp\left(-\hat{\mathbf{H}} \int_0^t \eta(s) ds\right).$$

Propositions 5 and 6 indicate that, under specified initial conditions, the approximated solutions to both (SGD-SDE) and (Adam-SDE) follow Gaussian distribution with mean \mathbf{x}^* . For ease of notation, we will continue to denote this Gaussian approximated solution as \mathbf{X}_t throughout this paper. By leveraging the anti-concentration inequality (Carbery and Wright, 2001), we can effectively calculate the probability that \mathbf{X}_T remains within the local vicinity of \mathbf{x}^* after a time period T . A smaller probability suggests a greater likelihood of escape from this region, indicating better escape capacity.

Theorem 3 (SGD Escape Probability) With the same initial conditions specified in Propositions 5, the Gaussian approximated solution for (SGD-SDE) satisfies

$$\mathbb{P}[\|\mathbf{X}_t - \mathbf{x}^*\|^2 \geq \epsilon] \geq 1 - \sqrt{\frac{e\epsilon}{\text{Tr}(\mathbf{P}_t)}},$$

where \mathbf{P}_t is the covariance matrix of \mathbf{X}_t defined in Eqn. (17). Suppose Assumption 2 holds, and considering the learning rate conditions $\eta(0) = \eta_{\max}$ and $\eta(T) = 0$, then we have

$$\mathbb{P}[\|\mathbf{X}_T - \mathbf{x}^*\|^2 \leq \epsilon] = \mathcal{O}\left(\left(\frac{\epsilon}{\eta_{\max}^4 \text{Tr}(\boldsymbol{\Sigma}_g)} \int_0^T \eta'(s)^2 ds\right)^{1/2}\right).$$

Theorem 4 (Adam Escape Probability) With the same initial conditions specified in Propositions 6, the Gaussian approximated solution for (Adam-SDE) satisfies

$$\mathbb{P}[\|\mathbf{X}_t - \mathbf{x}^*\|^2 \geq \epsilon] \geq 1 - \sqrt{\frac{e\epsilon}{\text{Tr}(\hat{\mathbf{P}}_t)}},$$

where $\widehat{\mathbf{P}}_t$ is the covariance matrix of \mathbf{Z}_t defined in Eqn. (21). Suppose Assumption 2 holds, and considering the learning rate conditions $\eta(0) = \eta_{\max}$ and $\eta(T) = 0$, then we have

$$\mathbb{P}[\|\mathbf{X}_T - \mathbf{x}^*\|^2 \leq \varepsilon] = \mathcal{O}\left(\left(\frac{\varepsilon}{\eta_{\max}^4 \text{Tr}(\boldsymbol{\Sigma}_g)} \int_0^T \eta'(s)^2 ds\right)^{1/2}\right).$$

Theorems 3 and 4 provide lower bounds on the probability that \mathbf{X}_t is located outside an ε -radius ball centered in \mathbf{x}^* after time t . A larger lower bound indicates a stronger escaping capacity of \mathbf{X}_t . Equivalently, a smaller probability that \mathbf{X}_T remains within the local region of \mathbf{x}^* after the LR has cooled down (at time T) suggests a greater capacity of \mathbf{X}_T to escape suboptimal local minima.

Based on the unified upper bounds provided by Theorems 3 and 4, we propose incorporating $\mathcal{O}((\int \eta'(s)^2 ds)^\alpha)$ into Opt-Laws. Together with the convergence analysis, this yields two complementary perspectives on how the LR schedule affects the final training loss. The convergence terms capture optimization progress toward stationarity, while the escape terms characterize the schedule’s influence on basin selection. These two aspects jointly motivate the feature construction in Opt-Laws.

On the escape analysis in practice. During the high-learning-rate phase, stochastic noise prevents the iterate from settling at any local minimum. However, as the LR decays to zero the noise vanishes and the iterate converges to a basin. The escape analysis (Theorems 3 and 4) characterizes which basin the iterate ultimately falls into. A more gradual cooldown sustains noise-driven diffusion longer, allowing migration toward better basins before the iterate is frozen, while an abrupt cooldown locks the iterate into its current region. The quantity $\int \eta'(s)^2 ds$ summarizes this effect from the covariance dynamics, measuring the abruptness of the cooldown and hence the degree to which the schedule constrains basin selection. Progressive ablation (Appendix Sec. A.4) confirms that escape features carry independent predictive signal, improving Top-2 from 66% to 89% on top of convergence-only features.

On the β - η coupling in Adam-SDE. The coupling between $\beta_{1,k}, \beta_{2,k}$ and η_k is a mathematical necessity for a non-degenerate SDE: with fixed β , the momentum relaxes infinitely fast relative to the parameter updates as $\eta \rightarrow 0$, reducing the SDE to a deterministic normalized gradient flow in which the stochastic dynamics and the rich schedule-dependent structure (such as the escape-related terms) are lost (Malladi et al., 2022). The single-time-scale coupling ensures that momentum and parameter dynamics evolve on the same effective time scale. Regardless of whether β is fixed (discrete analysis) or coupled with η (SDE analysis), β affects only the constants in the convergence bound, not the functional dependence on the schedule: discrete fixed- β analyses (Xie et al., 2024b; Zhang et al., 2022; Chen et al., 2019) yield bounds controlled by $\sum_k \eta_k$, confirming that the convergence feature form $1/\int_0^t \eta(s) ds$ is preserved. The SDE framework additionally provides escape-related insights involving $\int_0^T \eta'(s)^2 ds$ that are inaccessible from discrete analysis alone. Since our feature construction only extracts these functional forms and fits all coefficients from data, this is sufficient for our purpose. Bridging the gap between the discrete fixed- β framework and the continuous coupled- β SDE framework is an open problem beyond the scope of this work.

7 Conclusion

We introduced Opt-Laws, a framework that predicts the final training loss of LLMs as a function of the learning-rate schedule, model size, and data size.

The framework decomposes the schedule’s effect into two SDE-motivated mechanisms. The convergence features, derived from the integrated learning rate $\int \eta$, capture how fast the optimizer approaches stationarity. The escape features, derived from $\int \eta_t'^2$, capture the schedule’s influence on which basin the optimizer ultimately settles into. This decomposition yields 15 interpretable features whose coefficients are fitted from small-scale experiments, bridging theoretical analysis and data-driven prediction.

On the held-out benchmark, the generalized Opt-Laws achieves Top-2 hit rate of 94% and Spearman correlation of 0.84, outperforming all five baselines. The divergence criterion attains F1=0.92. In extrapolation settings, the law correctly identifies the best schedule family in all five out-of-family groups, and the history-aware extension produces correct rankings across continual-training and fine-tuning pipelines.

The current empirical validation covers MoE models with up to 4B trainable parameters and piecewise-linear, cosine, and constant-plus-linear schedules. The SDE-based feature construction does not assume a particular architecture or schedule family, and extending the validation to broader settings is a natural next step. A discussion of scope and limitations is provided in Appendix C.

Appendix A. Experimental Setup and Supplementary Results

This appendix provides supplementary details for the experiments in the main text. We first summarize the shared model and training settings (Sec. A.1), then define the small-scale training grid and evaluation protocol used for held-out benchmarking (Sec. A.2). Next, we document the exponent selection procedure and post-selection fitted coefficients (Sec. A.3). We then present the feature ablation and sensitivity analysis (Sec. A.4), followed by the divergence prediction benchmark (Sec. A.5) and schedule-family generalization results (Sec. A.6).

The theory supplement appears in Appendix. B, and a discussion of scope and limitations in Appendix. C.

A.1 Model Configurations and Shared Training Settings

Table 6 summarizes the key parameters of the MoE model employed in our experiments. These include architectural parameters such as the number of layers, hidden size, and the number of attention heads, along with parameter sizes: total trainable parameters, activated parameters during the forward pass, and the total parameters for the eight experts. Additionally, common training parameters are listed, including token length, global batch size, optimizer (AdamW (Loshchilov and Hutter, 2017)), weight decay, minimal learning rate, and gradient clipping threshold. These parameters adhere to standard LLM training practices without any special adjustments. We set the minimal learning rate to 0.0 to maximize comparability across schedules and to avoid an artificial performance floor from a non-zero residual learning rate.

Table 6: Key parameters of the MoE models used in experiments. *Top*: architecture parameters (per model size). *Bottom*: training settings shared across all models.

Model Size	Architecture			Parameters		
	Layers	Hidden	Attn. Heads	Total	Activated	Expert
8×0.001B	4	128	4	0.023B	0.019B	0.0063B
8×0.02B	12	384	12	0.17B	0.093B	0.113B
8×0.1B	12	768	12	0.58B	0.27B	0.45B
8×0.3B	24	1024	16	1.90B	0.75B	1.66B
8×0.6B	24	1536	16	4.05B	1.56B	3.62B

Shared training settings (all models):
Token length: 2048 Batch size: 2048 Optimizer: AdamW
Weight decay: 0.1 Min. LR: 0.0 Grad. clip: 1.0

Table 7: Data inventory for the small-scale training grid. Each row is a (model size, token budget) block with 35–40 hyper-parameter configurations. Divergent runs are those whose final loss exceeds 6.

Model Size	Tokens	Total	Convergent	Divergent
8×0.001B	10B	35	35	0
8×0.001B	30B	40	40	0
8×0.02B	10B	35	33	2
8×0.02B	30B	40	38	2
8×0.1B	10B	35	29	6
8×0.1B	30B	40	33	7
8×0.3B	20B	35	26	9
Total		260	234	26

A.2 Fitting Setup and Evaluation Protocol

This subsection defines the training grid and evaluation protocol used for the held-out benchmarks in the main text.

Training grid. The training grid corresponds to the loss grids in Fig. 2. We train MoE models at four model sizes (8×0.001B, 8×0.02B, 8×0.1B, 8×0.3B) on 10B, 20B, or 30B tokens, yielding seven (model size, token budget) blocks listed in Table 7. Within each block, we vary peak LR from 10^{-3} to 1.5×10^{-2} and warmup steps from 128 to 6000, producing 35 or 40 configurations per block and 260 configurations in total. All runs use a linear warmup followed by linear cooldown schedule. A run is labeled divergent if its final loss exceeds 6 (the typical plateau for failed runs), yielding 234 convergent and 26 divergent configurations. The convergent configurations are used for regression evaluation, and all 260 for divergence prediction.

Cross-validation protocol. We evaluate via 5-fold cross-validation at the configuration level. Within each (model size, token budget) block, the hyper-parameter configurations are randomly partitioned into five folds, so that every fold contains held-out samples from all blocks. In each round, the training portions from all blocks are combined to fit a single exponent vector α and coefficient vector \mathbf{c} across the full grid, following the staged procedure in Sec. A.3. The held-out configurations are used only for evaluation. Metrics are computed on the held-out configurations of each round and averaged across all five rounds. Divergent runs are excluded from the regression but retained for the divergence classification task in Sec. A.5. Runs with the constant-plus-linear cooldown schedule are excluded from fitting and reserved for the schedule-family generalization evaluation in Sec. A.6.

Task separation. The training grid supports three evaluation tasks. (1) Regression with the simplified Opt-Laws (Sec. 3), which uses a single (model size, token budget) block. (2) Regression with the generalized Opt-Laws (Sec. 4.2), which uses all convergent configurations across blocks. (3) Divergence prediction (Sec. A.5), which uses all 260 configurations including divergent runs. The three tasks share the same underlying grid but are evaluated independently.

A.2.1 METRIC DEFINITIONS

We report the following five metrics in Table 1. The first two assess regression quality and the remaining three assess schedule-selection quality.

- **R^2 .** Computed over all held-out convergent configurations across all blocks and folds: $R^2 = 1 - \sum_i (y_i - \hat{y}_i)^2 / \sum_i (y_i - \bar{y})^2$, where $y_i = \log(\text{Loss}_i)$, \hat{y}_i is the predicted log-loss, and \bar{y} is the mean of y_i over the held-out set.
- **Relative Error (%)**. The mean absolute relative error over held-out convergent configurations: $\frac{1}{n} \sum_i |(\text{Loss}_i - \widehat{\text{Loss}}_i) / \text{Loss}_i| \times 100\%$, where Loss_i is the actual loss and $\widehat{\text{Loss}}_i$ is the predicted loss.
- **Spearman**. For each (model size, token budget) block in each fold, we rank the held-out configurations by predicted loss and by actual loss, and compute the Spearman rank correlation between the two rankings. The reported value is the average across all blocks and folds.
- **Top- k Hit Rate**. For each block in each fold, we select the held-out configuration with the lowest predicted loss. If this configuration is among the k held-out configurations with the lowest actual loss, the block counts as a hit. This simulates the practical scenario of ranking unseen candidate schedules. Top- k Hit Rate is the number of hits divided by the total number of (block, fold) pairs evaluated. We report $k = 2$ throughout.
- **Regret**. For each block in each fold, let s^* be the held-out configuration with the lowest actual loss and \hat{s}^* be the one with the lowest predicted loss. The regret is $\text{Loss}(\hat{s}^*) - \text{Loss}(s^*)$, measuring the excess loss incurred by following the prediction. The reported value is the mean regret across all block-fold evaluations.

A.3 Exponent Selection and Fitted Coefficients

The exponent vector α in **Opt-Laws** is not optimized jointly with the linear coefficients \mathbf{c} . The three SDE-derived terms ($1/\int \eta_w$, $1/\int \eta_c$, $\int \eta_t^2$) use exponent ± 1.0 fixed by theory. For the remaining terms, each exponent is selected from the discrete candidate set

$$\{0.15, 0.20, 0.25, 0.50, 1.0\}.$$

The selection follows a two-level procedure. In the first level, we assign a shared exponent to each of the four groups (mixed interactions, convergence cross-terms, escape powers, scale powers) and search over all group-level combinations ($5^4 = 625$), with \mathbf{c} refitted via linear regression for each candidate, minimizing the fitting loss on the training folds. In the second level, we fix the group-level values and adjust only the most sensitive term within each group from the same candidate set. The held-out fold is used only for final evaluation. The final exponent vector and coefficients are reported in Table 8.

A.3.1 FITTED COEFFICIENTS

Table 8 reports the selected exponent vector and fitted coefficient vector for the generalized **Opt-Laws**. Unlike the simplified Opt-Laws in Eqn. (1), the coefficient vector \mathbf{c} is not constrained to be strictly positive. The simplified law has a small number of terms with direct physical interpretations, where positive coefficients are natural. The generalized law, however, contains 15 features including interaction terms, many of which are correlated. In multivariate regression with correlated features, individual coefficients reflect partial effects conditional on all other features. For example, two features that are each positively correlated with loss may receive opposite signs because one already accounts for part of the other’s contribution. Their signs therefore cannot be inferred from marginal correlations alone. We do not impose positivity constraints on \mathbf{c} .

Normalization. Before estimating the model loss using the parameters from these tables, it is necessary to normalize the training iteration steps S , model size N , and LR. For model parameter count N , we use the total number of learnable parameters, expressed in billions. The iteration count S and all step-related variables (warmup steps, cooldown steps) are converted to token counts in billions: $S_{\text{tokens}} = S \times L \times B/10^9$, where $L = 2048$ is the token length and $B = 2048$ is the global batch size (Table 6). The LR is normalized by dividing it by 1.5×10^{-2} , ensuring that the normalized LR values fall within the range of 0 to 1 across all experiments.

Table 8 provides the coefficients and powers for the convergence, escape, mixed, and bias terms for two LR schedules: (1) a linear warmup over a steps followed by a linear cooldown over $S - a$ steps, and (2) a linear warmup over a_1 steps, followed by a constant LR (η_{\max}) from a_1 to a_2 steps, and a cooldown over $S - a_2$ steps (as illustrated in Fig. 6 (a)).

A.3.2 DIVERGENCE CRITERION COEFFICIENTS

The parameters in $R(\eta_{\max}, a_1, N, S)$ (Eqn. (4)) are fitted on the train split of the small-scale training grid, where each configuration is labeled convergent or divergent based on whether the final loss exceeds 6. Before applying R , the variables S , a_1 , N , and η_{\max} are normalized following the same procedure as for the regression (Sec. A.3.1). We found that squaring the

Table 8: Selected exponents α , fitted coefficients c , and closed-form feature expressions for the generalized **Opt-Laws**. Two schedule families are listed. **S1**: linear warmup (a steps) followed by linear cooldown ($S-a$ steps). **S2**: linear warmup (a_1 steps), constant phase at η_{\max} (a_1 to a_2), then linear cooldown ($S-a_2$ steps). \mathcal{E} denotes $\int_{a_{e2}}^S \eta_t'^2$ in the mixed terms.

ϕ	α	c	S1	S2	ϕ	α	c	S1	S2
Convergence Terms					Mixed Terms ($\mathcal{E} = \int_{a_{e2}}^S \eta_t'^2$)				
$\int_0^{a_{c1}} \eta_t$	-1.0	-6.92×10^{-4}	$\frac{ah}{2}$	$\frac{a_1h}{2}$	$\mathcal{E} / \int_0^{a_{c1}} \eta_t$	0.20	-4.68×10^{-2}	$\frac{2h}{a(S-a)}$	$\frac{2h}{a_1(S-a_2)}$
$\int_{a_{c2}}^S \eta_t$	-1.0	-1.27×10^{-3}	$\frac{(S-a)h}{2}$	$\frac{(S+a_2-2a_1)h}{2}$	$\mathcal{E} / \int_{a_{c2}}^S \eta_t$	0.15	-4.18×10^{-2}	$\frac{2h}{(S-a)^2}$	$\frac{2h}{(S-a_2)(S+a_2-2a_1)}$
$N / \int_{a_{c2}}^S \eta_t$	0.25	-4.68×10^{-2}	$\frac{2N}{(S-a)h}$	$\frac{2N}{(S+a_2-2a_1)h}$	$N \cdot \mathcal{E} / \int_0^{a_{c1}} \eta_t$	0.15	-1.19×10^{-1}	$\frac{2Nh}{a(S-a)}$	$\frac{2Nh}{a_1(S-a_2)}$
$\int_0^{a_{c1}} \eta_t \cdot \int_{a_{c2}}^S \eta_t$	-0.23	4.65×10^{-2}	$\frac{a(S-a)h^2}{4}$	$\frac{a_1(S+a_2-2a_1)h^2}{4}$	$N \cdot \mathcal{E} / \int_{a_{c2}}^S \eta_t$	0.15	2.18×10^{-1}	$\frac{2Nh}{(S-a)^2}$	$\frac{2Nh}{(S-a_2)(S+a_2-2a_1)}$
Escape Terms					Bias Terms (global scalar)				
$\int_{a_{e2}}^S \eta_t'^2$	1.0	9.62×10^{-3}	$\frac{h^2}{S-a}$	$\frac{h^2}{S-a_2}$	N (model size)	-0.25	3.1×10^{-1}	N	N
$\int_0^{a_{e1}} \eta_t'^2$	0.25	1.92×10^{-2}	$\frac{h^2}{a}$	$\frac{h^2}{a_1}$	S (steps)	-0.25	6.98×10^{-1}	S	S
$\int_{a_{e2}}^S \eta_t'^2$	0.25	-5.05×10^{-2}	$\frac{h^2}{S-a}$	$\frac{h^2}{S-a_2}$	η_{\max}	0.20	5.26×10^{-2}	h	h
SN	-0.25	-1.82×10^{-1}	SN	SN	1	1.0	3.14×10^{-1}	1	1

normalized values of S and a_1 before substitution into Eqn. (4) improves the fitting stability. The fitted parameters are $\hat{c}_1 = 1.76$, $\hat{c}_2 = 33.21$, $\hat{c}_3 = 292.03$, $\hat{\alpha}_1 = 0.218$, and $\hat{\alpha}_2 = 0.5$.

A.4 Feature Ablation and Sensitivity Analysis

This subsection examines three aspects of the feature design: whether each of the four feature blocks (scale, convergence, escape, mixed) carries independent predictive signal, whether the selected exponent values are robust to perturbation, and whether including the decay phase $[a_1, a_2]$ in the convergence integral improves prediction. All experiments use the same 5-fold cross-validation protocol as in Sec. A.2.

Feature-family ablation. Table 9 reports a progressive ablation in which feature blocks are added one at a time. Scale terms alone already capture moderate within-block ranking (Top-2 51%) because the η_{\max} feature carries direct schedule information. Adding the four convergence terms raises Top-2 to 66% and halves the regret from 0.027 to 0.016, confirming that the cumulative optimization budget provides selection value beyond what η_{\max} alone supplies. Escape-related terms contribute the single largest improvement (Top-2 from 66% to 89%, Spearman from 0.61 to 0.77), consistent with the SDE escape analysis: the derivative-driven fluctuation terms carry independent predictive signal. Adding mixed interaction terms brings the full model to Top-2 94% and Spearman 0.84, capturing cross-scale modulation that single-block features cannot represent.

Table 9: Feature-family ablation (5-fold CV, held-out). Features are added by theoretical block: scale, convergence, escape, mixed interactions. The final regression model contains 15 non-bias features plus one intercept term (16 fitted coefficients in total).

Feature variant	Fit Quality		Selection		Regret
	R^2	Rel.Err.(%)	Spearman	Top-2 (%)	
Scale only (3d)	0.992	1.06	0.60	51	0.027
+ Convergence (7d)	0.992	1.06	0.61	66	0.016
+ Escape (11d)	0.997	0.61	0.77	89	0.006
+ Mixed interactions (15d)	0.998	0.50	0.84	94	0.003

Decay-phase ablation. As described in Sec. 4.3, the convergence integral excludes the decay phase $[a_1, a_2]$, whose LR-transition information is captured by the escape feature $\int_0^{a_2} \eta_t^2$. Table 10 tests the alternative of including the decay in the convergence integral ($a_{c_2} = a_1$ instead of $a_{c_2} = a_2$) on the polygon pre-training configurations in Table 2 and the continual-training configurations in Table 4 that have a non-trivial decay phase ($a_1 < a_2$). For pre-training, including the decay slightly increases the mean prediction error (0.15% to 0.23%), though both are well below 0.5%. For continual training under strong distribution shift, both treatments produce identical rankings (Spearman 1.00). Under weak distribution shift the Spearman drops from 0.90 to 0.30, but this setting has actual losses within a 0.005 range (1.991–1.996), so the ranking task itself is near the resolution limit. Overall, the two treatments produce similar prediction quality, with the default ($a_{c_2} = a_2$) performing slightly better. This is consistent with the observation in Sec. 4.3 that the decay-phase information is already captured by the escape feature, so including it in the convergence integral provides little additional benefit.

Exponent sensitivity. Table 11 perturbs one exponent group at a time while keeping all others at their defaults and refitting \mathbf{c} on the training split. For the three schedule-dependent groups (mixed interactions, convergence cross-terms, and escape powers), perturbing α within the candidate range leaves Top-2 at 94% and $R^2 \geq 0.998$. This robustness indicates that the SDE-derived functional forms already impose sufficient structural constraint, and the exact exponent values play a refinement role rather than a defining one. The scale-power group is the only sensitive component: at $\alpha=0.50$, Top-2 drops from 94% to 80%. Unlike the schedule-dependent terms, scale terms have no underlying SDE structure and rely entirely on the exponent to capture how model size modulates the prediction across a wide range ($8 \times 0.001\text{B}$ to $8 \times 0.3\text{B}$). Together with the feature-family ablation above, these results suggest that the primary predictive signal comes from the feature structure itself, not from the specific exponent values.

A.5 Divergence Prediction Benchmark

This subsection evaluates the R criterion (Eqn. (4)) as a standalone divergence classifier. The training grid contains 260 configurations (234 convergent, 26 divergent), evaluated under the same 5-fold cross-validation protocol as the loss regression. Because of the class imbalance,

Table 10: Decay-phase ablation on multi-phase schedules ($a_1 < a_2$). $a_{c_2} = a_2$ (default) starts the convergence tail at a_2 , excluding the decay $[a_1, a_2]$. $a_{c_2} = a_1$ includes it. Left: prediction error (%) on polygon pre-training configs (Table 2). Right: predicted scores and ranking for continual training (Table 4), with ranks in parentheses.

Schedule	Actual	Pred. Error (%)		Schedule	Actual	Pred. Score (Rank)	
		$=a_2$	$=a_1$			$=a_2$	$=a_1$
Polygon2	2.098	0.13	0.18	<i>Strong distribution shift</i>			
$a_2=7k, a_3=13k$				Polygon1	1.826	2.058 (3)	2.023 (3)
Polygon1v2	2.097	0.08	0.13	Polygon2	1.821	2.014 (2)	1.983 (2)
$a_2=5k, a_3=11.5k$				Linear	1.818	1.975 (1)	1.974 (1)
Polygon1	2.057	0.35	0.51	<i>Spearman</i>		1.00	1.00
$a_2=10k, a_3=15k$				<i>Weak distribution shift</i>			
Loss-eq	2.079	0.05	0.09	Const+Lin	1.991	1.995 (2)	1.995 (4)
$a_2=7k, a_3=12k$				Linear	1.992	1.975 (1)	1.975 (1)
Mean		0.15	0.23	Polygon1v2	1.993	2.010 (3)	1.991 (3)
Max		0.35	0.51	Polygon2	1.995	2.017 (4)	1.987 (2)
				Polygon1	1.996	2.059 (5)	2.024 (5)
				<i>Spearman</i>		0.90	0.30

we report precision, recall, F1, and balanced accuracy rather than overall accuracy. Three baselines are included: a majority-class predictor (all convergent), a peak- η_{\max} threshold, and logistic regression on $(\eta_{\max}, \text{warmup}, N, S)$.

Table 12 shows that the R criterion achieves $F1 = 0.92$ and balanced accuracy 0.94, well above all three baselines. Divergence in the training grid is not determined by η_{\max} alone: the same peak LR can produce convergence or divergence depending on the warmup duration and model/data scale. A simple threshold on η_{\max} misses this interaction ($F1 = 0.38$), and logistic regression has too few positive examples to learn the nonlinear boundary from raw features ($F1 = 0.54$). The R criterion encodes the interaction through its parameterized form (Eqn. (4)), which is why it achieves high precision (0.96) with relatively few false alarms. The lower recall (0.88) reflects a few borderline configurations where a long warmup nearly offsets a high peak LR, placing them close to the convergence/divergence boundary.

A.6 Schedule-Family Generalization

The generalized Opt-Laws is fitted on piecewise-linear schedules. To test cross-family generalization, we evaluate it on cosine and constant-plus-linear cooldown schedules that are not included in the fitting data. The convergence and escape integrals ($\int \eta$ and $\int \eta_t'^2$) have exact closed-form expressions for all three schedule families, so the feature computation does not introduce any approximation. We compare the three cooldown shapes on five (model, token) groups spanning $8 \times 0.1B$ and $8 \times 0.6B$, where each group shares the same η_{\max} , a_1 , and S .

Table 11: Exponent sensitivity (5-fold CV). One exponent group is set to the stated value while the rest remain at their defaults. The linear coefficients \mathbf{c} are refitted for each setting.

Perturbed group	α value	R^2	Spearman	Top-2 (%)
Default (selected)	–	0.998	0.84	94
Mixed interactions	0.10	0.998	0.83	94
	0.20	0.998	0.84	94
	0.30	0.998	0.85	94
Conv. cross-terms	0.15	0.998	0.84	94
	0.30	0.998	0.84	94
	0.50	0.998	0.82	94
Escape powers	0.15	0.998	0.85	94
	0.50	0.998	0.84	94
Scale powers	0.15	0.997	0.79	94
	0.50	0.996	0.76	80

Table 12: Divergence prediction benchmark (5-fold CV, 234 convergent vs. 26 divergent configurations). The R criterion is compared against three baselines. Precision, recall, F1, and balanced accuracy are reported to account for class imbalance.

Method	Precision	Recall	F1	Bal. Accuracy
Majority class (all conv.)	0.00	0.00	0.00	0.50
Peak- η_{\max} threshold	0.29	0.58	0.38	0.71
Logistic regression (LOO)	0.73	0.42	0.54	0.70
R criterion (5-fold)	0.96	0.88	0.92	0.94

In all five groups, the fitted law correctly identifies the best schedule family, with prediction errors below 2% (Table 13). For the $8 \times 0.1\text{B}$ model at 3B and 10B tokens, most errors are below 1%, comparable to the in-family results in Table 2. This cross-family accuracy is consistent with the continual-training and fine-tuning evaluations (Tables 4 and 5), where polygon, constant-plus-linear, and two-phase schedules outside the fitting family are also correctly ranked. The theoretical basis for this generalization is that the SDE convergence and escape bounds (Theorems 1–4) depend on the schedule only through $\int \eta$ and $\int \eta_t'^2$. These two integrals summarize the schedule’s contribution to optimization progress and basin selection regardless of its parametric form, and all tested schedule families admit exact closed-form expressions for both quantities. The fitted law therefore transfers across families without re-fitting.

Table 13: Schedule-family generalization. The generalized Opt-Laws, fitted only on piecewise-linear schedules, is evaluated on cosine and constant-plus-linear (Const+Lin) cooldown shapes. Within each group the three schedules share the same η_{\max} , a_1 , and S , differing only in cooldown shape. **Bold** marks the actual-best schedule, correctly identified in all five groups. All errors are below 2%.

Model Tokens	Cooldown	Act.	Pred.	Err.(%)	Model Tokens	Cooldown	Act.	Pred.	Err.(%)
8×0.1B 3B	Linear	3.177	3.179	0.1	8×0.6B 10B	Linear	2.501	2.526	1.0
	Cosine	3.205	3.175	0.9		Cosine	2.519	2.524	0.2
	Const+Lin	3.084	3.100	0.5		Const+Lin	2.480	2.484	0.2
8×0.1B 10B	Linear	2.689	2.693	0.1	8×0.6B 3B	Linear	2.995	2.988	0.2
	Cosine	2.695	2.689	0.2		Cosine	3.037	2.986	1.7
	Const+Lin	2.667	2.653	0.5		Const+Lin	2.956	2.908	1.6
8×0.1B 100B	Linear	2.369	2.332	1.5					
	Cosine	2.374	2.329	1.9					
	Const+Lin	2.358	2.312	1.9					

Appendix B. Theory Supplement

This section collects the proofs and derivations underlying the theoretical results stated in the main text.

B.1 Analysis for Opt-Laws, SGD-SDE, and Adam-SDE

B.1.1 PROOF OF PROPOSITION 1

Proof Based on the proposed Opt-Laws, the analytical expressions for the two LR schedules, $\eta_{\cos}(t)$ and $\eta_{\text{const}}(t)$, can be derived as follows:

$$\begin{aligned} \text{Opt-Laws}(\eta_{\cos}) &= c_1 \left(\frac{2}{\eta_{\max} a} \right)^{\alpha_1} + c_2 \left(\frac{2}{\eta_{\max}(S-a)} \right)^{\alpha_2} + \frac{c_3}{S} + b \\ &\quad + c_4 \left(\frac{\pi^2 \eta_{\max}^2}{8(S-a)} \right)^{\alpha_3} + c_5 \left(\frac{\eta_{\max}^2}{a} \right)^{\alpha_4}. \\ \text{Opt-Laws}(\eta_{\text{const}}) &= c_1 \left(\frac{2}{\eta_{\max} a} \right)^{\alpha_1} + c_2 \left(\eta_{\max}(a_c - a) + \frac{\eta_{\max}(S - a_c)}{2} \right)^{-\alpha_2} \\ &\quad + \frac{c_3}{S} + b + c_3 \left(\frac{\eta_{\max}^2}{S - a_c} \right)^{\alpha_3} + c_5 \left(\frac{\eta_{\max}^2}{a} \right)^{\alpha_4}. \end{aligned}$$

Note that $\lim_{S \rightarrow \infty} \text{Opt-Laws}(\eta_{\cos}(\cdot)) = \lim_{S \rightarrow \infty} \text{Opt-Laws}(\eta_{\text{const}}(\cdot)) = b$. Therefore, we have $\lim_{S \rightarrow \infty} |\text{Opt-Laws}(\eta_{\cos}(\cdot)) - \text{Opt-Laws}(\eta_{\text{const}}(\cdot))| = 0$. \blacksquare

B.1.2 DERIVATIONS FOR SGD-SDE AND ADAM-SDE

In this subsection, we derive the SDEs to model the iterative SGD and Adam sequences.

SGD-SDE: The iterative sequence of SGD is given by

$$\mathbf{x}_{k+1} = \mathbf{x}_k - \eta_0 \eta_k (\nabla f(\mathbf{x}_k) + \mathbf{z}_k), \quad \mathbf{z}_k \sim \mathcal{N}(0, \Sigma(\mathbf{x}_k)), \quad (22)$$

where η_k is the normalized learning rate, η_0 is a small rescaling parameter, and ξ_k is a Gaussian noise. Applying the Euler-Maruyama method (for a detailed description, see (Särkkä and Solin, 2019, Chapter 8.2)) to the corresponding SDE (SGD-SDE), we obtain:

$$\mathbf{x}_{k+1} = \mathbf{x}_k - \eta(t_k) \nabla f(\mathbf{x}_k) \Delta t_{k+1} + \sqrt{\eta_0} \eta(t_k) (\Delta t_{k+1} \Sigma(\mathbf{x}_k))^{\frac{1}{2}} \Delta \mathbf{W}_k,$$

where $\Delta t_{k+1} = t_{k+1} - t_k$ and $\Delta \mathbf{W}_k \sim \mathcal{N}(0, \mathbf{I}_N)$. By setting $\Delta t_{k+1} \equiv \eta_0$, the discrete scheme exactly recovers the SGD sequence (22). With the same initial conditions, where $\mathbf{x}_0 = \mathbf{X}_0$, and under certain smooth regularity conditions on the functions involved, it can be established that a positive constant $\alpha > 0$ (referred to as the order) exists satisfying the following property. For any time horizon $T > 0$ and positive integer $m \leq \lfloor \frac{T}{\eta_0} \rfloor$, there exists a constant K and a sufficiently small η_0 such that the following strong error bound holds

$$\mathbb{E} [\|\mathbf{X}_{m\eta_0} - \mathbf{x}_m\|] \leq K \eta_0^\alpha.$$

The classical approximation order for the Euler-Maruyama method is typically $\alpha = \frac{1}{2}$, which was proven in Gihman and Skorohod (1979). We do not delve into the details on this topic, as it is beyond the scope of this work. For a comprehensive discussion on the error analysis of numerical approximations for SDEs, interested readers may consult Kloeden and Platen (1999); Särkkä and Solin (2019). Additionally, for insights into the errors associated with modeling SGD sequences using SDEs, one can refer to the works of Li et al. (2019, 2021b).

Adam-SDE: By applying the Euler-Maruyama method for the SDE associated with \mathbf{m}_t in (Adam-SDE), we obtain:

$$\begin{aligned} \mathbf{m}_{k+1} &= \mathbf{m}_k - c_1 \eta(t_k) (\mathbf{m}_k - \nabla f(\mathbf{x}_k)) \Delta t_{k+1} + c'_1 \eta(t_{k+1}) (\Delta t_{k+1} \Sigma(\mathbf{x}_k))^{\frac{1}{2}} \Delta \mathbf{W}_k \\ &= (1 - c_1 \Delta t_{k+1} \eta_k) \mathbf{m}_k + c_1 \Delta t_{k+1} \eta_k \left(\nabla f(\mathbf{x}_k) + \frac{c'_1}{c_1 \sqrt{\Delta t_{k+1}}} (\Sigma(\mathbf{x}_k))^{\frac{1}{2}} \Delta \mathbf{W}_k \right). \end{aligned}$$

Setting $\Delta t_{k+1} = \frac{\hat{c}_1}{c_1}$ and $c'_1 = c_1 \sqrt{\Delta t_{k+1}} = \sqrt{c_1 \hat{c}_1}$, we derive that

$$\mathbf{m}_{k+1} = (1 - \beta_{1,k}) \mathbf{m}_k + \beta_{1,k} (\nabla f(\mathbf{x}_k) + \mathbf{z}_k),$$

where $\beta_{1,k} = 1 - \hat{c}_1 \eta_k$, $\mathbf{z}_k \sim \mathcal{N}(0, \Sigma(\mathbf{x}_k))$. This recovers the update of $\{\mathbf{m}_k\}$ in (Adam). Furthermore, the update of \mathbf{x}_k corresponds to Euler's method for the ODE associated with \mathbf{X}_t in (Adam-SDE). The update of \mathbf{v}_k aligns with the SDE associated with \mathbf{v}_t in (Adam-SDE), which directly follows from (Malladi et al., 2022, Theorem 4.2 or Theorem 4.5).

B.1.3 PROOF OF PROPOSITION 2

Proof Let $\mathbf{z}_i := \nabla F(\mathbf{x}, \zeta_i) - \nabla f(\mathbf{x})$ and $\mathbf{Z} := [\mathbf{z}_1, \mathbf{z}_2, \dots, \mathbf{z}_D]$, then $\boldsymbol{\Sigma}(\mathbf{x}) = \frac{1}{D} \mathbf{Z} \mathbf{Z}^\top$. Therefore, $\text{Tr}(\boldsymbol{\Sigma}(\mathbf{x})) = \frac{1}{D} \sum_{i=1}^D \text{Tr}(\mathbf{z}_i \mathbf{z}_i^\top) = \frac{1}{D} \sum_{i=1}^D \|\mathbf{z}_i\|^2$. Note that $\mathbf{z}_i \sim N(0, \boldsymbol{\Sigma}_g)$ are i.i.d. Gaussian vectors, where $\boldsymbol{\Sigma}_g$ is an $N \times N$ positive semidefinite covariance matrix. So next, we analyze the concentration of $\frac{1}{D} \sum_{i=1}^D \|\mathbf{z}_i\|^2$. Each $\|\mathbf{z}_i\|^2$ can be represented as a sum of weighted χ^2 variables:

$$\|\mathbf{z}_i\|^2 \sim \sum_{j=1}^n \lambda_j \chi_{ij}^2,$$

where λ_j are the eigenvalues of $\boldsymbol{\Sigma}_g$. The expected value and variance of $\|\mathbf{z}_i\|^2$ are given by:

$$\mathbb{E}[\|\mathbf{z}_i\|^2] = \text{tr}(\boldsymbol{\Sigma}_g), \quad \text{Cov}(\|\mathbf{z}_i\|^2) = 2 \text{Tr}(\boldsymbol{\Sigma}_g^2).$$

Given that χ^2 distribution is sub-exponential, we apply Bernstein's inequality to estimate the concentration of $\frac{1}{D} \sum_{i=1}^D \|\mathbf{z}_i\|^2$, which is given by:

$$\mathbb{P} \left(\left| \frac{1}{D} \sum_{i=1}^D \|\mathbf{z}_i\|^2 - \text{Tr}(\boldsymbol{\Sigma}_g) \right| \geq t \right) \leq 2 \exp \left(- \frac{Dt^2}{4 \text{Tr}(\boldsymbol{\Sigma}_g^2) + 2t \|\boldsymbol{\Sigma}_g\|_{\text{op}}} \right),$$

where $\|\boldsymbol{\Sigma}_g\|_{\text{op}}$ is the operator norm (largest eigenvalue) of $\boldsymbol{\Sigma}_g$. This completes the proof. \blacksquare

B.1.4 PROOF OF PROPOSITION 3

Proof Let $\mathbf{Z}_i := \boldsymbol{\Sigma}_g^{-\frac{1}{2}} (\nabla F(\mathbf{x}, \zeta_i) - \nabla f(\mathbf{x}))$ and $\mathbf{Z} := [\mathbf{Z}_1, \mathbf{Z}_2, \dots, \mathbf{Z}_D]$. Then, $\{\mathbf{Z}_i\}$ are standard Gaussian variables. Let $\hat{\boldsymbol{\Sigma}}(\mathbf{x}) := \frac{1}{D} \mathbf{Z} \mathbf{Z}^\top$. By the eigenvalue variance bounds for covariance matrices in (Ledoux and Rider, 2010, Corollary 3), there exists a constant $C > 0$ such that

$$\begin{aligned} \mathbb{E} \left[\lambda_{\max}(\hat{\boldsymbol{\Sigma}}(\mathbf{x})) \right] &\leq \mathbb{E} \left[\left| \lambda_{\max}(\hat{\boldsymbol{\Sigma}}(\mathbf{x})) - \left(1 + \sqrt{\frac{D}{N}} \right) \right| \right] + \left(1 + \sqrt{\frac{D}{N}} \right) \\ &\leq \sqrt{\mathbb{E} \left[\left(\lambda_{\max}(\hat{\boldsymbol{\Sigma}}(\mathbf{x})) - \left(1 + \sqrt{\frac{D}{N}} \right) \right)^2 \right]} + \left(1 + \sqrt{\frac{D}{N}} \right) \\ &\leq \frac{C}{N^{\frac{2}{3}}} + \left(1 + \sqrt{\frac{D}{N}} \right). \end{aligned}$$

Furthermore, note that $\boldsymbol{\Sigma}(\mathbf{x}) = \boldsymbol{\Sigma}_g^{\frac{1}{2}} \hat{\boldsymbol{\Sigma}}(\mathbf{x}) \boldsymbol{\Sigma}_g^{\frac{1}{2}}$, it follows that:

$$\mathbb{E} [\lambda_{\max}(\boldsymbol{\Sigma}(\mathbf{x}))] \leq \|\boldsymbol{\Sigma}_g\|_{\text{op}} \mathbb{E} \left[\left\| \hat{\boldsymbol{\Sigma}}(\mathbf{x}) \right\|_{\text{op}} \right] = \left(1 + \sqrt{\frac{D}{N}} \right) \sigma_g^2 + \frac{C \sigma_g^2}{N^{\frac{2}{3}}},$$

where $\|\cdot\|_{\text{op}}$ is the operator norm of matrix. This completes the proof. \blacksquare

B.2 Proofs for Convergence Analysis

B.2.1 PROOF OF THEOREM 1

Proof Apply the Itô formula to $f(\mathbf{X}_t)$ and utilize the definition of (SGD-SDE), we obtain:

$$\begin{aligned} df(\mathbf{X}_t) &= \langle \nabla f(\mathbf{X}_t), d\mathbf{X}_t \rangle + \frac{1}{2} \langle \nabla^2 f(\mathbf{X}_t) d\mathbf{X}_t, d\mathbf{X}_t \rangle \\ &= -\eta(t) \|\nabla f(\mathbf{X}_t)\|^2 dt + \eta_0 \eta(t) \langle \nabla f(\mathbf{X}_t), \sigma(\mathbf{X}_t) d\mathbf{W}_t \rangle \\ &\quad + \frac{\eta_0 \eta(t)^2}{2} \langle \nabla^2 f(\mathbf{X}_t), \sigma(\mathbf{X}_t) \sigma(\mathbf{X}_t)^\top \rangle dt. \end{aligned}$$

Taking the integral and then taking the expectation, we have:

$$\begin{aligned} \mathbb{E}[f(\mathbf{X}_t) - f(\mathbf{X}_0)] &= -\mathbb{E} \left[\int_0^t \eta(s) \|\nabla f(\mathbf{X}_s)\|^2 ds \right] \\ &\quad + \mathbb{E} \left[\int_0^t \frac{\eta_0 \eta(s)^2}{2} \langle \nabla^2 f(\mathbf{X}_s), \sigma(\mathbf{X}_s) \sigma(\mathbf{X}_s)^\top \rangle ds \right] \\ &\leq -\mathbb{E} \left[\int_0^t \eta(s) \|\nabla f(\mathbf{X}_s)\|^2 ds \right] + \left(\frac{\eta_0 L N}{2} \int_0^t \eta(s)^2 ds \right) \sup_{\mathbf{x} \in \mathbb{R}^N} \mathbb{E}[\|\Sigma(\mathbf{x}_s)\|_{\text{op}}]. \end{aligned}$$

Rearranging the terms and dividing both sides by $\int_0^t \eta(s) ds$, and by Proposition 3, we have

$$\mathbb{E} \left[\int_0^t \frac{\eta(s)}{\int_0^t \eta(s) ds} \|\nabla f(\mathbf{X}_s)\|^2 ds \right] \leq \frac{f(\mathbf{X}_0) - f_{\min}}{\int_0^t \eta(s) ds} + \frac{\eta_0 L \sigma_0^2 N \int_0^t \eta(s)^2 ds}{2 \int_0^t \eta(s) ds}.$$

This completes the proof. ■

B.2.2 PROOF OF PROPOSITION 4

Proof Denote $\bar{\mathbf{m}}_t := \mathbb{E}[\mathbf{m}_t]$ and $\bar{\mathbf{P}}_t := \text{Cov}(\mathbf{m}_t \mathbf{m}_t^\top)$. Then, $(\bar{\mathbf{m}}_t, \bar{\mathbf{P}}_t)$ satisfies the following ODE:

$$\begin{cases} \frac{d\bar{\mathbf{m}}_t}{dt} = -c_1 \eta(t) \bar{\mathbf{m}}_t + c_1 \eta(t) \nabla f(\mathbf{X}_t) \\ \frac{d\bar{\mathbf{P}}_t}{dt} = -2c_1 \eta(t) \bar{\mathbf{P}}_t + (c'_1)^2 \eta(t)^2 \sigma(\mathbf{X}_t) \sigma(\mathbf{X}_t)^\top. \end{cases}$$

Let $\Sigma_t := \Sigma(\mathbf{X}_t) = \sigma(\mathbf{X}_t) \sigma(\mathbf{X}_t)^\top$. The analytic solution to these equations is given by:

$$\begin{cases} \bar{\mathbf{m}}_t = \exp\left(-c_1 \int_0^t \eta(s) ds\right) \left[\int_0^t \exp\left(c_1 \int_0^s \eta(\tau) d\tau\right) c_1 \eta(s) \nabla f(\mathbf{X}_s) ds \right] \\ \bar{\mathbf{P}}_t = \exp\left(2c_1 \int_0^t \eta(s) ds\right) \left[\int_0^t \exp\left(2c_1 \int_0^s \eta(\tau) d\tau\right) (c'_1)^2 \eta(s)^2 \Sigma(\mathbf{X}_s) ds \right]. \end{cases}$$

Assumption 3.1 implies that $\sup_{\mathbf{x} \in \mathbb{R}^N} \|\nabla f(\mathbf{x})\| \leq \ell$. Therefore, we have that

$$\begin{aligned} \|\bar{\mathbf{m}}_t\| &\leq \ell \exp\left(-c_1 \int_0^t \eta(s) ds\right) \left[\int_0^t \exp\left(c_1 \int_0^s \eta(\tau) d\tau\right) c_1 \eta(s) ds \right], \\ \|\bar{\mathbf{P}}_t\|_{\text{op}} &\leq (c'_1)^2 \bar{\sigma} \exp\left(-2c_1 \int_0^t \eta(s) ds\right) \left[\int_0^t \exp\left(2c_1 \int_0^s \eta(\tau) d\tau\right) \eta(s)^2 ds \right] \\ &\leq (c'_1)^2 \bar{\sigma} \exp\left(-2c_1 \int_0^t \eta(s) ds\right) \left[\int_0^t \exp\left(2c_1 \int_0^s \eta(\tau) d\tau\right) \eta(s)^2 ds \right] \\ &\leq (c'_1)^2 \bar{\sigma} \int_0^t \eta(s)^2 ds \leq (c'_1)^2 \bar{\sigma} \Gamma < \infty, \end{aligned}$$

where $\Gamma := \int_0^\infty \eta(s)^2 ds$. By L'Hopital's rule, we have that

$$\begin{aligned} &\lim_{t \rightarrow \infty} \exp\left(-c_1 \int_0^t \eta(s) ds\right) \left[\int_0^t \exp\left(c_1 \int_0^s \eta(\tau) d\tau\right) c_1 \eta(s) ds \right] \\ &= \lim_{t \rightarrow \infty} \frac{c_1 \exp\left(c_1 \int_0^t \eta(s) ds\right) \eta(t)}{c_1 \exp\left(c_1 \int_0^t \eta(s) ds\right) \eta(t)} = 1. \end{aligned}$$

Thus, we have $\limsup_t \|\bar{\mathbf{m}}_t\| \leq \ell$. Consequently, there exists a constant C such that $\sup_t \|\bar{\mathbf{m}}_t\| \leq C < \infty$. By definition, $\mathbb{E}[\mathbf{m}_t \mathbf{m}_t^\top] = \bar{\mathbf{P}}_t + \bar{\mathbf{m}}_t \bar{\mathbf{m}}_t^\top$. Therefore, for any $t \geq 0$, we have $\|\mathbb{E}[\mathbf{m}_t \mathbf{m}_t^\top]\|_{\text{op}} \leq (c'_1)^2 \bar{\sigma} \Gamma + C^2$. Note that

$$\mathbb{E} \left[\|\mathbf{m}_t\|^2 \right] = \text{Tr} \left(\mathbb{E}[\mathbf{m}_t \mathbf{m}_t^\top] \right) \leq N \left\| \mathbb{E}[\mathbf{m}_t \mathbf{m}_t^\top] \right\|_{\text{op}}.$$

This proves the boundness of $\mathbb{E}[\|\mathbf{m}_t\|^2]$. Next, we prove the boundness of \mathbf{v}_t . By (Adam-SDE), the solution of \mathbf{v}_t is given by

$$\mathbf{v}_t = \exp\left(-\int_0^t c_2 \eta(s) ds\right) \int_0^t \exp\left(\int_0^s c_2 \eta(\tau) d\tau\right) c_2 \eta(s) \mathbf{d}_s ds,$$

where $\mathbf{d}_s := \text{diag}(\boldsymbol{\Sigma}(\mathbf{X}_s))$. By L'Hopital's rule, we have

$$\begin{aligned} \limsup_{t \rightarrow \infty} \|\mathbf{v}_t\|_\infty &\leq \sup_t \|\mathbf{d}_t\|_\infty \lim_{t \rightarrow \infty} \exp\left(-\int_0^t c_2 \eta(s) ds\right) \int_0^t \exp\left(\int_0^s c_2 \eta(\tau) d\tau\right) c_2 \eta(s) ds \\ &\leq \sup_t \|\mathbf{d}_t\|_\infty = \bar{\sigma}, \end{aligned}$$

Therefore, there exists constant $V > 0$ such that $\sup_{t \geq 0} \|\mathbf{v}_t\|_\infty \leq V$. This completes the proof. \blacksquare

B.2.3 PROOF OF THEOREM 2

Proof Apply Itô's formula to $\phi_1(\mathbf{X}_t, \mathbf{m}_t, \mathbf{v}_t) := f(\mathbf{X}_t) + \frac{1}{2c_1} \langle (\mathbf{v}_t + \epsilon)^{-\frac{1}{2}} \odot \mathbf{m}_t, \mathbf{m}_t \rangle$, we have

$$\begin{aligned}
& d\phi_1(\mathbf{X}_t, \mathbf{m}_t, \mathbf{v}_t) \\
&= -\eta(t) \langle \nabla f(\mathbf{X}_t), (\mathbf{v}_t + \epsilon)^{-\frac{1}{2}} \odot \mathbf{m}_t \rangle dt - \eta(t) \langle \mathbf{m}_t - \nabla f(\mathbf{X}_t), (\mathbf{v}_t + \epsilon)^{-\frac{1}{2}} \odot \mathbf{m}_t \rangle dt \\
&\quad + \frac{c_2\eta(t)}{4c_1} \langle (\mathbf{v}_t + \epsilon)^{-\frac{3}{2}} \odot \mathbf{m}_t^2, \mathbf{v}_t - \text{diag}(\boldsymbol{\Sigma}(\mathbf{X}_t)) \rangle dt + \frac{(c'_1)^2\eta(t)^2}{2c_1} \langle \text{Diag}((\mathbf{v}_t + \epsilon)^{-\frac{1}{2}}), \boldsymbol{\Sigma}(\mathbf{X}_t) \rangle dt \\
&\quad + \frac{c'_1}{c_1} \eta(t) \langle (\mathbf{v}_t + \epsilon)^{-\frac{1}{2}} \odot \mathbf{m}_t, \sigma(\mathbf{X}_t) d\mathbf{W}_t \rangle \\
&\leq - \left(1 - \frac{c_2}{4c_1}\right) \eta(t) \langle (\mathbf{v}_t + \epsilon)^{-\frac{1}{2}} \odot \mathbf{m}_t, \mathbf{m}_t \rangle dt + \frac{(c'_1)^2\eta(t)^2}{2c_1} \langle \text{Diag}((\mathbf{v}_t + \epsilon)^{-\frac{1}{2}}), \boldsymbol{\Sigma}(\mathbf{X}_t) \rangle dt \\
&\quad + \frac{c'_1}{c_1} \eta(t) \langle (\mathbf{v}_t + \epsilon)^{-\frac{1}{2}} \odot \mathbf{m}_t, \sigma(\mathbf{X}_t) d\mathbf{W}_t \rangle,
\end{aligned}$$

where the last inequality is derived by noting that $\mathbf{v}_t \geq 0$ and $(\mathbf{v}_t + \epsilon)^{-\frac{3}{2}} \odot \mathbf{v}_t \leq (\mathbf{v}_t + \epsilon)^{-\frac{1}{2}}$. Taking integral and then taking expectation, we have

$$\begin{aligned}
& \mathbb{E}[\phi_1(\mathbf{X}_t, \mathbf{m}_t, \mathbf{v}_t) - \phi_1(\mathbf{X}_0, \mathbf{m}_0, \mathbf{v}_0)] \\
&\leq -\mathbb{E} \left[\int_0^t \left(1 - \frac{c_2}{4c_1}\right) \eta(s) \langle (\mathbf{v}_s + \epsilon)^{-\frac{1}{2}} \odot \mathbf{m}_s, \mathbf{m}_s \rangle ds \right] \\
&\quad + \mathbb{E} \left[\int_0^t \frac{(c'_1)^2\eta(s)^2}{2c_1} \langle \text{Diag}((\mathbf{v}_s + \epsilon)^{-\frac{1}{2}}), \boldsymbol{\Sigma}(\mathbf{X}_s) \rangle ds \right].
\end{aligned}$$

Therefore, it holds that

$$\mathbb{E} \left[\|\mathbf{m}_t\|^2 \right] \leq \frac{\sqrt{V + \epsilon} (\phi_1(\mathbf{X}_0, \mathbf{m}_0, \mathbf{v}_0) - f_{\min})}{\left(1 - \frac{c_2}{4c_1}\right) \int_0^t \eta(s) ds} + \frac{\frac{(c'_1)^2}{2c_1} \bar{\sigma} \sqrt{V + \epsilon} \int_0^t \eta(s)^2 ds}{\left(1 - \frac{c_2}{4c_1}\right) \sqrt{\epsilon} \int_0^t \eta(s) ds}. \quad (23)$$

Next, we derive the bound for the gradient. We construct a novel Lyapunov function $\phi_2(\mathbf{X}_t, \mathbf{m}_t, \mathbf{v}_t) := f(\mathbf{X}_t) - \frac{1}{c_1} \langle \nabla f(\mathbf{X}_t), (\mathbf{v}_t + \epsilon)^{-\frac{1}{2}} \odot \mathbf{m}_t \rangle$ which links the noiseless gradient with the momentum. Applying Itô's formula to ϕ_2 yields that

$$\begin{aligned}
& d\phi_2(\mathbf{X}_t, \mathbf{m}_t, \mathbf{v}_t) \\
&= -\eta(t) \langle \nabla f(\mathbf{X}_t), (\mathbf{v}_t + \epsilon)^{-\frac{1}{2}} \odot \mathbf{m}_t \rangle dt + \frac{\eta(t)}{c_1} \langle \nabla^2 f(\mathbf{X}_t) (\mathbf{v}_t + \epsilon)^{-\frac{1}{2}} \odot \mathbf{m}_t, (\mathbf{v}_t + \epsilon)^{-\frac{1}{2}} \odot \mathbf{m}_t \rangle dt \\
&\quad + \eta(t) \langle \nabla f(\mathbf{X}_t) \odot (\mathbf{v}_t + \epsilon)^{-\frac{1}{2}}, \mathbf{m}_t - \nabla f(\mathbf{X}_t) \rangle dt - \frac{c'_1\eta(t)}{c_1} \langle \nabla f(\mathbf{X}_t) \odot (\mathbf{v}_t + \epsilon)^{-\frac{1}{2}}, \sigma(\mathbf{X}_t) d\mathbf{W}_t \rangle \\
&\quad - \frac{c_2\eta(t)}{2c_1} \langle \nabla f(\mathbf{X}_t) \odot \mathbf{m}_t \odot (\mathbf{v}_t + \epsilon)^{-\frac{3}{2}}, \mathbf{v}_t - \text{diag}(\boldsymbol{\Sigma}(\mathbf{X}_t)) \rangle dt.
\end{aligned}$$

Taking integral and taking expectation, we have

$$\begin{aligned}
& \mathbb{E} [\phi_2(\mathbf{X}_0, \mathbf{m}_0, \mathbf{v}_0) - \phi_2(\mathbf{X}_t, \mathbf{m}_t, \mathbf{v}_t)] \\
& \leq \frac{L}{c_1} \mathbb{E} \left[\int_0^t \eta(s) \left\| \mathbf{m}_s \odot (\mathbf{v}_s + \epsilon)^{-\frac{1}{2}} \right\|^2 ds \right] - \mathbb{E} \left[\int_0^t \eta(s) \left\langle \nabla f(\mathbf{X}_s) \odot (\mathbf{v}_s + \epsilon)^{-\frac{1}{2}}, \nabla f(\mathbf{X}_s) \right\rangle ds \right] \\
& \quad - \frac{c_2}{2c_1} \mathbb{E} \left[\int_0^t \eta(s) \left\langle \nabla f(\mathbf{X}_s) \odot \mathbf{m}_s \odot (\mathbf{v}_s + \epsilon)^{-\frac{3}{2}}, \mathbf{v}_s \right\rangle ds \right] \\
& \quad + \frac{c_2 \bar{\sigma}}{2c_1} \mathbb{E} \left[\int_0^t \eta(s) \left\langle \nabla f(\mathbf{X}_s) \odot \mathbf{m}_s, (\mathbf{v}_s + \epsilon)^{-\frac{3}{2}} \right\rangle ds \right] \\
& \leq \frac{L}{c_1 \epsilon} \mathbb{E} \left[\int_0^t \eta(s) \|\mathbf{m}_s\|^2 ds \right] - \frac{1}{\sqrt{V + \epsilon}} \mathbb{E} \left[\int_0^t \eta(s) \|\nabla f(\mathbf{X}_s)\|^2 ds \right] \\
& \quad + \frac{1}{4\sqrt{V + \epsilon}} \mathbb{E} \left[\int_0^t \eta(s) \|\nabla f(\mathbf{X}_s)\|^2 ds \right] + \frac{c_2^2 \sqrt{V + \epsilon}}{4c_1^2 \epsilon} \mathbb{E} \left[\int_0^t \eta(s) \|\mathbf{m}_s\|^2 ds \right] \\
& \quad + \frac{1}{4\sqrt{V + \epsilon}} \mathbb{E} \left[\int_0^t \eta(s) \|\nabla f(\mathbf{X}_s)\|^2 ds \right] + \frac{c_2^2 \bar{\sigma}^2 \sqrt{V + \epsilon}}{4\epsilon^3 c_1^2} \mathbb{E} \left[\int_0^t \eta(s) \|\mathbf{m}_s\|^2 ds \right], \\
& = \frac{L}{c_1 \epsilon} \mathbb{E} \left[\int_0^t \eta(s) \|\mathbf{m}_s\|^2 ds \right] - \frac{1}{2\sqrt{V + \epsilon}} \mathbb{E} \left[\int_0^t \eta(s) \|\nabla f(\mathbf{X}_s)\|^2 ds \right] \\
& \quad + \left(1 + \frac{\bar{\sigma}^2}{\epsilon^2} \right) \frac{c_2^2 \sqrt{V + \epsilon}}{4c_1^2 \epsilon} \mathbb{E} \left[\int_0^t \eta(s) \|\mathbf{m}_s\|^2 ds \right].
\end{aligned}$$

The last inequality comes from Cauchy-Young's inequality:

$$\begin{aligned}
& \frac{c_2}{2c_1} \left| \left\langle \nabla f(\mathbf{X}_s) \odot \mathbf{m}_s \odot (\mathbf{v}_s + \epsilon)^{-\frac{3}{2}}, \mathbf{v}_s \right\rangle \right| = \frac{c_2}{2c_1} \left| \left\langle \nabla f(\mathbf{X}_s) \odot \mathbf{v}_s \odot (\mathbf{v}_s + \epsilon)^{-\frac{3}{2}}, \mathbf{m}_s \right\rangle \right| \\
& \leq \frac{c_2}{2c_1 \sqrt{\epsilon}} \left| \left\langle \nabla f(\mathbf{X}_s), \mathbf{m}_s \right\rangle \right| \leq \frac{c_2}{2c_1 \sqrt{\epsilon}} \|\nabla f(\mathbf{X}_s)\| \|\mathbf{m}_s\| \leq \frac{1}{4\sqrt{V + \epsilon}} \|\nabla f(\mathbf{X}_s)\|^2 + \frac{c_2^2 \sqrt{V + \epsilon}}{4c_1^2 \epsilon} \|\mathbf{m}_s\|^2.
\end{aligned}$$

and similarly,

$$\frac{c_2 \bar{\sigma}}{2c_1} \left| \left\langle \nabla f(\mathbf{X}_s) \odot \mathbf{m}_s, (\mathbf{v}_s + \epsilon)^{-\frac{3}{2}} \right\rangle \right| \leq \frac{1}{4\sqrt{V + \epsilon}} \|\nabla f(\mathbf{X}_s)\|^2 + \frac{c_2^2 \bar{\sigma}^2 \sqrt{V + \epsilon}}{4\epsilon^3 c_1^2} \|\mathbf{m}_s\|^2.$$

Then, we have

$$\begin{aligned}
\mathbb{E} \left[\|\nabla f(\mathbf{X}_t)\|^2 \right] & \leq \frac{2\sqrt{V + \epsilon} (\phi_2(\mathbf{X}_0, \mathbf{m}_0, \mathbf{v}_0) - \min_t \mathbb{E} [\phi_2(\mathbf{X}_t, \mathbf{m}_t, \mathbf{v}_t)])}{\int_0^t \eta(s) ds} \\
& \quad + \left(\frac{2L\sqrt{V + \epsilon}}{c_1 \epsilon} + \left(1 + \frac{\bar{\sigma}^2}{\epsilon^2} \right) \frac{c_2^2 (V + \epsilon)}{2c_1^2 \epsilon} \right) \mathbb{E} \left[\|\mathbf{m}_t\|^2 \right].
\end{aligned}$$

Note that $\left| \mathbb{E} \left[\left\langle \nabla f(\mathbf{X}_t), (\mathbf{v}_t + \epsilon)^{-\frac{1}{2}} \odot \mathbf{m}_t \right\rangle \right] \right| \leq \frac{\ell}{\sqrt{\epsilon}} \sqrt{\mathbb{E} \left[\|\mathbf{m}_t\|^2 \right]} \leq \frac{\ell M \sqrt{N}}{\sqrt{\epsilon}}$. Combined with (23), we prove the bound for $\mathbb{E} \left[\|\nabla f(\mathbf{X}_t)\|^2 \right]$. This completes the proof. \blacksquare

B.3 Proofs for Escaping Probability

B.3.1 PROOF OF PROPOSITION 5

Proof Note that $\nabla f(\mathbf{x}^*) = 0$, we have $\frac{d\bar{\mathbf{x}}_t}{dt} = \mathbf{0}$. So $\bar{\mathbf{x}}_t$ remains constant at \mathbf{x}^* , and $\nabla^2 f(\bar{\mathbf{x}}_t) \equiv \nabla^2 f(\mathbf{x}^*)$. Then, the ODE (16) comes from (SDE-GA). Let $\mathbf{p}(t) = \text{vec}(\mathbf{P}(t))$, $\mathbf{b} = \text{vec}(\mathbf{\Sigma})$, where $\text{vec}(\cdot)$ is the vectorization of a matrix by column order. Then (16) for $\mathbf{P}(t)$ is equivalent to the following ODE for vector-valued function $\mathbf{p}(t)$:

$$\frac{d\mathbf{p}(t)}{dt} = -\eta(t)\mathbf{Q}\mathbf{p}(t) + \eta_0\eta(t)^2\mathbf{b},$$

where $\mathbf{Q} = \mathbf{I} \otimes \mathbf{H} + \mathbf{H} \otimes \mathbf{I}$, where \otimes is the Kronecker product. Then, we have

$$\mathbf{p}(t) = \exp\left(-\int_0^t \eta(s)\mathbf{Q}ds\right) \left(\int_0^t \exp\left(\int_0^s \eta(\tau)\mathbf{Q}d\tau\right) \eta_0\eta(s)^2\mathbf{b}ds\right).$$

Note that

$$\begin{aligned} & \exp\left(\int_0^s \eta(\tau)(\mathbf{I} \otimes \mathbf{H} + \mathbf{H} \otimes \mathbf{I})d\tau\right) \text{vec}(\mathbf{\Sigma}) \\ &= \exp\left(\mathbf{H} \int_0^s \eta(\tau)d\tau\right) \otimes \exp\left(\mathbf{H} \int_0^s \eta(\tau)d\tau\right) \text{vec}(\mathbf{\Sigma}) \\ &= \text{vec}\left(\exp\left(\mathbf{H} \int_0^s \eta(\tau)d\tau\right) \mathbf{\Sigma} \exp\left(\mathbf{H} \int_0^s \eta(\tau)d\tau\right)\right). \end{aligned}$$

Denote $\mathbf{A}(t) := \exp\left(-\int_0^t \eta(s)\mathbf{H}ds\right)$. Then, it holds that $(\mathbf{A}(t))^{-1} := \exp\left(\int_0^t \eta(s)\mathbf{H}ds\right)$. Hence, we obtain:

$$\begin{aligned} \mathbf{p}(t) &= \exp\left(-\int_0^t \eta(s)(\mathbf{I} \otimes \mathbf{H} + \mathbf{H} \otimes \mathbf{I})ds\right) \text{vec}\left(\int_0^t ((\mathbf{A}(s))^{-1})\mathbf{\Sigma}((\mathbf{A}(s))^{-1})\eta_0\eta(s)^2ds\right) \\ &= \mathbf{A}(t) \otimes \mathbf{A}(t) \text{vec}\left(\int_0^t ((\mathbf{A}(s))^{-1})\mathbf{\Sigma}((\mathbf{A}(s))^{-1})\eta_0\eta(s)^2ds\right) \\ &= \text{vec}\left(\mathbf{A}(t) \left(\int_0^t ((\mathbf{A}(s))^{-1})\mathbf{\Sigma}((\mathbf{A}(s))^{-1})\eta_0\eta(s)^2ds\right) \mathbf{A}(t)\right). \end{aligned}$$

Consequently, the matrix $\mathbf{P}(t)$ is expressed as:

$$\mathbf{P}(t) = \mathbf{A}(t) \left(\int_0^t ((\mathbf{A}(s))^{-1})\mathbf{\Sigma}((\mathbf{A}(s))^{-1})\eta_0\eta(s)^2ds\right) \mathbf{A}(t).$$

This completes the proof. ■

B.3.2 PROOF OF PROPOSITION 6

We first recall the Gaussian approximations for a general SDE (Särkkä and Solin, 2019). Considering the SDE with initial condition $\mathbf{x}_{t_0} = \mathbf{x}_0$:

$$d\mathbf{x}_t = \mathbf{G}(\mathbf{x}, t)dt + \mathbf{L}(\mathbf{x}, t)d\mathbf{W}_t$$

the linearization approximation of its FPK equation yields the following differential equations for $\bar{\mathbf{x}}(t) = \mathbb{E}[\mathbf{x}_t]$ and $\mathbf{P}(t) = \text{Cov}(\mathbf{x}_t)$ with the initial condition $\bar{\mathbf{x}}_{t_0} = \mathbb{E}[\mathbf{x}_0]$, $\mathbf{P}_{t_0} = \text{Cov}(\mathbf{x}_{t_0})$:

$$\begin{cases} \frac{d\bar{\mathbf{x}}}{dt} = \mathbf{G}(\bar{\mathbf{x}}, t) \\ \frac{d\mathbf{P}}{dt} = \mathbf{P}\mathbf{G}_{\mathbf{x}}^{\top}(\bar{\mathbf{x}}, t) + \mathbf{G}_{\mathbf{x}}(\bar{\mathbf{x}}, t)\mathbf{P} + \mathbf{L}(\bar{\mathbf{x}}, t)\mathbf{L}(\bar{\mathbf{x}}, t)^{\top}. \end{cases} \quad (\text{general-GA})$$

Proof Let $\mathbf{Z}_0 := [\mathbf{X}_0; \mathbf{m}_0; \mathbf{v}_0] = [\mathbf{x}^*; \mathbf{0}; \text{diag}(\boldsymbol{\Sigma}(\mathbf{x}^*))]$. Then $\bar{\mathbf{z}}_0 = \mathbf{Z}_0$ is a zero of $\mathbf{F}(\mathbf{Z})$ defined in (18). Therefore, the trajectory $\bar{\mathbf{z}}_t$ remains at \mathbf{Z}_0 . Note that $\frac{\partial F(\mathbf{Z}_0)}{\partial \mathbf{Z}} = \widehat{\mathbf{H}}$. Then (20) can be derived by substituting $\bar{\mathbf{z}}_t = \mathbf{Z}_0$, (18) and (19) into (general-GA). The remainder of the proof follows similarly to that of Proposition 5, and thus is omitted for brevity. ■

B.3.3 ANTI-CONCENTRATION FOR GAUSSIAN

Before proving the main results for the escape probability, we need a general anti-concentration inequality for Gaussian variables, as considered in other scenarios (Carbery and Wright, 2001; Tu and Boczar, 2023).

Lemma 1 Assume $\mathbf{x} \sim \mathcal{N}(\boldsymbol{\mu}, \boldsymbol{\Sigma})$, for any $\varepsilon \in (0, \text{Tr}(\boldsymbol{\Sigma}))$, we have

$$\mathbb{P}\left[\|\mathbf{x} - \boldsymbol{\mu}\|^2 \leq \varepsilon\right] \leq \sqrt{\frac{e\varepsilon}{\text{Tr}(\boldsymbol{\Sigma})}}.$$

Proof Applying Chernoff's bound, we have:

$$\begin{aligned} \mathbb{P}\left[\|\mathbf{x} - \boldsymbol{\mu}\|^2 \leq \varepsilon\right] &\leq \inf_{\lambda > 0} \left\{ \exp(\lambda\varepsilon) \int_{\mathbb{R}^N} \frac{1}{\sqrt{(2\pi)^N \det^*(\boldsymbol{\Sigma})}} \exp\left(-\lambda\|\mathbf{x}\|^2 - \frac{1}{2}\mathbf{x}^{\top}\boldsymbol{\Sigma}^{\dagger}\mathbf{x}\right) d\mathbf{x} \right\} \\ &= \inf_{\lambda > 0} \left\{ \exp(\lambda\varepsilon) \int_{\mathbb{R}^N} \frac{1}{\sqrt{(2\pi)^N \det^*(\boldsymbol{\Sigma})}} \exp\left(-\frac{1}{2}\mathbf{x}^{\top}(2\lambda\mathbf{I}_N + \boldsymbol{\Sigma}^{\dagger})\mathbf{x}\right) d\mathbf{x} \right\} \\ &= \inf_{\lambda > 0} \left\{ \exp(\lambda\varepsilon) \sqrt{\frac{(2\pi)^N \det\left((2\lambda\mathbf{I}_N + \boldsymbol{\Sigma}^{\dagger})^{-1}\right)}{(2\pi)^N \det^*(\boldsymbol{\Sigma})}} \right\} = \inf_{\lambda > 0} \left\{ \exp(\lambda\varepsilon) \frac{1}{\sqrt{\det(2\lambda\boldsymbol{\Sigma} + \mathbf{I}_N)}} \right\} \\ &\stackrel{(a)}{\leq} \inf_{\lambda > 0} \left\{ \exp(\lambda\varepsilon) \frac{1}{\sqrt{1 + 2\lambda \text{Tr}(\boldsymbol{\Sigma})}} \right\} \stackrel{(b)}{=} \sqrt{\frac{\varepsilon}{\text{Tr}(\boldsymbol{\Sigma})}} \exp\left(\frac{\text{Tr}(\boldsymbol{\Sigma}) - \varepsilon}{2\text{Tr}(\boldsymbol{\Sigma})}\right) \leq \sqrt{\frac{e\varepsilon}{\text{Tr}(\boldsymbol{\Sigma})}}, \end{aligned}$$

where $\boldsymbol{\Sigma}^{\dagger}$ is the Moore-Penrose pseudoinverse of $\boldsymbol{\Sigma}$ and $\det^*(\cdot)$ is the pseudo-determinant. In the above, (a) comes from

$$\det(2\lambda\boldsymbol{\Sigma} + \mathbf{I}_N) = \prod_{i=1}^N (1 + 2\lambda\sigma_i) \geq 1 + 2\lambda \sum_{i=1}^N \sigma_i = 1 + 2\lambda \text{Tr}(\boldsymbol{\Sigma}).$$

where σ_i is the i -th eigenvalue of $\boldsymbol{\Sigma}$, and (b) is optimized by setting $\lambda = \frac{\text{Tr}(\boldsymbol{\Sigma}) - \varepsilon}{2\varepsilon \text{Tr}(\boldsymbol{\Sigma})}$. ■

B.3.4 PROOF OF THEOREM 3

Proof Let \mathbf{U} be an orthogonal matrix such that $\mathbf{H} = \mathbf{U}\mathbf{\Lambda}\mathbf{U}^\top$, where $\mathbf{\Lambda}$ is the diagonal matrix of eigenvalues of \mathbf{H} . Let λ_{\max} be the maximal eigenvalue of \mathbf{H} . By equation (17), we have that

$$\begin{aligned} \text{Tr}(\mathbf{P}(t)) &= \text{Tr} \left(\int_0^t \exp \left(-\mathbf{H} \int_s^t \eta(\tau) d\tau \right) \mathbf{\Sigma} \exp \left(-\mathbf{H} \int_s^t \eta(\tau) d\tau \right) \eta_0 \eta(s)^2 ds \right) \\ &= \text{Tr} \left(\int_0^t \exp \left(-\mathbf{\Lambda} \int_s^t \eta(\tau) d\tau \right) \mathbf{U}^\top \mathbf{\Sigma} \mathbf{U} \exp \left(-\mathbf{\Lambda} \int_s^t \eta(\tau) d\tau \right) \eta_0 \eta(s)^2 ds \right) \\ &\geq \eta_0 \text{Tr}(\mathbf{\Sigma}) \int_0^t \exp \left(-2\lambda_{\max} \int_s^t \eta(\tau) d\tau \right) \eta(s)^2 ds \\ &\geq \eta_0 \text{Tr}(\mathbf{\Sigma}) \int_0^t \exp(-2\lambda_{\max} \eta_{\max}(t-s)) \eta(s)^2 ds \\ &\geq C \eta_0 \text{Tr}(\mathbf{\Sigma}) \int_0^t \eta(s)^2 ds, \end{aligned}$$

where $C := \inf_{t \geq 0} \frac{\int_0^t \exp(-2\lambda_{\max} \eta_{\max}(t-s)) \eta(s)^2 ds}{\int_0^t \eta(s)^2 ds}$. Next, we demonstrate that $C > 0$ by considering two cases. When $\int_0^\infty \eta(s)^2 ds < \infty$, it is clear that $C > 0$. When $\int_0^\infty \eta(s)^2 ds = \infty$, by L'Hopital's rule, we have

$$\lim_{t \rightarrow \infty} \frac{\int_0^t \exp(-2\lambda_{\max} \eta_{\max}(t-s)) \eta(s)^2 ds}{\int_0^t \eta(s)^2 ds} = \lim_{t \rightarrow \infty} \frac{\eta(t)^2}{\eta(t)^2} = 1.$$

Thus, $C > 0$. The condition $\eta(0) = \eta_{\max}$ and $\eta(T) = 0$ leads to the following inequality derived from the Cauchy-Schwarz inequality:

$$\left(\int_0^T \eta(s)^2 ds \right) \left(\int_0^T \eta'(s)^2 ds \right) \geq \left(\int_0^T \eta(s) \eta'(s) ds \right)^2.$$

Integrating by parts yields:

$$\int_0^T \eta(s) \eta'(s) ds = \eta(s)^2 \Big|_0^T - \int_0^T \eta(s) \eta'(s) ds,$$

which results in

$$\int_0^T \eta(s) \eta'(s) ds = -\frac{\eta_{\max}^2}{2}.$$

This result leads to the following inequality:

$$\frac{\left(\frac{\eta_{\max}^2}{2} \right)^2}{\int_0^T \eta(s)^2 ds} \leq \int_0^T \eta'(s)^2 ds.$$

Now, suppose Assumption 2 holds. For any fix $\delta \in (0, 1)$, by Proposition 2 and setting $t = \delta \text{Tr}(\mathbf{\Sigma}_g)$, we have

$$\begin{aligned} &\mathbb{P} \{ (1 - \delta) \text{Tr}(\mathbf{\Sigma}_g) \leq \text{Tr}(\mathbf{\Sigma}(\mathbf{x})) \leq (1 + \delta) \text{Tr}(\mathbf{\Sigma}_g) \} \\ &\geq 1 - 2 \exp \left\{ -\frac{D\delta^2 (\text{Tr}(\mathbf{\Sigma}_g))^2}{4 \text{Tr}(\mathbf{\Sigma}_g^2) + 2\delta \text{Tr}(\mathbf{\Sigma}_g) \|\mathbf{\Sigma}_g\|_{\text{op}}} \right\}. \end{aligned}$$

Denote the event $\mathcal{E} := \{(1-\delta) \text{Tr}(\boldsymbol{\Sigma}_g) \leq \text{Tr}(\boldsymbol{\Sigma}(\mathbf{x})) \leq (1+\delta) \text{Tr}(\boldsymbol{\Sigma}_g)\}$ and $\mathcal{A} := \{\|\mathbf{X}_T - \mathbf{x}^*\|^2 \leq \varepsilon\}$. By Proposition 5, $\mathbb{E}[\mathbf{X}_T] = \bar{\mathbf{x}}_T = \mathbf{x}^*$. Then, applying Lemma 1, we get

$$\begin{aligned} \mathbb{P}\left\{\|\mathbf{X}_T - \mathbf{x}^*\|^2 \leq \varepsilon \mid \mathcal{E}\right\} &\leq \sqrt{\frac{e\varepsilon}{\text{Tr}(\mathbf{P}_t)}} \leq \sqrt{\frac{e\varepsilon}{C\eta_0 \text{Tr}(\boldsymbol{\Sigma}) \left(\frac{\eta_{\max}^2}{2}\right)^2} \int_0^T \eta'(s)^2 ds} \\ &\leq \sqrt{\frac{e\varepsilon}{C\eta_0(1-\delta) \text{Tr}(\boldsymbol{\Sigma}_g) \left(\frac{\eta_{\max}^2}{2}\right)^2} \int_0^T \eta'(s)^2 ds}. \end{aligned}$$

Finally, we have

$$\begin{aligned} \mathbb{P}\{\mathcal{A}\} &= \mathbb{P}\{\mathcal{A} \mid \mathcal{E}\} \mathbb{P}\{\mathcal{E}\} + \mathbb{P}\{\mathcal{A} \mid \mathcal{E}^c\} \mathbb{P}\{\mathcal{E}^c\} \leq \mathbb{P}\{\mathcal{A} \mid \mathcal{E}\} + \mathbb{P}\{\mathcal{E}^c\} \\ &\leq \sqrt{\frac{e\varepsilon}{C\eta_0(1-\delta) \text{Tr}(\boldsymbol{\Sigma}_g) \left(\frac{\eta_{\max}^2}{2}\right)^2} \int_0^T \eta'(s)^2 ds} + 2 \exp\left\{-\frac{D\delta^2(\text{Tr}(\boldsymbol{\Sigma}_g))^2}{4 \text{Tr}(\boldsymbol{\Sigma}_g^2) + 2\delta \text{Tr}(\boldsymbol{\Sigma}_g) \|\boldsymbol{\Sigma}_g\|_{\text{op}}}\right\}. \end{aligned}$$

Since $D \gg N$, the second term is sufficiently small compared with the first term. Finally, we derive the bound

$$\mathbb{P}[\|\mathbf{X}_T - \mathbf{x}^*\|^2 \leq \varepsilon] = \mathcal{O}\left(\left(\frac{\varepsilon}{\eta_{\max}^4 \sigma_g^2} \int_0^T \eta'(s)^2 ds\right)^{1/2}\right).$$

This completes the proof. \blacksquare

B.3.5 PROOF OF THEOREM 4

Proof The proof follows similarly to the proof of Theorem 3, and hence we omit the details. \blacksquare

Appendix C. Limitations and Scope of Validity

The Opt-Laws framework is developed for learning-rate schedules that start from zero, vary over time, and decay to zero. Below we describe the boundary conditions of the current formulation. First, for fixed learning-rate schedules the derivative terms η'_t vanish, and the escape-related features reduce to zero. The law then contains only convergence and scale terms, which overlaps with the role of standard scaling laws. Opt-Laws is therefore most informative for schedules with nontrivial warmup and cooldown phases. Second, the SDE escape analysis (Theorems 3 and 4) assumes that the learning rate eventually decays to zero, which is standard in the SDE optimization literature. When the final learning rate is non-zero, the escape bounds require further extension. Generalizing the analysis to non-zero terminal LR is an interesting direction for future work. Third, the current empirical validation covers piecewise-linear, cosine, constant-plus-linear, and polygon schedule families. More complex schedule types such as cyclic schedules or warmup restarts have not been tested and remain a direction for future investigation.

References

- J. Achiam, S. Adler, S. Agarwal, L. Ahmad, I. Akkaya, F. L. Aleman, et al. GPT-4 technical report. *arXiv preprint arXiv:2303.08774*, 2023.
- C. Archambeau, D. Cornford, M. Opper, and J. Shawe-Taylor. Gaussian process approximations of stochastic differential equations. *Journal of Machine Learning Research*, 1:1–16, 2007.
- Y. Arjevani, Y. Carmon, J. C. Duchi, D. J. Foster, N. Srebro, and B. Woodworth. Lower bounds for non-convex stochastic optimization. *Mathematical Programming*, pages 1–50, 2022.
- H. Attouch, Z. Chbani, J. Peypouquet, and P. Redont. Fast convergence of inertial dynamics and algorithms with asymptotic vanishing viscosity. *Mathematical Programming*, 168: 123–175, 2018.
- H. Attouch, Z. Chbani, and H. Riahi. Fast convex optimization via a third-order in time evolution equation: Toges-v an improved version of toges. *Optimization*, 73(3):575–595, 2024.
- J. Bai, S. Bai, Y. Chu, Z. Cui, K. Dang, X. Deng, et al. Qwen technical report. *arXiv preprint arXiv:2309.16609*, 2023.
- Z. Bai and J. W. Silverstein. *Spectral analysis of large dimensional random matrices*, volume 20. Springer, 2010.
- B. Battash, L. Wolf, and O. Lindenbaum. Revisiting the noise model of stochastic gradient descent. In *International Conference on Artificial Intelligence and Statistics*, pages 4780–4788. PMLR, 2024.
- N. Berglund. Kramers’ law: Validity, derivations and generalisations. *Markov Processes And Related Fields*, 19(3):459–490, 2013.
- N. Berglund and B. Gentz. Sharp estimates for metastable lifetimes in parabolic SPDEs: Kramers’ law and beyond. *Electronic Journal of Probability*, 18(24):1–58, 2013.
- S. Bergsma, N. S. Dey, G. Gosal, G. Gray, D. Soboleva, and J. Hestness. Straight to zero: Why linearly decaying the learning rate to zero works best for LLMs. In *The Thirteenth International Conference on Learning Representations*, 2025.
- D. P. Bertsekas and J. N. Tsitsiklis. Gradient convergence in gradient methods with errors. *SIAM Journal on Optimization*, 10(3):627–642, 2000.
- T. Besiroglu, E. Erdil, M. Barnett, and J. You. Chinchilla Scaling: A replication attempt. *arXiv preprint arXiv:2404.10102*, 2024.
- X. Bi, D. Chen, G. Chen, S. Chen, D. Dai, C. Deng, et al. DeepSeek LLM: Scaling open-source language models with longtermism. *arXiv preprint arXiv:2401.02954*, 2024.

- A. Bovier and F. Den Hollander. Metastability: a potential-theoretic approach. *Grundlehren der mathematischen Wissenschaften*, 351, 2015.
- E. Caballero, K. Gupta, I. Rish, and D. Krueger. Broken neural scaling laws. In *The Eleventh International Conference on Learning Representations*, 2023.
- A. Carbery and J. Wright. Distributional and L^q norm inequalities for polynomials over convex bodies in \mathbb{R}^n . *Mathematical Research Letters*, 8(3):233–248, 2001.
- H. Chen, Y. Dong, Z. Wei, Y. Huang, Y. Zhang, and J. Zhu. Exploring the basin-like loss landscape in large language models. In *The Fourteenth International Conference on Learning Representations*, 2026.
- X. Chen, S. Liu, R. Sun, and M. Hong. On the convergence of a class of adam-type algorithms for non-convex optimization. In *International Conference on Learning Representations*, 2019.
- T. Computer. RedPajama: An open dataset for training large language models, 2023. URL <https://github.com/togethercomputer/RedPajama-Data>.
- M. Dambrine, C. Dossal, B. Puig, and A. Rondepierre. Stochastic differential equations for modeling first order optimization methods. *SIAM Journal on Optimization*, 34(2):1402–1426, 2024.
- D. Davis, D. Drusvyatskiy, S. Kakade, and J. D. Lee. Stochastic subgradient method converges on tame functions. *Foundations of Computational Mathematics*, 20(1):119–154, 2020.
- DeepSeek-AI, A. Liu, B. Feng, B. Wang, B. Wang, B. Liu, et al. DeepSeek-V2: A strong, economical, and efficient mixture-of-experts language model. *arXiv preprint arXiv:2405.04434*, 2024.
- K. Ding and K.-C. Toh. Stochastic Bregman Subgradient Methods for Nonsmooth Nonconvex Optimization Problems. *arXiv preprint arXiv:2404.17386*, 2024.
- K. Ding, N. Xiao, and K.-C. Toh. Adam-family methods with decoupled weight decay in deep learning. *arXiv preprint arXiv:2310.08858*, 2023.
- A. Dubey, A. Jauhri, A. Pandey, A. Kadian, A. Al-Dahle, A. Letman, et al. The LLaMA 3 herd of models. *arXiv preprint arXiv:2407.21783*, 2024.
- J. C. Duchi and F. Ruan. Stochastic methods for composite and weakly convex optimization problems. *SIAM Journal on Optimization*, 28(4):3229–3259, 2018.
- P. Foret, A. Kleiner, H. Mobahi, and B. Neyshabur. Sharpness-aware minimization for efficiently improving generalization. *arXiv preprint arXiv:2010.01412*, 2020.
- L. Gao, J. Schulman, and J. Hilton. Scaling laws for reward model overoptimization. In *International Conference on Machine Learning*, pages 10835–10866. PMLR, 2023.

- B. Gess and S. Kassing. Convergence rates for momentum stochastic gradient descent with noise of machine learning type. *arXiv preprint arXiv:2302.03550*, 2023.
- S. Ghadimi and G. Lan. Stochastic first-and zeroth-order methods for nonconvex stochastic programming. *SIAM journal on optimization*, 23(4):2341–2368, 2013.
- I. I. Gihman and A. V. Skorohod. *Stochastic Differential Equations*. Springer New York, 1979.
- S. Goyal, P. Maini, Z. C. Lipton, A. Raghunathan, and J. Z. Kolter. Scaling laws for data filtering—data curation cannot be compute agnostic. In *Proceedings of the IEEE/CVF Conference on Computer Vision and Pattern Recognition*, pages 22702–22711, 2024.
- B. Grimmer, K. Shu, and A. Wang. Accelerated objective gap and gradient norm convergence for gradient descent via long steps. *arXiv preprint arXiv:2403.14045*, 2024.
- Y. Guo, J. Fu, H. Zhang, D. Zhao, and Y. Shen. Efficient continual pre-training by mitigating the stability gap. *arXiv preprint arXiv:2406.14833*, 2024.
- Z. Guo, Y. Xu, W. Yin, R. Jin, and T. Yang. A novel convergence analysis for algorithms of the Adam family. *arXiv preprint arXiv:2112.03459*, 2021.
- K. Gupta, B. Thérien, A. Ibrahim, M. L. Richter, Q. G. Anthony, E. Belilovsky, et al. Continual pre-training of large language models: How to re-warm your model? In *Workshop on Efficient Systems for Foundation Models@ ICML*, 2023.
- A. Hägele, E. Bakouch, A. Kosson, L. B. Allal, L. Von Werra, and M. Jaggi. Scaling laws and compute-optimal training beyond fixed training durations. *arXiv preprint arXiv:2405.18392*, 2024.
- F. He, T. Liu, and D. Tao. Control batch size and learning rate to generalize well: Theoretical and empirical evidence. *Advances in Neural Information Processing Systems*, 32, 2019.
- D. Hernandez, J. Kaplan, T. Henighan, and S. McCandlish. Scaling laws for transfer. *arXiv preprint arXiv:2102.01293*, 2021.
- J. Hoffmann, S. Borgeaud, A. Mensch, E. Buchatskaya, T. Cai, E. Rutherford, et al. Training compute-optimal large language models. *arXiv preprint arXiv:2203.15556*, 2022.
- S. Hu, Y. Tu, X. Han, C. He, G. Cui, X. Long, et al. Minicpm: Unveiling the potential of small language models with scalable training strategies. *arXiv preprint arXiv:2404.06395*, 2024.
- H. Ibayashi and M. Imaizumi. Why does sgd prefer flat minima?: Through the lens of dynamical systems. In *When Machine Learning meets Dynamical Systems: Theory and Applications*, 2023.
- A. Ibrahim, B. Thérien, K. Gupta, M. L. Richter, Q. Anthony, T. Lesort, et al. Simple and scalable strategies to continually pre-train large language models. *arXiv preprint arXiv:2403.08763*, 2024.

- B. Isik, N. Ponomareva, H. Hazimeh, D. Pappas, S. Vassilvitskii, and S. Koyejo. Scaling laws for downstream task performance of large language models. *arXiv preprint arXiv:2402.04177*, 2024.
- S. Jastrzębski, Z. Kenton, D. Arpit, N. Ballas, A. Fischer, et al. Three factors influencing minima in SGD. *arXiv preprint arXiv:1711.04623*, 2017.
- H. Jin, W. Wei, X. Wang, W. Zhang, and Y. Wu. Rethinking learning rate tuning in the era of large language models. *arXiv preprint arXiv:2309.08859*, 2023.
- J. Kaplan, S. McCandlish, T. Henighan, T. B. Brown, B. Chess, R. Child, et al. Scaling laws for neural language models. *arXiv preprint arXiv:2001.08361*, 2020.
- H. Karimi, J. Nutini, and M. Schmidt. Linear convergence of gradient and proximal-gradient methods under the polyak-łojasiewicz condition. In *Joint European conference on machine learning and knowledge discovery in databases*, pages 795–811. Springer, 2016.
- Z. Ke, Y. Shao, H. Lin, T. Konishi, G. Kim, and B. Liu. Continual pre-training of language models. *arXiv preprint arXiv:2302.03241*, 2023.
- N. S. Keskar, D. Mudigere, J. Nocedal, M. Smelyanskiy, and P. T. P. Tang. On large-batch training for deep learning: Generalization gap and sharp minima. *arXiv preprint arXiv:1609.04836*, 2016.
- G. Khromov and S. P. Singh. Some fundamental aspects about Lipschitz continuity of neural networks. In *The Twelfth International Conference on Learning Representations*, 2024.
- H. Kim, G. Papamakarios, and A. Mnih. The Lipschitz constant of self-attention. In *International Conference on Machine Learning*, pages 5562–5571. PMLR, 2021.
- D. P. Kingma and J. Ba. Adam: A method for stochastic optimization. *arXiv preprint arXiv:1412.6980*, 2014.
- P. E. Kloeden and E. Platen. *Numerical Solution to Stochastic Differential Equations*. Springer, 1999.
- H. A. Kramers. Brownian motion in a field of force and the diffusion model of chemical reactions. *Physical*, 7(4):284–304, 1940.
- M. Ledoux and B. Rider. Small deviations for beta ensembles. *Electronic Journal of Probability*, 15(41):1319–1343, 2010.
- J. D. Lee, I. Panageas, G. Piliouras, M. Simchowitz, M. I. Jordan, and B. Recht. First-order methods almost always avoid strict saddle points. *Mathematical programming*, 176:311–337, 2019.
- H. Li and Z. Lin. Restarted nonconvex accelerated gradient descent: No more polylogarithmic factor in the $\mathcal{O}(\epsilon^{-7/4})$ complexity. In *International Conference on Machine Learning*, pages 12901–12916. PMLR, 2022.

- Q. Li, C. Tai, and E. Weinan. Stochastic modified equations and adaptive stochastic gradient algorithms. In *International Conference on Machine Learning*, pages 2101–2110. PMLR, 2017.
- Q. Li, C. Tai, and E. Weinan. Stochastic modified equations and dynamics of stochastic gradient algorithms i: Mathematical foundations. *Journal of Machine Learning Research*, 20(40):1–47, 2019.
- X. Li, Z. Zhuang, and F. Orabona. A second look at exponential and cosine step sizes: Simplicity, adaptivity, and performance. In *International Conference on Machine Learning*, volume 139 of *Proceedings of Machine Learning Research*, pages 6553–6564. PMLR, 2021a.
- Z. Li, S. Malladi, and S. Arora. On the validity of modeling SGD with stochastic differential equations (SDEs). *Advances in Neural Information Processing Systems*, 34:12712–12725, 2021b.
- C. Liu, L. Zhu, and M. Belkin. Loss landscapes and optimization in over-parameterized non-linear systems and neural networks. *Applied and Computational Harmonic Analysis*, 59:85–116, 2022.
- I. Loshchilov and F. Hutter. Decoupled weight decay regularization. *arXiv preprint arXiv:1711.05101*, 2017.
- K. Luo, H. Wen, S. Hu, Z. Sun, M. Sun, Z. Liu, K. Lyu, and W. Chen. A multi-power law for loss curve prediction across learning rate schedules. In *The Thirteenth International Conference on Learning Representations*, 2025.
- K. Lv, Y. Yang, T. Liu, Q. Gao, Q. Guo, and X. Qiu. Full parameter fine-tuning for large language models with limited resources. *arXiv preprint arXiv:2306.09782*, 2023.
- S. Malladi, K. Lyu, A. Panigrahi, and S. Arora. On the SDEs and scaling rules for adaptive gradient algorithms. In *Advances in Neural Information Processing Systems*, 2022.
- R. Maulen-Soto, J. Fadili, and H. Attouch. An SDE perspective on stochastic convex optimization. *arXiv preprint arXiv:2207.02750*, 2022.
- R. Maulen-Soto, J. Fadili, H. Attouch, and P. Ochs. An SDE perspective on stochastic inertial gradient dynamics with time-dependent viscosity and geometric damping. *arXiv preprint arXiv:2407.04562*, 2024.
- R. May. Asymptotic for a second-order evolution equation with convex potential and vanishing damping term. *Turkish Journal of Mathematics*, 41(3):681–685, 2017.
- T. Mori, L. Ziyin, K. Liu, and M. Ueda. Power-law escape rate of SGD. In *International Conference on Machine Learning*, pages 15959–15975. PMLR, 2022.
- M. Muehlebach and M. Jordan. A dynamical systems perspective on Nesterov acceleration. In *International Conference on Machine Learning*, pages 4656–4662. PMLR, 2019.

- N. Muennighoff, A. Rush, B. Barak, T. Le Scao, N. Tazi, A. Piktus, et al. Scaling data-constrained language models. *Advances in Neural Information Processing Systems*, 36, 2024.
- Y. Nesterov. A method for solving the convex programming problem with convergence rate $O(1/k^2)$. In *Dokl akad nauk Sssr*, volume 269, page 543, 1983.
- T. H. Nguyen, U. Simsekli, M. Gurbuzbalaban, and G. Richard. First exit time analysis of stochastic gradient descent under heavy-tailed gradient noise. *Advances in Neural Information Processing Systems*, 32, 2019.
- J. Parmar, S. Satheesh, M. Patwary, M. Shoyebi, and B. Catanzaro. Reuse, don't retrain: A recipe for continued pretraining of language models. *arXiv preprint arXiv:2407.07263*, 2024.
- B. Polyak. *Introduction to Optimization*. Optimization Software, New York, 1987.
- S. J. Reddi, S. Kale, and S. Kumar. On the convergence of adam and beyond. In *International Conference on Learning Representations*, 2018.
- M. Reid, N. Savinov, D. Teplyashin, D. Lepikhin, T. Lillicrap, J.-b. Alayrac, et al. Gemini 1.5: Unlocking multimodal understanding across millions of tokens of context. *arXiv preprint arXiv:2403.05530*, 2024.
- J. S. Rosenfeld, A. Rosenfeld, Y. Belinkov, and N. Shavit. A constructive prediction of the generalization error across scales. In *International Conference on Learning Representations*, 2020.
- T. Rotaru, F. Glineur, and P. Patrinos. Exact worst-case convergence rates of gradient descent: a complete analysis for all constant stepsizes over nonconvex and convex functions. *arXiv preprint arXiv:2406.17506*, 2024.
- N. Sardana, J. Portes, S. Doubov, and J. Frankle. Beyond Chinchilla-optimal: Accounting for inference in language model scaling laws. In *International Conference on Machine Learning*, 2024.
- S. Särkkä and J. Sarmavuori. Gaussian filtering and smoothing for continuous-discrete dynamic systems. *Signal Processing*, 93(2):500–510, 2013.
- S. Särkkä and A. Solin. *Applied Stochastic Differential Equations*, volume 10. Cambridge University Press, 2019.
- S. Särkkä, J. Hartikainen, I. S. Mbalawata, and H. Haario. Posterior inference on parameters of stochastic differential equations via non-linear gaussian filtering and adaptive MCMC. *Statistics and Computing*, 25(2):427–437, 2015.
- H. Shen and T. Chen. A single-timescale analysis for stochastic approximation with multiple coupled sequences. *Advances in Neural Information Processing Systems*, 35:17415–17429, 2022.

- D. Shrivastava, D. Kocetkov, H. de Vries, D. Bahdanau, and T. Scholak. Repofusion: Training code models to understand your repository. *arXiv preprint arXiv:2306.10998*, 2023.
- U. Simsekli, L. Sagun, and M. Gurbuzbalaban. A tail-index analysis of stochastic gradient noise in deep neural networks. In *International Conference on Machine Learning*, pages 5827–5837. PMLR, 2019.
- A. Solin, E. Tamir, and P. Verma. Scalable inference in SDEs by direct matching of the Fokker–Planck–Kolmogorov equation. *Advances in Neural Information Processing Systems*, 34:417–429, 2021.
- R. M. Soto, J. Fadili, and H. Attouch. An SDE perspective on stochastic convex optimization. *arXiv preprint arXiv:2207.02750*, 2022.
- W. Su, S. Boyd, and E. Candes. A differential equation for modeling Nesterov’s accelerated gradient method: Theory and insights. *Advances in Neural Information Processing Systems*, 27, 2014.
- H. Tissue, V. Wang, and L. Wang. Scaling law with learning rate annealing. In *The Thirteenth International Conference on Learning Representations*, 2025.
- S. Tu and R. Boczar. An elementary proof of anti-concentration for degree two non-negative gaussian polynomials. *arXiv preprint arXiv:2301.05992*, 2023.
- X. Wang, S. Magnússon, and M. Johansson. On the convergence of step decay step-size for stochastic optimization. *Advances in Neural Information Processing Systems*, 34: 14226–14238, 2021.
- T. Wei, B. Zhu, L. Zhao, C. Cheng, B. Li, W. Lü, et al. Skywork-MoE: A deep dive into training techniques for mixture-of-experts language models. *arXiv preprint arXiv:2406.06563*, 2024.
- N. Xiao, X. Hu, and K.-C. Toh. Convergence guarantees for stochastic subgradient methods in nonsmooth nonconvex optimization. *arXiv preprint arXiv:2307.10053*, 2023.
- N. Xiao, X. Hu, X. Liu, and K.-C. Toh. Adam-family methods for nonsmooth optimization with convergence guarantees. *Journal of Machine Learning Research*, 25(48):1–53, 2024.
- X. Xie, Q. Wang, Z. Ling, X. Li, G. Liu, and Z. Lin. Optimization induced equilibrium networks: An explicit optimization perspective for understanding equilibrium models. *IEEE Transactions on Pattern Analysis and Machine Intelligence*, 45(3):3604–3616, 2022.
- X. Xie, Z. Lin, K.-C. Toh, and P. Zhou. LoCo: Low-bit communication adaptor for large-scale model training. *arXiv preprint arXiv:2407.04480*, 2024a.
- X. Xie, P. Zhou, H. Li, Z. Lin, and S. Yan. Adan: Adaptive Nesterov momentum algorithm for faster optimizing deep models. *IEEE Transactions on Pattern Analysis and Machine Intelligence*, 2024b.

- X. Xie, Z. Yu, Y. Liao, T. Wang, K.-C. Toh, and S. Yan. Slow-fast inference: Training-free inference acceleration via within-sentence support stability. *arXiv preprint arXiv:2603.12038*, 2026.
- Z. Xie, I. Sato, and M. Sugiyama. A diffusion theory for deep learning dynamics: Stochastic gradient descent exponentially favors flat minima. In *International Conference on Learning Representations*, 2020.
- A. Yang, B. Yang, B. Hui, B. Zheng, B. Yu, C. Zhou, et al. Qwen2 technical report. *arXiv preprint arXiv:2407.10671*, 2024.
- H. Zhang, C. Wei, J. Lee, and T. Ma. Shape matters: Understanding the implicit bias of the noise covariance. In *Conference on Learning Theory*, pages 2315–2357. PMLR, 2021.
- Y. Zhang, C. Chen, N. Shi, R. Sun, and Z.-Q. Luo. Adam can converge without any modification on update rules. *Neural Information Processing Systems*, 35:28386–28399, 2022.
- L. Zhao, T. Wei, L. Zeng, C. Cheng, L. Yang, P. Cheng, et al. LongSkywork: A training recipe for efficiently extending context length in large language models. *arXiv preprint arXiv:2406.00605*, 2024.
- P. Zhou, X. Xie, Z. Lin, K.-C. Toh, and S. Yan. Win: Weight-decay-integrated Nesterov acceleration for faster network training. *Journal of Machine Learning Research*, 25(83): 1–74, 2024a.
- P. Zhou, X. Xie, Z. Lin, and S. Yan. Towards understanding convergence and generalization of AdamW. *IEEE Transactions on Pattern Analysis and Machine Intelligence*, 2024b.
- Z. Zhu, J. Wu, B. Yu, L. Wu, and J. Ma. The anisotropic noise in stochastic gradient descent: Its behavior of escaping from sharp minima and regularization effects. In *International Conference on Machine Learning*, pages 7654–7663. PMLR, 2019.